Università degli Studi di Firenze
Facoltà di Scienze Matematiche Fisiche e Naturali

Tesi di Dottorato in Fisica
XVII ciclo

Bose-Einstein Condensates in Optical Lattices

Leonardo Fallani

Supervisore:
Prof. Massimo Inguscio

Coordinatore del corso:
Prof. Alessandro Cuccoli

Contents

Introduction

Since the experimental realization of Bose-Einstein condensates of dilute gases in 1995, ten years of exciting theoretical and experimental research have demonstrated that, far from being only an exotic consequence of quantum statistics, Bose-Einstein condensation offers extremely rich possibilities for the investigation of quantum processes lying at the intersection of many different areas of physics [1]. Bose-Einstein condensates of trapped gases constitute a window for the observation of the *quantum world*, since they are macroscopic objects which behave according to the laws of quantum mechanics. The appeal of these systems relies in the fact that their quantum wavefunction can be directly observed and manipulated. This unique possibility makes them attractive for the study of many problems of fundamental physics. One of most striking evidences of this macroscopic quantum behavior is the observation of interference in two spatially overlapping condensates [2]. Indeed, Bose-Einstein condensation is one of the physical phenomena in which the undulatory nature of matter emerges in all its evidence.

Bose-Einstein condensation has provided a revolution in *atom optics* comparable to the one produced in ordinary optics by the invention of the laser. As the laser emission, Bose-Einstein condensation results from the macroscopic occupation of a single bosonic state, thus providing a much more brilliant and coherent source than thermal atoms for experiments of atom optics. In order to run atomic interferometers or any other atom optics experiment, it is necessary to implement tools for the manipulation of matter-waves. Forces resulting from the interaction between atoms and laser light can be used to efficiently manage the properties of coherent matter waves. In this context the role of light and matter is exchanged with respect to what happens in ordinary optics, where material devices are used to direct and manipulate light beams. In particular, the mechanical effects of laser standing waves, the so-called *optical lattices*, have provided a simple tool for the implementation of mirrors and beam splitters [3], as well as diffraction gratings for matter waves [4].

Far from being only tools for atom optics, optical lattices have demonstrated to be invaluable instruments for more fundamental investigations. The study of ultracold atoms in optical lattices has thrown a bridge between the worlds of atomic physics and *solid state physics*. Laser beams in standing wave

configuration provide ideal periodic potentials for the atoms, with no defects and no phonons, thus constituting a testground for the quantum theory of transport in periodic structures. Furthermore, these systems allow a broad tunability of the interaction parameters, since the depth of the periodic potential can be easily changed by tuning the frequency and intensity of the laser light forming the standing wave. Appealing experiments performed in the late '90s demonstrated that ultracold atoms in optical standing waves indeed behave as a gas of electrons in a crystal of ions. Cold atoms in optical lattices have opened the possibility to experimentally study many effects predicted by the band theory and not previously observed for electrons moving in ordinary crystalline solids, such as Bloch oscillations, Wannier-Stark ladders and Landau-Zener tunnelling [5]. Bose-Einstein condensates represent the ultimate tool for the investigation of these phenomena, due to the extremely small momentum spread and their large coherence length. The most fascinating aspect of this research is that it is possible to trace the dynamics of a single quantum object in a ideal periodic potential, a goal that is hardly achievable for electrons moving in crystalline solids, where the main observables are related only to ensemble properties.

Differently from photons, the constituents of the matter-wave field are interacting particles. The presence of interactions enriches the properties of the condensed many-body system with fascinating phenomena such as sound propagation and superfluidity. In particular, the presence of an interaction term in the wave equation describing the system is responsible for the self-nonlinear behavior of matter waves. This property is at the basis of many intriguing phenomena, such as solitonic propagation [6] and four-wave mixing [7]. In the context of optical lattices, the presence of such nonlinearities leads to a number of new effects deviating from the single-particle Bloch theory, including the observation of different kinds of instabilities [8]. Quantum degenerate samples of spin-polarized fermions are free from these effects and indeed they constitute a promising resource in the field of metrology and for the implementation of high-accuracy force sensors [9].

Optical lattices also constitute an important tool for the investigation and the manipulation of the *superfluid properties* of Bose-Einstein condensates. The connection between superfluidity and Bose-Einstein condensation can be traced back to 1938 with the theory of F. London on the behavior of liquid ^{4}He below the lambda point [10]. Since the realization of Bose-Einstein condensation in dilute gases, many experiments have demonstrated that a condensate indeed behaves as a superfluid. The most striking evidences of this superfluid behavior are the detection of quantized vortexes [11, 12], the observation of a reduced moment of inertia (with respect to the classical rigid value) [13, 14], the measurement of the collective modes frequencies [15, 16], as well as the evidence that condensates exhibit a macroscopic phase. In this context many experimental and theoretical works have studied how an optical lattice can

be used to detect and to modify the superfluid properties of Bose-Einstein condensates. It has been shown that for small depths of the periodic potential the system still behaves as a superfluid, as demonstrated by the presence of long-range coherence [17, 18, 19] and by the dynamical response of the system to applied potential gradients [20]. For larger potential depths new regimes can be reached. This is the case of the transition from a superfluid to a Mott insulator, driven by pure quantum fluctuations, in which the repulsive interaction between atoms forces a localization in the lattice sites, with a vanishing long-range coherence and the creation of number Fock states in each well [21]. Still in the frame of these strongly correlated systems, when a disordered potential is added to the periodic structure, new localized phases are expected to emerge, such as the Bose-glass or the Anderson-localized states [22, 23].

From an applicative point of view, much effort is spent in the direction of implementing *quantum computing* schemes with cold atoms in optical lattices [24, 25]. While the experiments made until now with single ions in electrostatic traps [26, 27] seem to be the most promising road for the actual realization of quantum computational schemes, due to the long decoherence times, ultracold atoms in optical lattices could provide an appealing alternative [28]. An attracting perspective is the use of such systems as *quantum simulators*, i.e. quantum many-body systems that, with an appropriate choice of the interaction parameters, may simulate the behavior of other quantum physical systems driven by the same Hamiltonian.

This PhD thesis is the conclusion of three years of work at the European Laboratory for Nonlinear Spectroscopy (LENS) in Florence. During this period we have focused our experimental activity mostly on the investigation of the transport and superfluid properties of a Bose-Einstein condensate in a one-dimensional optical lattice. The presentation of the work is organized according to the following scheme.

In the first chapter we will introduce the main theoretical instruments concerning the description of Bose-Einstein condensates and the physics of periodic potentials. In particular, we will present the main results of the Bloch theory for a gas of noninteracting particles, discussing how the band structure concepts can be extended to the description of a condensate in a periodic potential and which the limits of applicability of this approach are.

In the second chapter we will present the main features of the apparatus working at LENS for the production of Bose-Einstein condensates of ^{87}Rb.

The third chapter is devoted to the description of two experiments [29, 30] focused on the study of the collective dynamics of a harmonically trapped condensate in the presence of a static periodic potential. In the regime of small amplitude oscillations we have found that the frequencies of the dipole and quadrupole modes show a strong dependency on the lattice height, that can be explained in terms of a modified *effective mass*. Out of this regime, when the

amplitude of the oscillations becomes larger, we observe the disruption of the superfluid dynamics and the onset of a classical *insulating* regime characterized by a loss of long-range coherence.

In the fourth chapter we will present the results of some experiments performed with a Bose-Einstein condensate in a moving optical lattice [31, 32, 33]. The possibility to move the periodic potential with controlled velocity allows us to selectively access states with well defined quasimomentum and band index, thus exploring the full band structure. In a first set of experiments (performed in a low density regime) we have studied the expansion of the condensate in the moving lattice: this technique has allowed us to perform a precise band spectroscopy and to evidence a *lensing effect* caused by a modification of the matter-wave dispersion induced by the lattice. In a second set of experiments (performed in a high density regime) we have studied the time evolution of the harmonically trapped condensate in the presence of the moving lattice: we have carried out a detailed investigation of the stability regimes of the nonlinear Bloch states, separately identifying the effects of *energetic* and *dynamical instability*, the two main mechanisms causing the breakdown of the Bloch waves in a nonlinear periodic system.

In the last chapter we will present preliminary observations on both static and dynamic properties of Bose-Einstein condensates in optical lattices with large spacing and in disordered potentials produced by optical speckle patterns [34]. We will mainly address the problems of localization, with a particular attention to the issue of quantum interference after expansion (recently studied also in [35]) and to the observed modifications of the collective dynamics.

Chapter 1

A bit of theory

In this first chapter we will introduce, from a theoretical point of view, the two main ingredients that have been used in the experiments described in this thesis: Bose-Einstein condensates and periodic potentials.

In the first section we will review the basic notions regarding Bose-Einstein condensation, introducing some notations and equations that will be extensively used in the text. We will first consider the general problem of Bose-Einstein condensation, specializing the theoretical analysis to the case of a harmonically trapped gas. We will consider the effect of interactions among the particles by introducing the Gross-Pitaevskii mean-field theory, that has proven to be a powerful tool for the description of both static and dynamic properties of condensates of weakly interacting neutral atoms.

In the second section we will consider the problem of a quantum particle in a periodic potential. Following an approach well known in solid state physics, we will review the main features of the Bloch theory for a gas of noninteracting particles. We will discuss how the band structure concepts can be used to describe the physics of a Bose-Einstein condensate in a periodic potential and what the limits of applicability of this theory are. In particular, we will show how the nonlinearity connected to the wave equation of the system can affect the Bloch picture, by enriching the physics of these systems with many spectacular effects.

1.1 Bose-Einstein condensation

Bose-Einstein condensation is a pure quantum phenomenon consisting of the macroscopic occupation of a single-particle state by an ensemble of identical bosons in thermal equilibrium at finite temperature. The occurrence of this phase transition in a gas of atoms was first predicted by A. Einstein in 1925 [36], following the ideas contained in a paper by S. N. Bose devoted to the statistical description of the quanta of light [37].

Let us consider a gas of identical bosons confined in a box in thermal equilibrium at temperature T. From a quantum-mechanical point of view, owing to the position uncertainty associated with the thermal momentum distribution, the particles can be described as wavepackets with an average extent corresponding to the thermal *de Broglie wavelength*

$$\lambda_{dB} = \frac{h}{\sqrt{2\pi m k_B T}}, \tag{1.1}$$

where h is the Planck constant, m is the mass of the particles and k_B is the Boltzmann constant. Decreasing the temperature of the system, the particles slow down and the spatial extent of the wavepackets increases. When the thermal de Broglie wavelength becomes comparable with the mean interparticle distance, the overlap between the wavepackets cannot be neglected and the quantum indistinguishability of the particles becomes important. In this condition the system behaves quite differently depending on the quantum nature of the particles, whether they are bosons or fermions. In the case of bosons, as the gas is cooled down, a critical temperature T_C exists below which the particles start to macroscopically occupy the lowest energy state and a Bose-Einstein condensate (BEC) forms. This phenomenon, driven only by quantum statistics, does not depend on the interactions among particles, which may instead counteract this pure quantum effect.

Following the Maxwell-Boltzmann statistics, at $T = 0$ the system naturally occupies the lowest energy state, since the thermal entropic contribution to the free energy vanishes. The intriguing feature of Bose-Einstein condensation is, indeed, that it results in the macroscopic occupation of a single-particle state at $T > 0$, when the thermal energy $k_B T$ of the system is much bigger than the level spacing and the classical Maxwell distribution would predict occupancy of a quasi-continuum of levels.

An important parameter measuring how quantum-mechanically a gas behaves is the *phase-space density* $n\lambda_{dB}^3$, where n is the numerical density of the sample. For an ideal gas the BEC phase transition happens when

$$n\lambda_{dB}^3 = 2.612. \tag{1.2}$$

For a gas of ^{87}Rb atoms at normal conditions ($P = 10^5$ Pa, $T = 300$ K) $\lambda_{dB} \simeq 0.01$ nm and $n\lambda_{dB}^3 \approx 10^{-8}$: this means that the gas behaves according to the classical laws of mechanics. The eight orders of magnitude in the phase-space density separating a room temperature gas from a quantum degenerate sample can be filled either by increasing the density or, more easily, by decreasing the temperature. However, an important problem arises regarding the thermodynamic stability of the system. Indeed, at sufficiently low temperatures, all the known interacting systems, with the exception of helium, undergo a phase transition to the solid phase. In Fig. 1.1 (adapted from [38]) we show a typical pressure-temperature diagram, indicating the boundaries

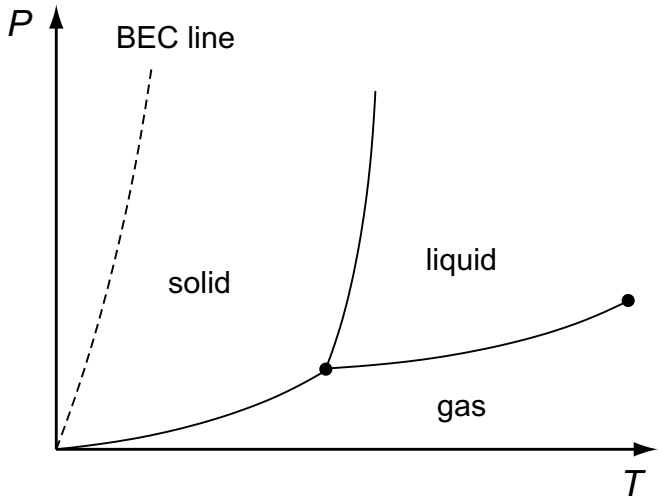

Figure 1.1: A typical pressure-temperature phase diagram. The dashed line corresponds to the BEC transition for an ideal gas (adapted from [38]).

between the solid, liquid and gaseous phases. The dashed line corresponds to the BEC phase transition for an ideal gas. From this diagram it is clear that, in order to observe Bose-Einstein condensation, one has to get rid of all the processes that could bring the system into the thermodynamically stable solid phase. This can be achieved by working with very dilute samples, in which the probability of inelastic three-body collisions can be neglected and the system may reach a metastable Bose-condensed phase. The drawback of this strategy is that one has to work with samples that are many thousand times more dilute than air and has to bring them down to temperatures of the order of μK or even less.

Bose-Einstein condensation in dilute gases of neutral atoms has been experimentally achieved for the first time in 1995 by the group leaded by E. Cornell and C. Wieman at JILA (Boulder, CO, USA) and, after few months, by the group of W. Ketterle at MIT (Cambridge, MA, USA). This achievement, recognized with the Nobel Prize in Physics in 2001 [39, 40], is the spectacular result of the progresses made in atomic physics in the last decades with the development of advanced techniques for cooling and trapping neutral atoms (as awarded by the Nobel Prize in Physics in 1997). In the last ten years Bose-Einstein condensation has been achieved in many other laboratories all over the world. Up to now, the complete list of elements brought to BEC is formed by ^{87}Rb, ^{23}Na, ^{7}Li, H, ^{85}Rb, ^{4}He*, ^{41}K, ^{133}Cs, ^{174}Yb and ^{52}Cr (in chronological order).

1.1.1 BEC of a trapped noninteracting gas

Let us now consider a gas of N noninteracting identical bosons in a three-dimensional harmonic confining potential [41]

$$V_{ext}(\mathbf{r}) = \frac{1}{2}m\left(\omega_x^2 x^2 + \omega_y^2 y^2 + \omega_z^2 z^2\right), \tag{1.3}$$

that is the actual trapping potential in which Bose-Einstein condensates are produced in the experiments. The eigenvalues of the single-particle Hamiltonian problem for the 3D harmonic oscillator are

$$\epsilon_{n_x,n_y,n_z} = \left(n_x + \frac{1}{2}\right)\hbar\omega_x + \left(n_y + \frac{1}{2}\right)\hbar\omega_y + \left(n_z + \frac{1}{2}\right)\hbar\omega_z\,, \tag{1.4}$$

where n_x, n_y and n_z are the quantum numbers identifying the oscillator state. For a system in thermal equilibrium, the occupancy of the levels is described by the Bose-Einstein statistics, according to which the mean occupation number is given in the grand-canonical ensemble by [42]

$$f(n_x, n_y, n_z) = \frac{1}{e^{\beta(\epsilon_{n_x,n_y,n_z} - \mu)} - 1}\,, \tag{1.5}$$

where $\beta = (k_B T)^{-1}$ is the inverse reduced temperature, k_B is the Boltzmann constant and μ is the *chemical potential*, that accounts for the conservation of the total number of particles

$$N = \sum_{n_x,n_y,n_z} \frac{1}{e^{\beta(\epsilon_{n_x,n_y,n_z} - \mu)} - 1}\,. \tag{1.6}$$

In the classical limit of high temperature the chemical potential is large and negative and the Bose statistics (1.5) reduces to the Maxwell-Boltzmann statistics. Let us suppose that, lowering the temperature of the system, the chemical potential approaches the ground state energy $\epsilon_{0,0,0}$ at finite T. In this case, Eq. (1.5) predicts that the population of the ground state should become macroscopic. Substituting $\mu = \epsilon_{0,0,0}$ in Eq. (1.6) we obtain

$$N = N_0 + \sum_{n_x,n_y,n_z} \frac{1}{e^{\beta\hbar(\omega_x n_x + \omega_y n_y + \omega_z n_z)} - 1}, \tag{1.7}$$

where we have isolated the population of the ground state N_0, that produces a divergence in the sum. If the level spacing $\hbar\omega_i$ is much smaller than $k_B T$, we can substitute the sum with the integral (semiclassic approximation)

$$N = N_0 + \int_0^\infty \frac{dn_x dn_y dn_z}{e^{\beta\hbar(\omega_x n_x + \omega_y n_y + \omega_z n_z)} - 1}. \tag{1.8}$$

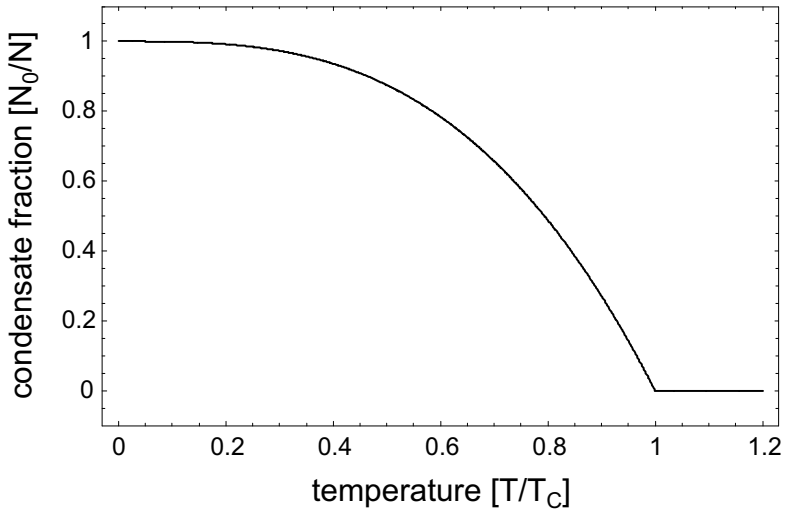

Figure 1.2: Condensate fraction as a function of temperature for a gas of noninteracting particles confined in a 3D harmonic potential.

By carrying out the integration, we find that the number of atoms in the condensed fraction as a function of T is

$$N_0 = N\left[1 - \left(\frac{T}{T_C}\right)^3\right], \tag{1.9}$$

where the *critical temperature* T_C has been defined as

$$T_C = \frac{\hbar\bar{\omega}}{k_B}\left(\frac{N}{\zeta(3)}\right)^{1/3} = 0.94\frac{\hbar\omega_{ho}}{k_B}N^{1/3}, \tag{1.10}$$

in which $\zeta(n)$ is the Riemann function and $\omega_{ho} = (\omega_x\omega_y\omega_z)^{1/3}$ is the geometric average of the trapping frequencies. This derivation is strictly valid in the thermodynamic limit, that for a harmonically trapped gas corresponds to the limit $N \to \infty$, with $N\omega_{ho}^3$ constant. In Fig. 1.2 we plot the condensate fraction as a function of temperature as obtained from Eq. (1.9).

At $T = 0$ all the atoms will occupy the harmonic oscillator ground state. The constructive interference of the single-particle wavefunctions adds up to build the condensate density distribution

$$n(\mathbf{r}) = N\left(\frac{m\bar{\omega}}{\pi\hbar}\right)^{3/2}\exp\left[-\frac{m}{\hbar}\left(\omega_x x^2 + \omega_y y^2 + \omega_z z^2\right)\right], \tag{1.11}$$

that corresponds to the square modulus of the gaussian wavefunction of the harmonic oscillator ground state normalized with $\int d\mathbf{r}\, n(\mathbf{r}) = N$.

We note that, for a harmonically trapped gas, Bose-Einstein condensation occurs with a sudden narrowing of the density distribution both in momentum and coordinate space. This is different from the case of a bosonic gas confined in a box, in which the condensation occurs only in momentum space, while in coordinate space the condensed gas remains delocalized and cannot be spatially distinguished from the non-condensed component.

The BEC transition can be classified according to the Ginzburg-Landau criterion for the classification of phase transitions [43]. The degree of symmetry of the system is described by an *order parameter*, that is zero for $T > T_C$ and nonzero for $T < T_C$, reflecting a spontaneous symmetry breaking in the low temperature phase. In the case of the BEC transition the order parameter is the condensate density. Since it varies continuously around T_C with a discontinuity in the first derivative, the BEC transition can be classified as a second-order phase transition according to the Ginzburg-Landau criterion.

1.1.2 BEC of a trapped interacting gas

In the previous section we have considered the problem of Bose-Einstein condensation for a noninteracting ideal gas. The thermodynamic behavior of such a system around the critical temperature is completely governed by quantum statistics. However, real systems are always characterized by interactions among their constituent particles. In strongly interacting systems the presence of interactions can blur the quantum effects and lead to a significant quantum depletion of the condensate phase even at zero temperature. This is the case of superfluid ^{4}He, in which only a small fraction of the liquid (typically around 10%) is Bose-condensed. In the case of weakly interacting systems, as for BEC of dilute gases, quantum depletion can be neglected. However, the presence of interactions strongly modifies the properties of the system, leading to a nonlinear behavior of the de Broglie matter-wave that enriches the multitude of observable phenomena.

In second quantization, the many-body Hamiltonian operator describing a system of N bosons in an external potential V_{ext} is given by

$$\hat{H} = \int d\mathbf{r}\ \hat{\Psi}^\dagger(\mathbf{r}) \left[-\frac{\hbar^2 \nabla^2}{2m} + V_{ext}(\mathbf{r}) \right] \hat{\Psi}(\mathbf{r}) + \frac{1}{2} \iint d\mathbf{r} d\mathbf{r}'\ \hat{\Psi}^\dagger(\mathbf{r}) \hat{\Psi}^\dagger(\mathbf{r}') V_{int}(|\mathbf{r} - \mathbf{r}'|) \hat{\Psi}(\mathbf{r}') \hat{\Psi}(\mathbf{r}) \ , \quad (1.12)$$

where $\hat{\Psi}(\mathbf{r})$ ($\hat{\Psi}^\dagger(\mathbf{r})$) is the boson field annihilation (creation) operator and V_{int} describes binary s-wave collisions, that in an ultracold dilute gas are the only relevant collisional processes. The field operator can be written as

$$\hat{\Psi}(\mathbf{r}) = \sum_j \Psi_j(\mathbf{r}) \hat{b}_j \ , \quad (1.13)$$

where $\Psi_j(\mathbf{r})$ is the wavefunction of the single-particle state j and $\hat{b}_j$ is the annihilation operator of a boson in the state j. From a very general point of view, the field operator $\hat{\Psi}(\mathbf{r})$ can be written in Heisenberg representation as

$$\hat{\Psi}(\mathbf{r},t) = \Psi(\mathbf{r},t) + \delta\hat{\Psi}(\mathbf{r},t) \; , \tag{1.14}$$

where $\Psi(\mathbf{r},t) = \langle\hat{\Psi}(\mathbf{r},t)\rangle$ is the expectation value of the field operator and $\delta\hat{\Psi}(\mathbf{r},t)$ describes the quantum + thermal excitations. Bose-Einstein condensation occurs when the single-particle ground state exhibits macroscopic occupancy. Using a standard approach in quantum field theory, when the number of particles in one state is macroscopic ($N_0 \gg 1$), the creation and annihilation operators can be substituted with *c-numbers*, thus recovering the limit of a classical field. With this assumption the expectation value $\Psi(\mathbf{r},t)$ naturally results from the macroscopic occupancy of the ground state, while $\delta\hat{\Psi}(\mathbf{r},t)$ describes the excitations. Following the Bogoliubov approximation we neglect the contribution of $\delta\hat{\Psi}(\mathbf{r},t)$, thus the Heisenberg equation of motion for $\hat{\Psi}(\mathbf{r},t)$ becomes an equation for the classical field $\Psi(\mathbf{r},t)$:

$$i\hbar\frac{\partial}{\partial t}\Psi(\mathbf{r},t) = \left[-\frac{\hbar^2\nabla^2}{2m} + V_{ext}(\mathbf{r}) + \int d\mathbf{r}' \; \Psi^\dagger(\mathbf{r}',t)V_{int}(\mathbf{r}-\mathbf{r}')\Psi(\mathbf{r}',t)\right]\Psi(\mathbf{r},t) \; , \tag{1.15}$$

where the complex function $\Psi(\mathbf{r},t)$ is the *condensate wavefunction* and represents the order parameter of the phase transition. If the mean interparticle distance $n^{-1/3}$ is much larger than the range of the two-body potential V_{int} (diluteness condition), the latter can be substituted with the effective pseudopotential $g\delta(\mathbf{r}-\mathbf{r}')$. With this assumption, that in dilute gases is generally well satisfied, the previous equation becomes

$$i\hbar\frac{\partial}{\partial t}\Psi(\mathbf{r},t) = \left[-\frac{\hbar^2\nabla^2}{2m} + V_{ext}(\mathbf{r}) + g|\Psi(\mathbf{r},t)|^2\right]\Psi(\mathbf{r},t) \; . \tag{1.16}$$

This equation is known as *Gross-Pitaevskii equation* (GPE), after the two scientists that independently derived it in the early '60s. The interaction constant g is related to the *scattering length* a by the relation

$$g = \frac{4\pi\hbar^2 a}{m}. \tag{1.17}$$

In the following we will consider only positive values of the scattering length, corresponding to repulsive interactions between particles[1]. As one can see

[1] Actually, for negative scattering lengths, condensates are stable only for very small number of atoms N. Above a critical value N_C the attractive interactions between atoms cause a collapse of the condensate due to inelastic collisional processes.

from Eq. (1.16), the presence of interactions gives rise to a nonlinear term in the wave equation for the condensate order parameter. This term, describing the condensate self-interaction, is particularly important as it is responsible for a rich multitude of nonlinear phenomena. In the context of coherent matter-wave optics it plays the same role as the third-order susceptibility $\chi^{(3)}$ in nonlinear optics, producing effects such as self-defocusing, four wave mixing and solitonic propagation.

The stationary solutions of Eq. (1.16) can be calculated using the ansatz $\Psi(\mathbf{r},t) = e^{-i\mu t/\hbar}\psi(\mathbf{r})$, where μ is the condensate chemical potential. Substituting this expression in Eq. (1.16) we obtain the time-independent GPE

$$\left[-\frac{\hbar^2\nabla^2}{2m} + V_{ext}(\mathbf{r}) + g|\psi(\mathbf{r})|^2\right]\psi(\mathbf{r}) = \mu\psi(\mathbf{r})\ . \tag{1.18}$$

The ground state of the system can be analytically calculated by solving this equation in the so-called *Thomas-Fermi approximation*, holding for $Na/a_{ho} \gg 1$, where $a_{ho} = \sqrt{\hbar/m\omega_{ho}}$ is the average harmonic oscillator length. In this regime of large number of atoms the interaction term $g|\psi(\mathbf{r},t)|^2$ dominates the kinetic term $-\hbar^2\nabla^2/2m$, that can be neglected. With this assumption, well satisfied in most of the experiments, the differential equation (1.18) becomes an algebraic equation from which we obtain the condensate density

$$n(\mathbf{r}) = |\psi(\mathbf{r})|^2 = \frac{1}{g}\left[\mu - V_{ext}(\mathbf{r})\right]\ \theta\left[\mu - V_{ext}(\mathbf{r})\right], \tag{1.19}$$

where $\theta(x)$ is the Heaviside function (equal to 1 for $x > 0$, to 0 for $x \leqslant 0$). In the case of an axially symmetric harmonic trap with $\omega_x = \omega_y = \omega_\perp$, the explicit shape of the condensate density distribution is an inverted parabola

$$n(\mathbf{r}) = n_0\left(1 - \frac{x^2+y^2}{R_\perp^2} - \frac{z^2}{R_z^2}\right)\theta\left(1 - \frac{x^2+y^2}{R_\perp^2} - \frac{z^2}{R_z^2}\right), \tag{1.20}$$

whose height and widths are connected to the chemical potential by

$$n_0 = \frac{\mu}{g} = \frac{\hbar\omega_{ho}}{2g}\left(\frac{15Na}{a_{ho}}\right)^{2/5} \tag{1.21}$$

$$R_z = \sqrt{\frac{2\mu}{m\omega_z^2}} \tag{1.22}$$

$$R_\perp = \sqrt{\frac{2\mu}{m\omega_\perp^2}} \tag{1.23}$$

The repulsive interaction term in Eq. (1.18) has the effect of broadening the density distribution of the single-particle ground state. In Fig. 1.3 we show the condensate density distribution for $N = 3\times10^5$, $\omega_z = 2\pi\times 9$ Hz and

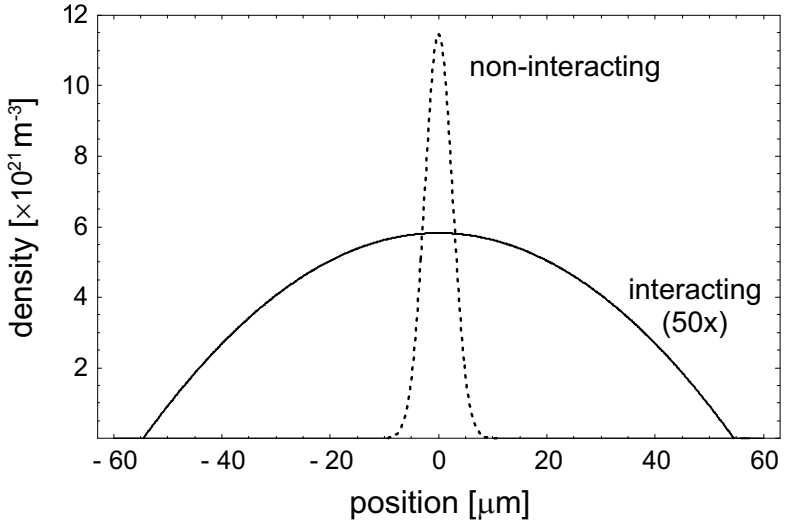

Figure 1.3: BEC density distribution for $N = 3 \times 10^5$, $\omega_z = 2\pi \times 9$ Hz and $\omega_\perp = 2\pi \times 90$ Hz in the noninteracting case (dotted line) and for a repulsive interaction characterized by the scattering length $a = 5.7$ nm (solid line, value for ^{87}Rb). The density is evaluated along the trap axis (note the 50x magnification factor of the vertical scale in the interacting case).

$\omega_\perp = 2\pi \times 90$ Hz in the noninteracting case (dotted line) and for a repulsive interaction with strength $a = 5.7$ nm (solid line)[2]. The ratio between the peak density of the Thomas-Fermi distribution (1.21) and the peak density of the noninteracting distribution (1.11) is

$$\frac{n_0}{n_0^{ho}} = \frac{15^{2/5}\pi^{1/2}}{8}\left(\frac{Na}{a_{ho}}\right)^{-3/5}, \tag{1.24}$$

corresponding to 1% for the parameters of Fig. 1.3, where $Na/a_{ho} \simeq 10^3$.

The change in shape from a gaussian thermal distribution to a Thomas-Fermi distribution is well confirmed by the experiments and indeed used as a signature of Bose-Einstein condensation (as discussed in Sec. 2.3.2). A comparison of the distribution (1.20) with the numerical solution of Eq. (1.18) shows that the Thomas-Fermi approximation yields an excellent result, but fails at the edges of the distribution, when density goes to zero. Indeed in these regions the kinetic term dominates on the (vanishing) interaction energy term and the actual density distribution goes to zero in a smoother way (with no discontinuity in the first derivative) [41].

[2]These numbers correspond to the typical parameters of our experimental setup.

1.2 Periodic potentials

1.2.1 Noninteracting particles in periodic potentials

Let us consider a gas of noninteracting particles in a periodic potential, a well known problem of quantum mechanics [44]. For simplicity we can restrict to the one-dimensional case, because this is the configuration we have used in the experiments described in the following chapters. The periodicity condition for the potential $V(x)$ takes the form

$$V(x) = V(x + d) \tag{1.25}$$

where d is the lattice spacing. Let us consider the time-independent Schrödinger equation for the wavefunction $\Psi(x)$ of a particle of mass m moving in this potential:

$$\hat{H}\Psi(x) = \left[-\frac{\hbar^2}{2m}\frac{\partial^2}{\partial x^2} + V(x)\right]\Psi(x) = E\Psi(x) \tag{1.26}$$

The Bloch theorem states that solutions of Eq. (1.26) take the form

$$\Psi_{n,q}(x) = e^{iqx}u_{n,q}(x) \tag{1.27}$$

$$u_{n,q}(x) = u_{n,q}(x + d), \tag{1.28}$$

which describes plane waves e^{iqx} modulated by functions $u_{n,q}(x)$ having the same periodicity of the lattice. These stationary solutions are labelled by two quantum numbers: the *band index* n and the *quasimomentum* q.

The quantum number q is called *quasimomentum* because it presents some analogies with the momentum p, which is the good quantum number to describe the eigenstates of the Schrödinger equation in the absence of any external potential. These analogies will be more evident in the following section, when we will study the dynamics of a Bloch wavepacket in the presence of external forces. However, since the potential $V(x)$ does not present a complete translational invariance, the solutions (1.27) are not eigenstates of the momentum operator and $\hbar q$ is *not* the expectation value of the momentum. We note that, because of the discrete invariance of the Hamiltonian under translations $x \to x + nd$ (with n integer), the quasimomentum is defined modulus $2\pi/d$, that is the period of the reciprocal lattice. As a matter of fact, the periodicity of the problem in real space induces a periodic structure also in momentum space, in which the elementary cells are the so called *Brillouin zones*.

For a given quasimomentum q many different solutions with different energies $E_n(q)$ exist. These solutions are identified with the band index n. The term *band* refers to the fact that the periodic potential causes a segmentation of the energy spectrum into allowed and forbidden zones, the so called *energy bands*, which in solid state physics are at the basis of the conduction properties of metals and insulators. For generic periodic potentials $V(x)$, the energy

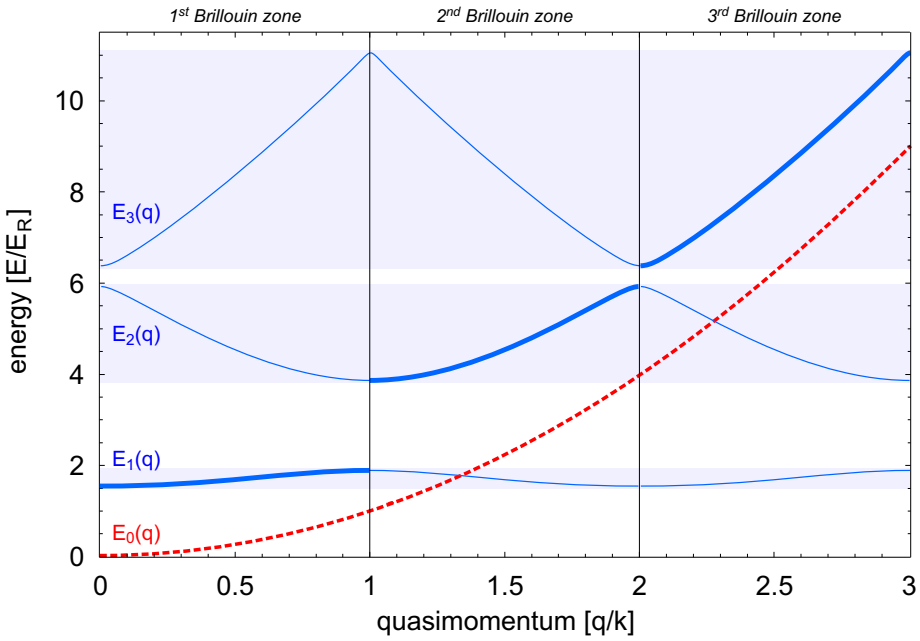

Figure 1.4: Solid curves: lowest three energy bands for a particle of mass m in the periodic potential (1.29) with $V_0 = 4E_R$. Dashed curve: energy spectrum of the free particle. The energies are expressed in natural units $E_R = \hbar^2 k^2/2m$.

spectrum $E_n(q)$ may be easily calculated in the two limits of weak and strong potentials, for which one can use a perturbative approach starting from the free and the tightly bound particle cases, respectively.

The simplest form of periodic potential is the pure sinusoidal potential

$$V(x) = \frac{V_0}{2}\left(1 - \cos 2kx\right), \tag{1.29}$$

which has a spatial periodicity $d = \pi/k$. For this particular choice the Schrödinger equation (1.26) becomes

$$\left[-\frac{\hbar^2}{2m}\frac{\partial^2}{\partial x^2} + \frac{V_0}{2}\left(1 - \cos 2kx\right)\right]\Psi_{n,q}(x) = E_n(q)\Psi_{n,q}(x). \tag{1.30}$$

This equation has the form of the well known *Mathieu equations* [45], whose solutions do not have an analytic expression, but are tabulated and their approximations can be easily evaluated numerically.

In Fig. 1.4 we plot the eigenenergies of Eq. (1.30) as a function of the quasimomentum q for the first three energy bands in the first three Brillouin zones. In this example the height of the periodic potential is $V_0 = 4E_R$, where $E_R = \hbar^2 k^2/2m$ is a natural energy scale introduced by the lattice (its meaning will be clear in Sec. 3.1.3 when discussing about the physical realization

of such a potential). The solid thick lines correspond to a representation of the energy spectrum in the so called *extended zone scheme*, in which different energy bands are plotted in different Brillouin zones. However, because the quasimomentum is defined modulus a vector of the reciprocal lattice, the spectrum $E_n(q)$ can be more generally represented in the *repeated zone scheme*, in which all the energy bands are plotted in all the Brillouin zones (both thin and thick solid lines). For comparison, we plot in the same graph also the parabolic energy spectrum of the free particle (dashed curve). Even though this is only an example, some general features of the band structure are already clear from this particular case:

1. At low energies ($E_n \ll V_0$) the bands are almost flat and, for increasing height of the periodic potential, asymptotically tend to the eigenenergies of the harmonic oscillator obtained with a parabolic approximation of the single lattice site potential.

2. At high energies ($E_n \gg V_0$) the bands are pretty similar to the free particle spectrum (except for a zero-point energy shift) and differ from the latter only near the boundaries of the Brillouin zones.

3. Near the zone boundaries, in correspondence with the appearance of the energy gap, the bands have null derivative.

Let us now consider the shape of the solutions of Eq. (1.30). In Fig. 1.5 we plot the squared modulus of the lowest band wavefunction $\Psi_{0,0}(x)$ for $q = 0$ and three different heights of the periodic potential: $V_0 = E_R$ (dotted line), $V_0 = 5E_R$ (dashed line), $V_0 = 25E_R$ (solid line). For small potential heights (dotted line) the Bloch states $\Psi_{0,q}(x)$ are similar to the plane waves e^{iqx}, except for a small amplitude modulation with the periodicity of the lattice. Increasing the lattice height (solid line), when the energy of the system becomes much smaller than the height of the periodic potential, the Bloch wavefunctions turn out to be strongly modulated. In this tight binding limit $E \ll V_0$ these functions can be more conveniently written as the sum of many wavefunctions located at the lattice sites:

$$\Psi_{n,q}(x) = \sum_{j=-\infty}^{\infty} e^{ijqd} \psi_n(x - jd). \tag{1.31}$$

The functions $\psi_n(x)$ are the so-called *Wannier functions* and e^{ijqd} is a phase factor dependent on the quasimomentum q. Eq. (1.31) states that the eigenstates of the system are coherent superpositions of Wannier functions located at the lattice sites and with a well defined phase link across the entire lattice. Generally speaking, Eq. (1.31) can be written for any lattice height, even out of the tight binding regime. For low lattice heights the Wannier functions spread over the entire lattice. In the tight binding regime the Wannier

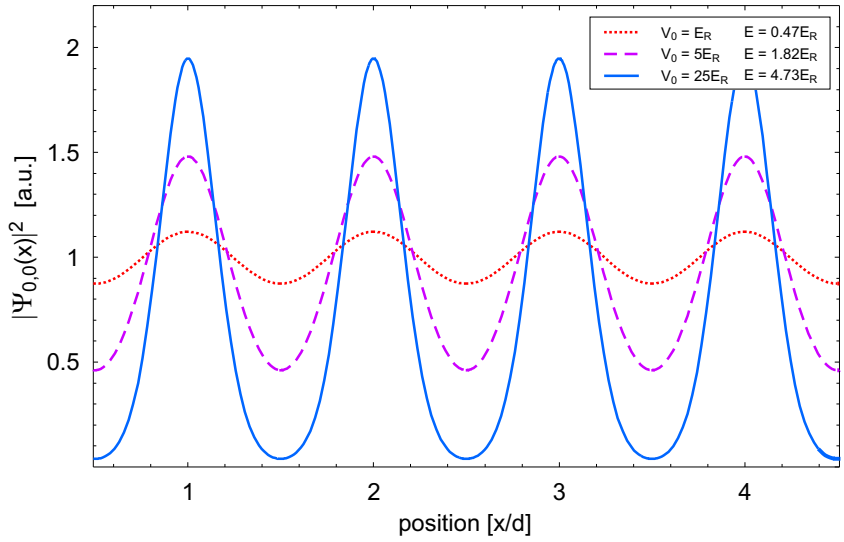

Figure 1.5: Squared modulus of the lowest band wavefunction $\Psi_{0,0}(x)$ as a function of x for $q = 0$ and three different heights of the periodic potential (1.29): $V_0 = E_R$ (dotted), $V_0 = 5E_R$ (dashed), $V_0 = 25E_R$ (solid). Increasing the lattice height, the wavefunction changes from a weakly modulated plane wave to a function that is strongly localized at the lattice sites. In the inset we also report the energy of these states.

functions become strongly localized and, for increasing lattice height, asymptotically tend to the wavefunctions describing the eigenstates of the single lattice sites.

Finally, let us write the Bloch functions $\Psi_{n,q}(x)$ in a further different form, that will be used extensively in the following chapters. From Eq. (1.28) it follows that the periodic function $u_{n,q}(x)$ admits the Fourier expansion

$$u_{n,q}(x) = \sum_{j=-\infty}^{\infty} a_j e^{i2jkx}, \tag{1.32}$$

that, substituted in Eq. (1.27), gives

$$\Psi_{n,q}(x) = \sum_{j=-\infty}^{\infty} a_j e^{i(q+2jk)x}, \tag{1.33}$$

representing a linear combination of plane waves with wavenumber $q + 2jk$. Again, we note that from Eq. (1.33) it follows that the quasimomentum q is only defined modulus $2k$.

1.2.2 Dynamics of a Bloch wavepacket

In this section we review the basic concepts describing the dynamics of a Bloch wavepacket in the presence of external fields. Let us consider a superposition of Bloch states with a mean quasimomentum q and a quasimomentum spread Δq much smaller than the width of the Brillouin zones. From the "uncertainty relation" for the Fourier transform, it follows that the spatial extent of this wavepacket $\Delta x \sim 1/\Delta q$ is much larger than the lattice spacing, i.e. the wavefunction extends on many lattice sites. It is possible to demonstrate that the group velocity of the wavepacket is

$$v_n(q) = \frac{1}{\hbar}\frac{\partial E_n(q)}{\partial q}, \tag{1.34}$$

directly proportional to the first derivative of the band [44]. In the following we will refer to this quantity as *Bloch velocity*. We observe that, since the energy band is flat at the zone boundaries, in these regions the Bloch velocity vanishes. We also note that the expression (1.34) is the matter wave analogy of the group velocity $\partial\omega/\partial k$ for a packet of electromagnetic waves having a dispersion relation $\omega(k)$.

The simplest model describing the dynamics of a Bloch wavepacket in the presence of external fields is the *semiclassical model*. Following this model we make the assumption that the external forces do not modify the energy spectrum of the system, and have only the effect of changing the mean position and the quasimomentum of the wavepacket. The main approximation used in this model is the assumption that the forces F_{ext} acting on the system are slowly varying on the scale of the periodic potential and weak enough not to induce interband transitions (i.e. the band index n can be considered as a constant of the motion). Within these assumptions one can write

$$\dot{x} = \hbar^{-1}\frac{\partial E_n(q)}{\partial q} \tag{1.35}$$

$$\hbar\dot{q} = F_{ext}. \tag{1.36}$$

Eq. (1.35) is a restatement of Eq. (1.34) in which x is now the expectation value of the coordinate operator, i.e. the average position of the wavepacket. As we can see from Eq. (1.36), the effect of the external fields is to change the quasimomentum state q. We observe that Eq. (1.36) is the analogy of second Newton's law of dynamics, but with two important differences: 1) on the left hand side the quasimomentum q is present, instead of the momentum p; 2) on the right hand side only the external forces F_{ext} are present, and not the total forces acting on the system (actually, the forces due to the lattice potential are implicitly included in the energy spectrum E_n). Nevertheless, the similarity between these two equations is remarkable.

To get more insight into the semiclassical model we can use simple maths on Eqs. (1.35) and (1.36) obtaining

$$\ddot{x} = \frac{d}{dt}\left[\hbar^{-1}\frac{\partial E_n(q)}{\partial q}\right] = \hbar^{-1}\frac{\partial^2 E_n(q)}{\partial q^2}\dot{q} = \hbar^{-2}\frac{\partial^2 E_n(q)}{\partial q^2}F_{ext} \tag{1.37}$$

that is a restatement of the second Newton's law of dynamics for a particle subject to an external force F_{ext} and having an *effective mass*

$$m_n^*(q) = \hbar^2\left[\frac{\partial^2 E_n(q)}{\partial q^2}\right]^{-1}, \tag{1.38}$$

which is related to the local curvature of the energy bands (and reduces to the real mass m in the case of the parabolic free particle spectrum).

In Fig. 1.6 we plot the Bloch velocity (1.34) and the effective mass (1.38) as a function of the quasimomentum q for the first three energy bands in a periodic potential with height $V_0 = 4E_R$, the same value used for the calculation of the energy bands in Fig. 1.4. For simplicity, we have used the extended zone scheme, in which only one band for Brillouin zone is plotted. We observe that in proximity of the zone boundaries the effective mass may become negative: this means that a force F_{ext} acting on the wavepacket produces a center-of-mass acceleration in the opposite direction. For comparison, we plot in the same graphs also the (linear) velocity and the (constant) mass of the free particle (dashed curves).

When the approximation of weak forces is relaxed and the acceleration becomes big, interband transitions (the so called *Landau-Zener tunnelling*) may take place. The probability for this process to happen is [46]

$$\Gamma \propto e^{-a_c/a}, \tag{1.39}$$

where $a_c = d(\Delta E)^2/4\hbar^2$ is a critical acceleration dependent on the lattice spacing d and the energy gap ΔE between the lower and the higher band.

1.2.3 A Bose-Einstein condensate in a periodic potential

Bose-Einstein condensates are in principle the ideal tools for the investigation of the quantum effects connected with the dynamics of a particle in a periodic potential. Unlike the electron gas in a crystalline solid, composed by particles in many different states, a condensate is formed by atoms all occupying the same quantum state and acting as the same particle. This opens the possibility to study fundamental issues of quantum mechanics and solid state physics that are not observable in other systems, where it is hardly possible to isolate a single quantum particle and trace its dynamics in the lattice potential.

In the presence of a periodic potential, the BEC will be naturally described by a Bloch wavepacket. The finite size Δx of the condensate causes

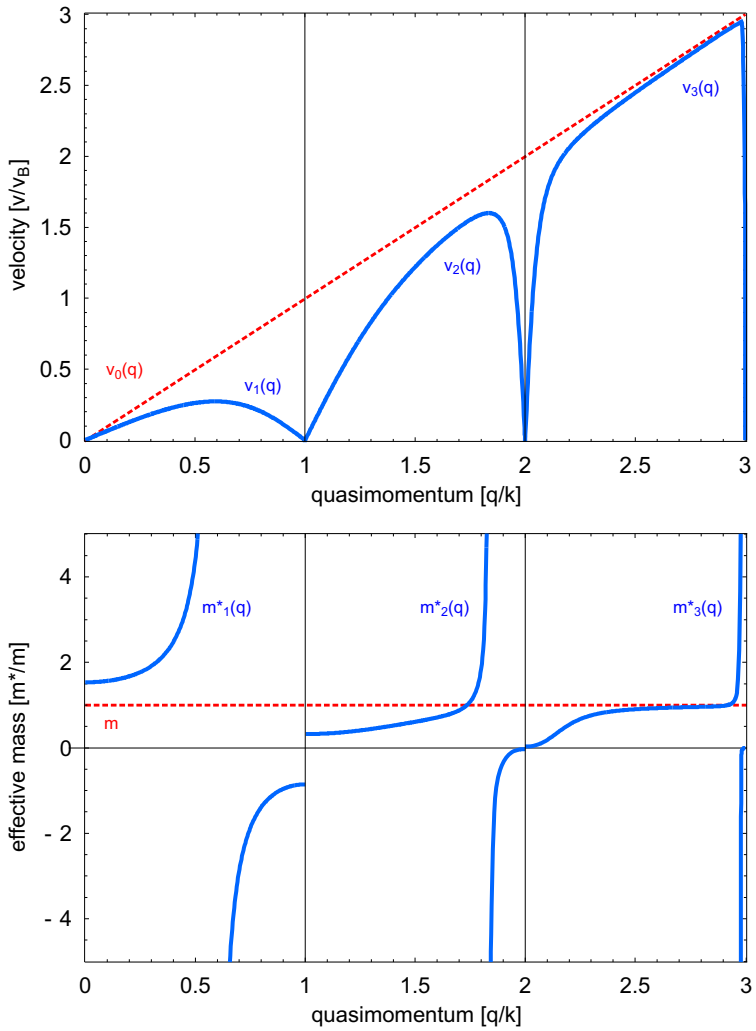

Figure 1.6: Solid curves: Bloch velocity (top) and effective mass (bottom) in the first three energy bands for a particle of mass m in the periodic potential of Eq. (1.29) with $V_0 = 4E_R$. Dashed curves: velocity and mass of the free particle. The velocities are expressed in natural units $v_B = \hbar k/m$ and the effective masses in units of real mass m.

this wavepacket to have a finite quasimomentum spread $\Delta q \sim 1/\Delta x$. As we will discuss in the following chapters, a typical condensate in a near-infrared standing wave optical lattice spreads over $\sim 10^2$ lattice sites. As a consequence, its quasimomentum spread Δq is much smaller than the width of the Brillouin zones and in most cases the condensate can be described with a δ-like distribution in quasimomentum space. Owing to this extremely narrow momentum spread, BECs constitute the ultimate atom sources for the

study of band structure phenomena. Experimental studies of band-related effects for BECs in optical lattices have been reported in [47, 48] as a natural progression of experiments performed in the late '90s studying Bloch oscillations, Wannier-Stark ladders and Landau-Zener tunnelling for ultracold (non-condensed) atoms in optical lattices [5]. These experiments have confirmed that the Bloch theory is indeed an excellent description of such systems, especially in the regime of low densities, where atom-atom interactions can be neglected. In this context, in Sec. 4.2 we present an experimental investigation of the energy spectrum of a BEC in a moving optical lattice, with a particular attention on how band-related effects can modify the dispersion of the matter wavepacket [31].

But this is only a part of the story. Let us now consider the role of interactions between the atoms forming a real condensate. As we have already discussed, the wave equation describing the condensate in the mean field approximation is the Gross-Pitaevskii equation

$$i\hbar\frac{\partial}{\partial t}\Psi(x,t) = \left[-\frac{\hbar^2}{2m}\frac{\partial^2}{\partial x^2} + V(x) + g|\Psi(x,t)|^2\right]\Psi(x,t)\ , \tag{1.40}$$

that includes a nonlinear interaction term. The presence of nonlinearities complicates the single-particle Bloch picture, leading to a rich variety of effects. For a generic periodic potential $V(x)$ extended states in the form of Bloch waves (1.27) are still stationary solutions of Eq. (1.40) and for a wide range of parameters the main features of the linear band structure are conserved. However, in the presence of strong nonlinearities, the single-particle energy spectrum is modified and loops appear in the Bloch bands [49, 50, 51] in the form of "swallow tails". The nonlinear Bloch waves corresponding to these extra solutions, a consequence of the superfluid nature of the system, correspond to arrays of dark or gray solitons with the same period of the lattice. A different class of stationary solutions includes periodic wavefunctions that do not satisfy the Bloch periodicity condition and have multiple period with respect to the lattice spacing [52]. Due to the nonlinear nature of the Gross-Pitaevskii equation also localized solutions exist, including isolated matter-wave gap solitons created in the gaps of the band spectrum [53, 54].

Not only nonlinearities are responsible for this wide collection of "exotic" states. In the presence of nonlinearities a fundamental problem arises regarding the *stability* of these solutions. Also restricting our attention to the extended Bloch states, a linear stability analysis of the Gross Pitaevskii equation shows that in large regions of the parameter space the Bloch waves become unstable against the growth of excitations that may drive the system away from the initial states. A detailed discussion of the main instability mechanisms is presented in Sec. 4.3, introducing an experiment, described in this thesis, devoted to the investigation of the different instability regimes for a BEC in a moving optical lattice [32, 33].

All these phenomena, that in the last years have attracted a lot of interest both from a theoretical and an experimental point of view, are derived within the frame of the Gross-Pitaevskii theory, that treats the condensate as a classical field. This approach has proven to give an excellent description of the system in the regime of weak lattice heights and for large site occupancy. However, in the tight binding regime, if the number of atoms per lattice site becomes small, the mean field treatment ceases to be valid and a full quantum theory, taking into account correlations between atoms, is required. The standard theoretical approach for the description of such systems is the Bose-Hubbard model [55, 56]. In second quantization, the Hamiltonian operator describing a bosonic system in a periodic potential is

$$\hat{H} = -K \sum_{\langle j,j' \rangle} \hat{b}_j^\dagger \hat{b}_{j'} + \frac{U}{2} \sum_j \hat{n}_j \left(\hat{n}_j - 1\right) + \sum_j \epsilon_j \hat{n}_j \ , \tag{1.41}$$

where $\hat{b}_j$ is the annihilation operator of one particle in the j-th site, $\hat{n}_j = \hat{b}_j^\dagger \hat{b}_j$ is the number operator, and $\langle j, j' \rangle$ indicates the sum on nearest neighbors. Each of the three terms on right-hand-side of Eq. (1.41) accounts for a different contribution to the total energy of the system: K is the *hopping energy*, proportional to the probability of quantum tunnelling between neighboring sites, U is the on-site *interaction energy*, giving a nonzero contribution only if more than one particle occupy the same site, and ϵ_j is a site-dependent energy accounting for external potentials superimposed on the lattice. We note that the Hamiltonian (1.41) contains two main approximations: it takes into account only a single (generally, the lowest) energy band and neglects all the couplings between the sites except for the one between nearest neighbors.

In the case $\epsilon_j = 0$ the ground state of the many-body system described by Eq. (1.41) depends on the balance between the two energy scales K and U. Assuming single site occupancy, when $U \ll K$ the system is in a superfluid state and the tunnelling ensures off-diagonal long-range coherence across the lattice. Instead, when $U \gg K$, the system is in a localized *Mott insulator* state, where long-range coherence is lost and number Fock states are created in the lattice sites. The transition between the superfluid state to a Mott insulator for ultracold atoms in a 3D optical lattice has been reported for the first time in [21, 57], where the ratio U/K was varied across the transition point by controlling the height of the lattice.

1.2.4 Josephson picture of the tight binding limit

In conclusion of this section, I would like to briefly introduce an alternative approach to the Bloch theory, based on the formalism used in the physics of Josephson junctions. Let us consider the tight binding limit $E \ll V_0$, where one can easily derive analytical results. Following the formalism of the Wannier functions, the time-dependent wavefunction describing a state in the lowest

energy band can be generally written as

$$\Psi(x,t) = \sum_{j=-\infty}^{\infty} \Phi_j(t)\Psi_j(x), \tag{1.42}$$

where $\Psi_j(x) = \Psi(x - jd)$ is the ground state of the j-th lattice site and

$$\Phi_j(t) = \sqrt{n_j(t)}e^{i\phi_j(t)} \tag{1.43}$$

is a complex function describing the amplitude $\sqrt{n_j}$ and the phase ϕ_j associated to the wavefunction in the j-th site. We assume for the sake of simplicity that the Wannier functions almost coincide with the ground state of the single potential well, which is strictly valid only for an infinitely high lattice. The functions $\Psi_j(x)$ are strongly localized at the lattice sites, with a small (but nonzero) overlap between functions $\Psi_j(x)$ and $\Psi_{j+1}(x)$ located at neighboring sites. Substituting this ansatz in Eq. (1.40) and neglecting the nonlinear interaction term, which is not relevant for the following discussions, we obtain a set of discrete Schrödinger equations for $\Phi_j(t)$:

$$i\hbar\frac{d\Phi_j}{dt} = -K\left(\Phi_{j-1} + \Phi_{j+1}\right), \tag{1.44}$$

in which we have defined a tunnelling rate

$$K = -\frac{\hbar^2}{2m}\int dx \left(\frac{\partial\Psi_j}{\partial x}\cdot\frac{\partial\Psi_{j+1}}{\partial x}\right), \tag{1.45}$$

calculated as an overlap integral between neighboring wavefunctions. In Eq. (1.44) we have only considered the tunnelling between nearest neighbors, neglecting all the other couplings. We note that K is a function of the lattice height, since the states $\Psi_j(x)$ implicitly depend on the shape of the potential.

Exact solutions of Eq. (1.44) are the usual Bloch waves, in which the complex functions $\Phi_j(t) = e^{i(jqd - Et/\hbar)}$ take the form of plane waves. In this case the phase difference between neighboring sites $\Delta\phi = \phi_{j+1} - \phi_j = qd$ is constant across the entire lattice and dependent on the quasimomentum state q. Substituting this Bloch ansatz in Eq. (1.44) one finds an analytical expression for the shape of the lowest energy band:

$$E = -2K\cos(qd). \tag{1.46}$$

Again, we can study the dynamics of a wavepacket in the presence of external forces. Following the definitions introduced in Sec. 1.2.2, the group velocity turns out to be

$$v = \frac{2Kd}{\hbar}\sin(qd) \tag{1.47}$$

and the effective mass

$$m^* = m\left(\frac{E_R}{K}\right)\frac{1}{\pi^2\cos(qd)}, \tag{1.48}$$

both dependent on the tunnelling rate K, which is the relevant quantity for the description of the dynamics of the system.

One can introduce collective coordinates $\bar{x}$ and $\Delta\phi$ describing, respectively, the wavepacket center of mass and the phase difference between neighboring sites. Defining the atomic current as $I = nv$, with n density of the gas, from Eq. (1.47) one can derive the simple expression

$$I = I_c \sin\Delta\phi, \tag{1.49}$$

which has the form of the current/phase relation holding for Josephson junctions, $I_c = 2Kdn/\hbar$ being a critical current that is directly proportional on the tunnelling rate K. Indeed, in this regime the system forms an array of Josephson junctions, i.e. a chain of quantum systems weakly linked by a tunnelling mechanism which preserves a phase coherence across the entire array. The current flowing in the array actually depends on the phase difference $\Delta\phi$ between adjacent sites, as in the case of a weak insulating junction between two semiconductors, in which the electronic current due to the quantum tunnelling through the barrier is proportional to the sine of the phase difference between the macroscopic wavefunctions in the two semiconductors. We note that Eq. (1.49) takes the form of a pendulum equation with the phase difference $\Delta\phi$ corresponding to the angle of the pendulum with respect to the vertical axis.

The phase dynamics is sensitive to the presence of forces driving the system out of equilibrium. If we apply a constant force $F = -\Delta V/d$ across the array, with ΔV difference of potential between adjacent sites, Eq. (1.36) becomes

$$\hbar\frac{d}{dt}\Delta\phi = -\Delta V. \tag{1.50}$$

This equation shows that a constant difference of potential ΔV produces a phase difference $\Delta\phi$ that grows linearly in time, hence, using Eq. (1.49), an ac-current oscillating at a frequency proportional to ΔV. This phenomenon, known as *Josephson effect*, is nothing but the transposition, in the language of phase-number conjugate variables, of the well known phenomenon of Bloch oscillations for a quantum particle in a periodic potential.

The experimental evidence for Josephson-like effects on matter waves in periodic potentials has been obtained in [17] through the study of macroscopic quantum interference and in [20] through the investigation of the transport properties of a BEC in an optical lattice. We note that the Josephson approach is particularly suitable in the case of high lattice heights, when the total wavefunction can be expanded in the sum of many localized wavefunctions. In the case of low lattice heights, when the wavefunction is just weakly

modulated and we cannot neglect the overlap integral between more distant neighboring sites, the tunnelling rate K loses most of its physical meaning. In this case other energy scales K', K'', etc. describing longer range couplings should be included in Eq. (1.44) and the simple form of the energy spectrum in Eq. (1.46) will get more complicated.

Chapter 2

Experimental setup

In this chapter we describe the main features of the ^{87}Rb BEC apparatus working at LENS since 1999. During this PhD work the setup has been moved from the previous location of the laboratory (the hill of Arcetri in Florence) to the new location (the new university building in Sesto Fiorentino). All the optical part of the setup has been dismantled and then reassembled, with the installation of new laser sources, new locking schemes and a new detection system. The vacuum system and the magnetic trap, as well as most of the electronics, are the same working since the first BEC in 1999. More details on the experimental setup can be found in [58, 59, 60, 61, 62].

2.1 Laser cooling

The development of laser cooling and trapping techniques has been one of the major advances in atomic physics of the last century, as also acknowledged by the award of the Nobel Prize in Physics in 1997 [63, 64, 65]. The first proposal to use laser light to cool atomic ensembles dates back to 1975 [66]. Starting from the early '80s, many striking experimental results showed the possibility to cool ensembles of neutral atoms to the microkelvin regime, much below the lowest temperatures attainable with standard cryogenic techniques, thus opening the possibility to reach Bose-Einstein condensation of atomic gases.

However, laser cooling alone is not sufficient to achieve Bose-Einstein condensation. Most of the laser cooling techniques suffer a fundamental limit, that is connatural with the cooling mechanism itself, namely the exchange of photons with the radiation field. The lowest temperature achievable with laser cooling is the recoil temperature $T_R = \hbar^2 k^2 / m k_B$ (for rubidium ~ 350 nK) corresponding to the energy acquired in a photon absorption process. This limit, together with the low densities typically achievable with such techniques (of the order of 10^{10} atoms/cm^3), makes a further cooling mechanism necessary for the achievement of quantum degeneracy.

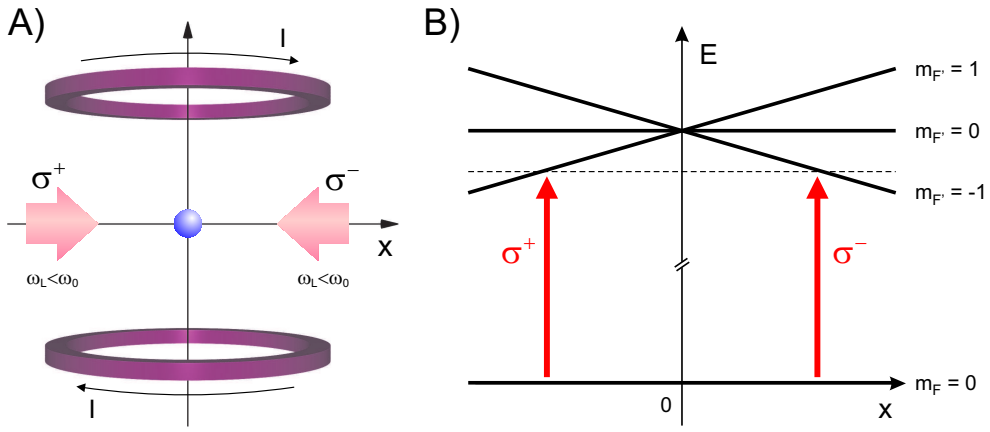

Figure 2.1: Principle of operation of a magneto-optical trap (MOT) in a simplified 1D configuration. A) An atom is trapped in the presence of a quadrupole magnetic field and of two red-detuned counterpropagating laser beams with opposite circular polarization. B) Energy-level diagram of a hypothetical atom having $F = 0$ ground state and $F' = 1$ excited state in the presence of a magnetic field gradient.

The solution adopted in the first BEC experiments to overcome this problem is the use of magnetostatic traps, that provide a conservative confining potential where evaporative cooling can be performed. This clever technique relies on the selective expulsion of the most energetic atoms from the trap and on the subsequent rethermalization of the sample at lower temperatures. However, in order to efficiently load a magnetic trap, a precooling stage is required, and laser cooling is the most powerful way to do it.

2.1.1 Magneto-optical traps

Magneto-optical trapping is the fundamental brick of all the running BEC systems (with the notable exception of hydrogen [67]), providing the first fundamental cooling step in the route to quantum degeneracy. A magneto-optical trap (MOT) is a device composed by a spherical quadrupole magnetic field, generally created by a pair of coils placed in anti-Helmoltz configuration, and three pairs of counterpropagating red-detuned laser beams intersecting orthogonally in the region of zero magnetic field, in such a way that beams aligned along the same axis have opposite circular polarization.

The principle of operation of a magneto-optical trap can be analyzed in a simplified 1D geometry, as illustrated in Fig. 2.1A. Let us consider two coils producing a uniform magnetic field gradient in the center of the trap and two laser beams with opposite circular polarization σ^+ and σ^- directed along $\hat{x}$ in such a way that the σ^+ beam propagates in the direction of increasing field.

We consider the case of an hypothetical atom having a ground state $F = 0$ and an excited state $F' = 1$ with a hyperfine threefold $m_{F'} = -1, 0, 1$. In Fig. 2.1B we show the energies of the atomic states taking into account the position-dependent Zeeman shift of the excited levels

$$\Delta E(x) = g_{F'} \mu_B m_{F'} B(x), \tag{2.1}$$

where $g_{F'}$ is the Landé factor of the excited state, μ_B is the Bohr magneton and $B(x) = bx$ is the quadrupole magnetic field, in which the gradient b is chosen in such a way that $g_{F'} b > 0$. Let us consider an atom located at $x > 0$. Because of the position-dependent Zeeman shift induced by the quadrupole field, the atom will preferentially absorb a photon from the σ^- field, because the red-detuned light is more in resonance with the $m_F = 0 \rightarrow m_{F'} = -1$ transition. As a consequence of the momentum transfer in the atom-photon interaction (with a directional stimulated absorption and a subsequent isotropic spontaneous emission), the atom will experience a net force directed towards the trap center. In the case of an atom located at $x < 0$ the situation is reversed. In this case the most probable process is absorption from the σ^+ field, that still produces a net force directed towards the trap center. In addition, since the two beams are red-detuned, this restoring force is accompanied by a viscous force, as the one produced in optical molasses. The total force exerted on the atom is

$$F = -m\omega^2 x - \gamma v, \tag{2.2}$$

that describes a damped harmonic oscillator. It has been experimentally verified that the above considerations are still valid in the 3D case, when cooling beams are applied also in the orthogonal directions, and for atoms with a more complex electronic configuration. We note that the typical field gradients used in a MOT are very weak and the interaction $-\mu \cdot \mathbf{B}$ with the atomic magnetic dipole (see Sec. 2.2) plays a negligible role.

The original proposal for the realization of a magneto-optical trap was presented by J. Dalibard in 1986 [63]. The first operating MOT was realized in 1987 starting from a decelerated beam of sodium atoms [68] and, in the later years, it has been demonstrated that it is possible to trap the atoms in a MOT directly from a room-temperature vapor [69].

2.1.2 Rubidium energy levels

Rubidium, as all the other alkali metals, has a simple hydrogen-like electronic structure, which is determined only by the quantum numbers of the weakly bound outer electron. Indeed, the core electrons packed in the inner filled shells can be excited only with strongly energetic photons well outside the visible part of the spectrum, and can therefore be ignored. Rubidium has two natural isotopes, with mass numbers 85 and 87, and relative abundances 72% and 28% respectively. Both the isotopes have a nonzero nuclear spin, hence

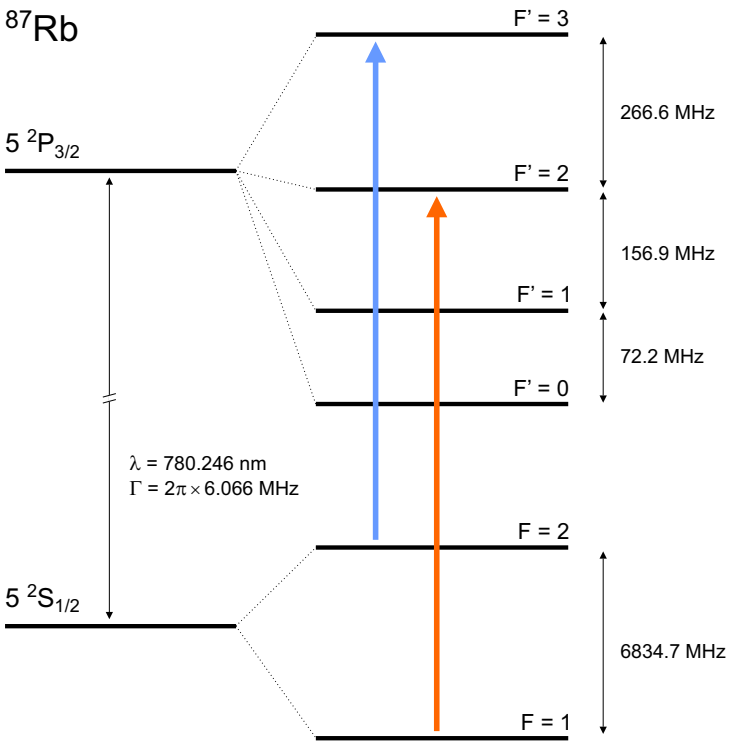

Figure 2.2: Hyperfine structure of the ^{87}Rb D2 transition. The arrows indicate the cooling transition $F = 2 \rightarrow F' = 3$ and the repumping transition $F = 1 \rightarrow F' = 2$ excited in the MOT operation.

the hyperfine structure of the states must be taken into account. In the case of ^{87}Rb the nuclear spin is $I = 3/2$ and the ground state $5^2S_{1/2}$ is split into two hyperfine levels with total angular momentum $F = 1$ and $F = 2$, separated by a ~ 6.8 GHz frequency interval.

Magneto-optical trapping of ^{87}Rb is made on the D2 line connecting the fine structure states $5^2S_{1/2}$ and $5^2P_{3/2}$ at a wavelength $\lambda = 780.246$ nm. In Fig. 2.2 we show the hyperfine manifolds of both the ground and the excited state [70]. The cooling transition is the $F = 2 \rightarrow F' = 3$, since this is the strongest closed transition of the hyperfine structure. However, since the hyperfine splitting of the excited state is quite narrow, the residual excitation of atoms into the state $F' = 2$ constitutes a strong loss channel, because atoms may decay from this state into the uncoupled $F = 1$ hyperfine ground state. For this reason an additional *repumping* laser is used in resonance with the transition $F = 1 \rightarrow F' = 2$ to recycle the lost atoms into the ground state $F = 2$ through the relaxation channel $F' = 2 \rightarrow F = 2$.

2.1.3 Laser sources

The laser light used to excite both the cooling and the repumping transitions comes from diode laser sources. The diode lasers are mounted in a Littrow extended cavity configuration [71], that provides optical feedback to the laser, reducing the threshold current, narrowing the linewidth of the emission and providing broad tunability. In these home-made cavities the laser light emitted by the diode is collimated by a lens placed in front of the diode facet and is sent onto a diffraction grating, which both provides the optical feedback and behaves as the wavelength-selective element. In the Littrow configuration the first order diffracted beam (containing $\sim 10\%$ of the output power) goes directly back into the diode to provide the feedback, while the zeroth order reflected beam, containing most of the output power, is outcoupled from the cavity and used in the experiment. Manually changing the angle of the grating with respect to the laser emission provides a coarse wavelength tuning within the emission curve of the diode. Fine tuning of the laser wavelength and mode is accomplished by changing the operating current and temperature. Even finer tuning (from a few MHz to 5 GHz) is possible by controlling the voltage of a PZT acting on the diffraction grating mounting. We use laser diodes SANYO DL7140-201 operating at a typical current 70 mA, provided by a stabilized current generator, and temperature 16 °C, kept constant by a Peltier cell placed inside the cavity and driven by a stabilization circuit. The laser light outcoupled from the extended cavity has a typical power of 20 mW and a linewidth of ≈ 300 kHz.

The diode laser used to excite the cooling transition is the master oscillator for a commercial tapered amplifier TOPTICA TA100. Such a device, commonly called MOPA (*Master Oscillator Power Amplifier*), is capable of single-pass amplification of the light coming from the master oscillator fully preserving its spectral characteristics. The output power of the MOPA, when operating with a current of 1.3 A and injected with 15 mW of laser light, is of the order of 700 mW.

In order to run a magneto-optical trap the laser light working on the cooling transition must have a narrow linewidth and an absolutely stable frequency. The first requirement is guaranteed by the extended cavity configuration, which narrows the spectral width of the free-running laser well below the linewidth of the cooling transition (~ 6 MHz). The second requirement can be satisfied only by a stabilization technique which actively locks the laser emission onto a stable reference. To accomplish this task a fraction of the beam coming out from each of the laser sources is used to make saturation spectroscopy on a cell filled with Rb vapor. A frequency modulation technique allows us to use the first derivative of the absorption signal as the dispersive signal for the locking scheme. The feedback loop is closed by acting on the PZT controlling the position of the diffraction grating in the extended cavity. The cooling laser is locked 140 MHz below the $F = 2 \rightarrow F' = 3$ transition,

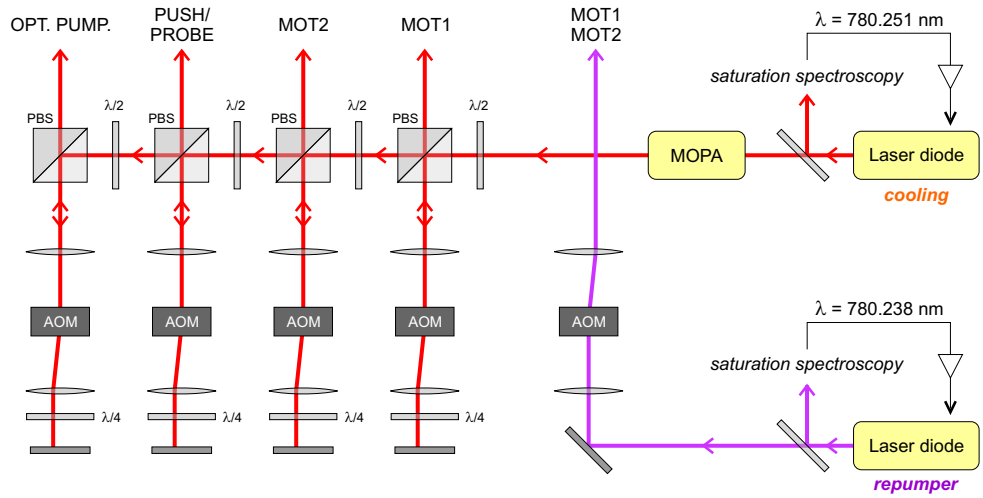

Figure 2.3: Laser sources and optical system for the control of the frequency and the intensity of the beams used in the experiment.

while the laser beam is locked on the crossover between the $F = 1 \rightarrow F' = 1$ and the $F = 1 \rightarrow F' = 2$ transition, ~ 80 MHz below the latter transition.

In Fig. 2.3 we show the scheme used for the control of the frequencies and the intensities of all the beams used for the production and the detection of Bose-Einstein condensates. Since we use a double-MOT system (see Sec. 2.1.4), we need cooling and repumping beams for two different magneto-optical traps (MOT1, MOT2) and a beam for the transfer of atoms between the two MOTs (PUSH). Furthermore, we need a beam to optically pump the atoms into a magnetically trappable state (OPT. PUMP.) and a beam for the imaging of the condensate (PROBE). With the exception of the repumping beams, which have a frequency much different from the frequency of the other beams and thus need to be obtained from an independent laser source, all the beams used in the experiment are derived from the same cooling laser. The beam coming out from the MOPA is sent through a series of adjustable splitters made up by a $\lambda/2$ plate and a polarizing beam-splitter cube. Acousto-optic modulators (AOMs) are used both to finely set the frequency of the beams and to modulate their intensity, in order to meet the requests of the different experimental phases. In the case of the beams derived by the cooling laser the AOMs are used in double pass configuration: the first order diffracted beam is retroreflected by a mirror and sent again through the AOM. The output beam is then separated from the incoming beam with the use of polarization optics. The double-pass system provides the advantage that, whenever the radiofrequency driving the AOMs is changed, the optical path of the output beam is not affected, independently from the variation of the deflection angle.

The drawback of this scheme is a loss of power due to the AOM $\sim$ 80% efficiency at each passage. The necessity to have a well defined optical path independently from the modulation frequency is particularly important for the alignment of the MOT cooling beams, whose detuning from the resonance has to be set to different values while transferring the atoms from the magneto-optical trap to the pure magnetostatic trap.

2.1.4 Double-MOT system

A good vacuum system is a fundamental requirement for the success of a Bose-Einstein condensation experiment. Indeed, since the typical temperatures of the trapped gas are of the order of 1 μK or even less, a perfect thermal isolation of the sample from the environment is necessary. This is particularly important in the magnetic trapping phase, when long lifetimes and minimal heating are essential demands for the good operation of evaporative cooling (see Sec. 2.2.4). The most important sources of losses and heating for a cloud of trapped atoms are the collisions with the background gas, that is in thermal equilibrium with the room-temperature walls of the vacuum cell. This process can be reduced by bringing the pressure in the cell below 10^{-10} mbar in the ultra-high-vacuum (UHV) regime.

This requirement is in contrast with the necessity to start the evaporative cooling with a large number of trapped atoms. Actually, if the atoms trapped in the MOT are captured directly from the background gas, a larger pressure would provide a higher number of trapped atoms. One of the typical solutions to this problem is to work with a double-MOT apparatus, in which two magneto-optical traps are produced in two separate cells with different pressure. The strategy is the following: in a first MOT, working in a moderate UHV environment, many atoms as possible are captured from the background gas; these cold atoms are then transferred into a second cell, at deep UHV, in which they are recaptured in a second MOT. In the same cell the atoms are then loaded in the magnetostatic trap for the evaporative cooling stage.

First MOT. In Fig. 2.4 we show a schematic top view of the two vacuum chambers used in the experiment. A first steel chamber (on top of the figure) is used to produce a first MOT in which the atoms are captured directly from the background gas. In this chamber we measure a pressure of the order of 10^{-9} mbar, kept constant by an ion pump Varian VacIon Plus 25 with a pumping speed of 25 l/s. The chamber is connected to a cell containing a sample of solid rubidium in equilibrium with its saturated vapor pressure, and an adjustable valve is used to regulate the amount of vapor being sent into the chamber. The three MOT cooling beams, one for each orthogonal axis, are retroreflected by curved mirrors placed after the cell windows, in order to slightly focus them back in the center of the chamber to compensate for the

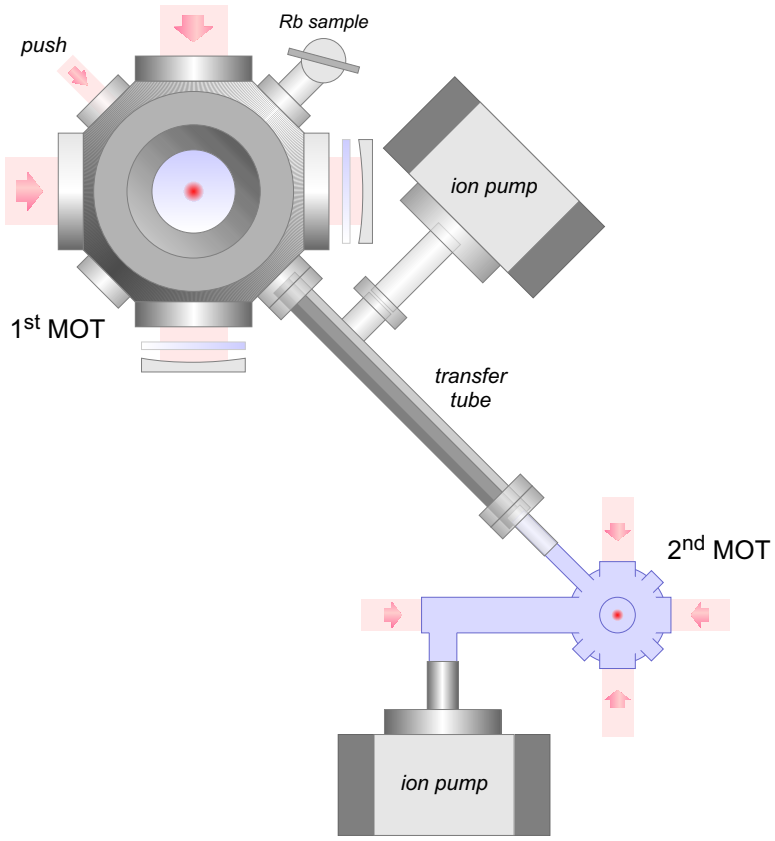

Figure 2.4: Schematic top view of the vacuum system used in the experiment. A steel chamber, used to produce a first MOT, is connected to a glass cell, in which the atoms transferred from the first MOT are recaptured in a second MOT and then loaded into the magnetic trap.

absorption of the first passage. Each of the MOT beams is red-detuned 12 MHz (2Γ) from the resonance, has a diameter of $\sim$ 3 cm and a power of 20 mW. The repumping light necessary for the MOT is superimposed on the path of the cooling beams and has a total power of 8 mW. The quadrupole field for the MOT is created by two coils mounted with vertical axis in an anti-Helmoltz configuration. The coils, made up of circular windings of copper wire with 0.8 mm diameter, produce a magnetic field gradient of 7 Gauss/cm with a current of 4 A. Three larger compensation coils are used to cancel the earth magnetic field and other spurious fields (including the one produced by the ion pumps). In this first MOT we typically capture $\sim 10^{10}$ atoms at a temperature of $\sim$ 100 μK, with a loading time $\sim$ 5 s. The diagnostic of the MOT is made with a photodiode, measuring the fluorescence of the trapped atoms, and a CCD camera, used to control the MOT shape and position.

Second MOT. The first chamber is connected to a second glass cell via a steel tube with a diameter of 11 mm. This narrow pipe allows the maintenance of a differential vacuum between the two cells, which is essential for the good operation of the system. A second ion pump Varian VacIon Plus 55, with a pumping speed of 55 l/s, is connected to the glass cell and maintain a pressure of the order of 10^{-11} mbar, necessary for the good operation of the magnetostatic trap which is created in the same cell. A titanium sublimation system Varian 916-0017 is periodically used to improve the quality of the vacuum by removing the Rb atoms stuck to the cell walls. In this second chamber, instead of using three orthogonal MOT beams retroreflected after the passage from the cell, we use six independent beams with the possibility of independent alignment. Although we lose half of the available power, this design allows us to precisely control the intensity and alignment of each of the six MOT beams, and this is particularly important during the transfer from the MOT to the magnetostatic trap, where an optical molasses phase is used to increase the phase-space density. Each of the MOT beams is red-detuned 12 MHz (2Γ) from the resonance, has a diameter of 2 cm and a power of 10 mW. The repumping light necessary for the operation of the MOT is superimposed on the path of the cooling beams and has a total power of 8 mW. The quadrupole field for the MOT is generated by the same magnetic trap coils described in Sec. 2.2.1, which produce a magnetic field gradient of 10 Gauss/cm, and three pairs of compensation coils are used to cancel spurious magnetic fields. The latter coils, mounted in Helmoltz configuration, are also used in the magnetic trapping phase to set the value of the magnetic bias field (see Sec. 2.2.1). Due to the ultra-high vacuum present in this cell, capture of rubidium atoms from the background gas is strongly suppressed and the MOT is loaded from the atoms precooled in the first chamber and then transferred into the second cell.

The transfer of atoms between the first and the second MOT is accomplished by a laser beam (*push beam*) directed along the axis of the transfer tube and slightly focused near the center of the glass cell where the second MOT is produced. The push beam is slightly misaligned from the center of the second MOT in order not to hit the atoms already captured in the trap. The beam is derived from the same laser source producing the MOT cooling beams (see Fig. 2.3), is σ^+ circularly polarized and is 3 MHz red-detuned with respect to the cooling transition. The experimental sequence used to transfer atoms from the first to the second MOT is the following. We load the first MOT for 200 ms, then we switch off the quadrupole field and apply a short molasses phase in order to further cool the trapped atoms. The push beam is then switched on for 3 ms, exerting a force on the atoms in the direction of the second cell. The atoms, optically pumped in the state $|F = 2, m_F = 2\rangle$, are guided along the axis of the transfer tube by an exapolar magnetic field produced by permanent magnets. When the atoms reach the second cell they

are captured by the second MOT. Then the quadrupole field of the first MOT is switched on and the sequence starts again. The loading of the second MOT takes ~ 300 shots, for a total loading time of ~ 60 s, after which the number of atoms saturates. In this way we typically load the second MOT with $\sim 10^9$ atoms at a temperature ~ 100 μK. The diagnostic of the MOT is made, as in the case of the first MOT, with a photodiode and a CCD camera.

Towards magnetic trapping At the end of the MOT loading procedure, before transferring the atoms into the magnetic trap, we use a further cooling stage in order to increase the phase-space density of the sample. First, we reduce the magnetic field gradient from 10 Gauss/cm to 6 Gauss/cm, thereby increasing the detuning of the cooling beam from 12 MHz to 24 MHz. Then, after 20 ms of such a MOT phase, we switch off the quadrupole magnetic field for a 5 ms long optical molasses phase, in which the power of the cooling beams is decreased from 10 mW to 5 mW and the detuning is increased from 24 MHz to 48 MHz. This sub-Doppler polarization-gradient cooling decreases the temperature of the sample to ~ 50 μK, bringing it to a phase-space density 10^{-7}. At this time the cold atomic sample is ready to be magnetically trapped.

2.2 Magnetic trapping

The development of laser cooling techniques has been a fundamental milestone on the path to the modern BEC experiments, but the decisive breakthrough was the development of magnetic trapping techniques, which allowed the implementation of evaporative cooling and the final achievement of quantum degeneracy in neutral atoms. The first experimental evidence for magnetic trapping of neutral atoms was reported in [72] for a beam of sodium atoms optically decelerated in a Zeeman slower. A pre-cooling stage is indeed a fundamental requirement for loading magnetic traps, since the depth of these traps is generally quite small, of the order of tens of mK with convenient magnetic fields.

Magnetic trapping is based on the interaction of the atomic magnetic dipole moment μ with an inhomogeneous magnetic field $\mathbf{B}(\mathbf{r})$. Classically, the interaction energy $U(\mathbf{r})$ is given by [73]

$$U(\mathbf{r}) = -\mu \cdot \mathbf{B}(\mathbf{r}). \tag{2.3}$$

If the atom is moving slowly enough, so that we can neglect the magnetic field variation on the timescale set by the Larmor frequency ω_L, we can assume that the dipole moment adiabatically follows the direction of the field. In this approximation, the scalar product $-\mu \cdot \mathbf{B}$ can be substituted with the product of the modula and Eq. (2.3) becomes

$$U(\mathbf{r}) = g_F m_F \mu_B \left|\mathbf{B}(\mathbf{r})\right|, \tag{2.4}$$

where we have expressed the magnetic dipole moment μ in terms of the Bohr magneton μ_B, the hyperfine Landé factor g_F and the projection of the total angular momentum on the quantization axis m_F. The Wing theorem [74] states that a region of space free from currents cannot sustain a field maximum, but only a field minimum. Hence, in order to trap the atoms in a minimum of the potential (2.4), the product $g_F m_F$ has to be positive. In the case of ^{87}Rb the Landé factors for the two hyperfine components of the ground state are $g_1 = -1/2$ for the $F = 1$ state and $g_2 = 1/2$ for the $F = 2$ state. As a consequence, only the low-field-seeking states $|F, m_F\rangle = |1, -1\rangle$, $|2, 1\rangle$, $|2, 2\rangle$ can be magnetically trapped.

2.2.1 Trap geometry

The magnetic trap used in our experiment is a modification of the traps employed in [75] and [76]. The magnetic field produced in these traps shares the same features as the one obtained with the Ioffe–Pritchard configuration proposed in [77], i.e. it is a static field and it varies harmonically around a nonzero local minimum. The importance of having a nonzero minimum is caused by the fact that in this way one can avoid the complication of losses due to Majorana spin-flips [78] into untrapped states when the atoms cross a region with vanishing field.

Our trap is created by four different circular coils, as schematically illustrated in Fig. 2.5. The coils Q1 and Q2, made up of 15 windings with a diameter from 3 to 6 cm, are aligned along the vertical axis $\hat{y}$ at the same distance $a' = 3.2$ cm from the center of the vacuum cell. The current I_Q flowing through them in opposite directions produces a quadrupole field in the center, that is also used in the MOT phase. The coil C, with the same diameter and number of windings, is aligned along the orthogonal axis $\hat{z}$ at a distance $a = 4$ cm from the center of the cell. The coil A, instead, is made up of 6 larger windings with 12 cm diameter and is placed at $a'' = 3.2$ cm from the center of the cell. The same current I_C circulates in the coils C and A, but in opposite directions. All these coils are made with copper hollow tube with 3 mm diameter, used both to carry the current and to allow the water flow used to cool the structure. This trap is designed to work with high currents ($I = 240$ A) requiring a power consumption of more than 2 kW, that is dissipated by the water flowing inside the same coils.

Let us derive some analytical expression for the magnetic field generated by the trap coils Q1, Q2 and C, assuming that they have all the same radius R and are at the same distance $a = a'$ from a common center. The following analysis, based on a very simple model, allows us to illustrate the main features of this trap geometry and will be useful for the description of the experiments in the next chapter.

Let us first consider the magnetic field generated by the current I circulating in a coil of radius R, in the ideal case in which the transverse size of the

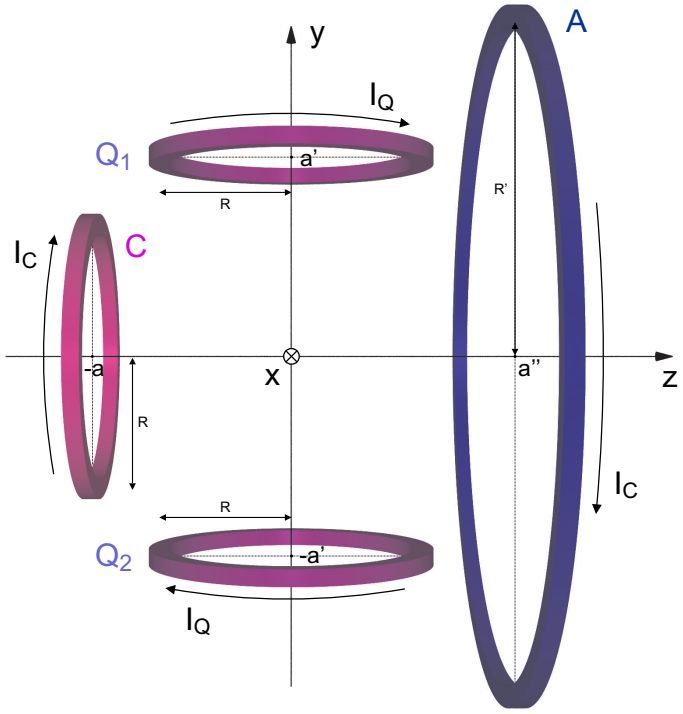

Figure 2.5: Magnetic trap geometry. Distances, size and thickness of the coils have not the right proportions.

conductor can be neglected. We introduce cylindrical coordinates ξ, indicating the position along the coil axis, and ρ, indicating the radial distance from the axis. From classical electrodynamics textbooks [73], it is possible to derive an analytical expression for the induction field along the axis

$$B(0,\xi) = \frac{\mu_0 I R^2}{2} \frac{1}{[R^2 + (\xi - a)^2]^{3/2}} \hat{\mathbf{e}}_\xi, \tag{2.5}$$

where a is the position of the coil along the axis and $\hat{\mathbf{e}}_\xi$ is the unit vector parallel to the axis. Expanding Eq. (2.5) to the second order in ξ we find

$$B(0,\xi) = \left[b_0 + b_1\xi + b_2\xi^2\right] \hat{\mathbf{e}}_\xi, \tag{2.6}$$

The magnetic field in the proximity of the axis can be calculated introducing corrective terms in ρ^n and forcing the resulting expression to satisfy the Maxwell equations $\nabla \cdot \mathbf{B} = 0$ and $\nabla \times \mathbf{B} = \mathbf{0}$. Expanding to the second order in ξ and ρ one finds

$$B(\rho,\xi) = \left[b_0 + b_1\xi + b_2\xi^2 - \frac{1}{2}b_2\rho^2\right] \hat{\mathbf{e}}_\xi + \left[-\frac{1}{2}b_1\rho - b_2\xi\rho\right] \hat{\mathbf{e}}_\rho, \tag{2.7}$$

where $\hat{\mathbf{e}}_\rho$ is the unit vector orthogonal to the axis. Writing similar expression for the induction field generated by the three trap coils and introducing cartesian coordinates one finds that the total field near the origin is

$$B(x,y,z) = \begin{pmatrix} B_x \\ B_y \\ B_z \end{pmatrix} = \begin{pmatrix} -(b_1' + \frac{1}{2}b_1)x - b_2 xz \\ (2b_1' - \frac{1}{2}b_1)y - b_2 yz \\ b_0 + (b_1 - b_1')z + b_2(z^2 - \frac{1}{2}x^2 - \frac{1}{2}y^2) \end{pmatrix}, \quad (2.8)$$

where b_0, b_1 and b_2 are the coefficients of the field generated by the curvature coil C and b_1' is the gradient of the field generated by each of the two coils Q1 and Q2 (in this case the 0^{th} and 2^{nd} order of the expansion cancel, because the two coils are equidistant and the currents flow in opposite directions). The modulus of the magnetic field, neglecting terms $O(r^3)$, is

$$|B(x,y,z)| = B_0 + B_x x^2 + B_y y^2 + B_z (z - z_0)^2 \quad (2.9)$$

where we have defined the following quantities:

$$\begin{cases} B_0 = b_0 - \frac{(b_1' - b_1)^2}{4b_2} \\ B_x = \frac{(b_1' + \frac{1}{2}b_1)^2}{2b_0} - \frac{b_2}{2} \\ B_y = \frac{(2b_1' - \frac{1}{2}b_1)^2}{2b_0} - \frac{b_2}{2} \\ B_z = b_2 \\ z_0 = \frac{b_1' - b_1}{2b_2} \end{cases} \quad (2.10)$$

In the case in which the three coils are all equidistant from the origin and the same current I flows in them, we have $b_1' = b_1$ and Eq. (2.9) reduces to

$$|B(x,y,z)| = b_0 + \left(\frac{9b_1^2}{8b_0} - \frac{b_2}{2}\right)\left(x^2 + y^2\right) + b_2 z^2. \quad (2.11)$$

In this simple derivation the modulus of the magnetic field has a minimum in the origin and it changes harmonically in all directions. The geometry of the trap is cylindrical, with the axis coincident with the axis of the curvature coil. The trap frequencies are

$$\omega_z = \sqrt{\frac{2g_F\mu_B m_F}{m} B_z} \propto \sqrt{b_2} \quad (2.12)$$

$$\omega_\perp = \sqrt{\frac{2g_F\mu_B m_F}{m} B_{x,y}} \propto \sqrt{\frac{9b_1^2}{8b_0} - \frac{b_2}{2}} \sim \sqrt{\frac{b_1^2}{b_0}} \quad (2.13)$$

While the axial trap frequency ω_z is set by the second order term of the curvature field, the radial trap frequency $\omega_\perp$ depends on the gradient of the curvature field and on the bias field b_0. This means that it is possible to change the radial frequency simply adding a uniform magnetic field. For this

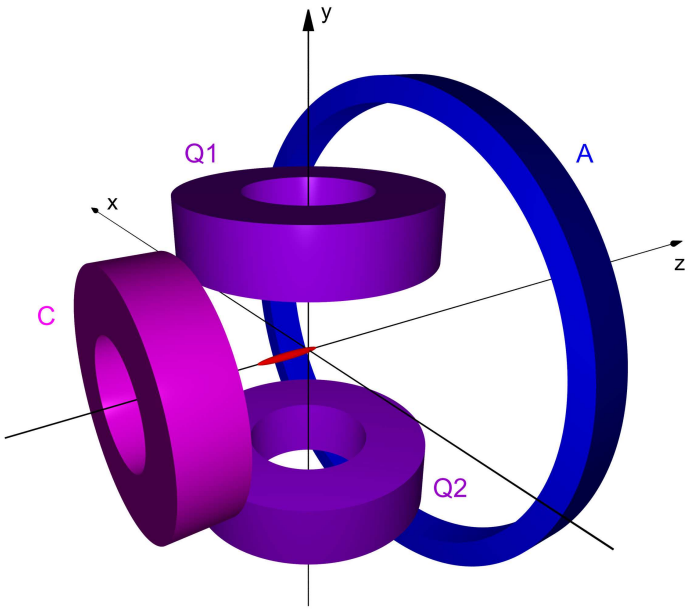

Figure 2.6: 3D model of the magnetic trap setup (in scale). The central ellipsoid represents the cigar-shaped trapped cloud.

reason the trap is equipped with the fourth *antibias* coil A which is used to lower the bias field in order to increase the radial confinement. The size of this coil is bigger, in such a way not to affect gradient and curvature of the field produced by the other trap coils. The current flowing in this coil is the same as the one circulating in the curvature coil, but in the opposite direction. The fine tuning of the bias field is accomplished by using the same Helmoltz compensation coils that in the MOT phase (see Sec. 2.1.4) are used to cancel spurious magnetic fields.

Actually, the trap configuration used in the experiment is slightly different from the above analysis, because the quadrupole coils Q1 and Q2 are some millimeters closer to the cell than the curvature coil C, in order to further increase the confinement. This configuration produces a ~ 6 mm displacement of the trap center along the $\hat{z}$ direction towards the curvature coil. Despite this difference, the above analysis well reproduces the main features of the actual trap configuration used in the experiment. In the standard operation, the current circulating in the four trap coils is $I = 235A$, the bias field is $B_0 \simeq 2.5$ G and the (measured) trap frequencies for the atoms in the hyperfine state $|F = 1, m_F = -1\rangle$ are

$$\omega_z = 2\pi \times 8.8 \text{ Hz}$$
$$\omega_\perp = 2\pi \times 90 \text{ Hz}$$

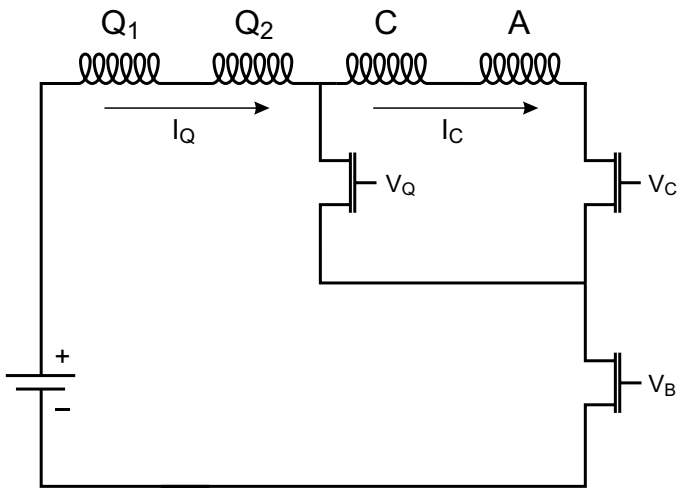

Figure 2.7: Circuital scheme of the magnetic trap. Q1 and Q2 represent the two quadrupole coils, while C and A represent, respectively, the curvature and the antibias coils. Three blocks of MOSFETs are used to control the currents flowing in the trap coils.

2.2.2 Magnetic trap control

The current necessary for the operation of the magnetic trap is given by a commercial high-current power supply HP 6681A, internally modified in order to reach a maximum current 250 A with a maximum voltage 11 V. The scheme in Fig. 2.7 shows the connections of the four trap coils and the circuit used to control the trap currents. The generator is computer controlled via GPIB interface. We use three blocks of high-power MOSFETs STE180N10 as voltage-controlled switches, in which the current flowing between *drain* and *source* can be regulated by the voltage applied to the *gate*. Each block is made up of four such devices mounted in parallel to sustain higher currents. The blocks controlled by the voltages V_C and V_Q (see Fig. 2.7) are used to change the trap geometry from the pure quadrupole configuration (as in the MOT phase, with current flowing only in Q1 and Q2) all the way to the Ioffe configuration (with an equal current flowing in all the four coils).

The block controlled by the signal V_B is instead used as a current regulator. In the routine operation of the magnetic trap we need to use current ramps or to quickly commute between different current values. The slow response of the power supply, combined with the poor temporal resolution of the GPIB interface, does not allow a good execution of these tasks. For this reason we use a feedback circuit that compares the actual current, measured by a sensor integrated in the power supply, with a programmed value. The difference between these two values is the error signal, that is processed by an analog

circuit and then applied to the gate of the MOSFETs (V_B), which regulate the current flowing in the circuit, thus closing the stabilization loop. The same MOSFET block is also used for fast commutation (~ 500 μs) of the trap currents in the critical phases of the trap switching on and off.

2.2.3 Loading the magnetic trap

After the molasses phase the atoms are optically pumped in the low-field-seeking state $|F = 1, m_F = -1\rangle$, that can be trapped in a magnetic field minimum. The procedure used in the experiment is the following. At the end of the molasses stage we first switch off the cooling beam, then after 200 μs we switch off also the repumper beam, in such a way to optically pump the atoms in the hyperfine state $F = 2$. In order to populate the state $|F = 1, m_F = -1\rangle$ we switch on a weak magnetic field along the direction of the trap axis, in such a way to define a quantization axis, then apply a 200 μs-long pulse of a σ^- polarized beam travelling in the same direction of the magnetic field. This optical pumping beam, derived from the cooling laser (as shown in Fig. 2.3), is resonant with the $F = 2 \rightarrow F' = 2$ transition and forces the atoms to decay back into the $F = 1$ state, with a bias towards the Zeeman state $m_F = -1$. This sequence has been experimentally adopted and optimized in order to transfer the highest number of atoms in the state $|F = 1, m_F = -1\rangle$, with an efficiency better than 50%.

After this optical pumping phase we capture the atoms in a pure quadrupole trap, produced by a current $I = 70$ A flowing in the Q1 and Q2 coils, corresponding to a gradient $2b'_1 = 70$ G/cm in the vertical direction and $b'_1 = 35$ G/cm in the two radial directions. This field gradient has been chosen to maximize the phase-space density of the atomic cloud captured in the trap [59]. If the field gradient is too small, it will not provide the necessary confinement and will decrease the phase-space density of the sample (being eventually overcome by the gravitational gradient). An excessive field gradient would strongly compress the cloud, thereby increasing its energy.

Once the atoms are captured in the weak quadrupole trap, the current in the quadrupole coils is adiabatically ramped to $I = 235$ A in 300 ms, then the modification of the quadrupole trap into the Ioffe-Pritchard trap takes place. The MOSFETs controlled by V_C are closed (see Fig. 2.7), while the ones controlled by V_Q are gradually opened in 400 ms, in such a way to let the current flow in the C and A coils too. Again, it is important that these trap modifications take place slowly enough not to induce heating of the atomic cloud. At the end of this process, the maximum current $I = 235$ A flows in all the four trap coils: the atoms are confined in the Ioffe-Pritchard trap and the evaporative cooling can start.

The lifetime of the thermal sample in the magnetic trap is of the order of ~ 90 s, with a heating rate ~ 30 nK/s. The lifetime is an important issue, because an efficient evaporative cooling requires quite long thermalization

times. In the case of ^{87}Rb the collisional properties are particularly good and inelastic processes due to three-body collisions between the trapped atoms can be neglected at the typical densities achievable in a magnetic trapped cloud. Here we report some common instrumental effects limiting the lifetime which we have encountered during the work:

- A first source of losses is collisions with the background gas. These collisions are highly energetic, since the background gas is in thermal equilibrium with the cell at room temperature, and may cause the atoms to escape from the trap. In order to limit the effect of these collisions, maintaining a good ultra-high vacuum is a fundamental task.

- A second source of heating is caused by the presence of resonant light that can be absorbed by the atoms, which get excited and then may decay back into untrapped states. Also the momentum imparted to the atoms in the photon absorption and emission processes heats the sample. During the magnetic trapping phase we block the laser beams with mechanical shutters, to ensure the complete extinction of resonant light that the AOMs cannot guarantee. We also keep the laboratory windows closed, since we found that the sunlight spectrum contains enough radiation at 780 and 795 nm to prevent the condensation.

- A third source of heating is related to the short-term stability of the magnetic field. If the currents flowing in the trap coils have fast fluctuations (on the typical timescales $\approx$ 10 ms of the trap dynamics) the atoms cannot adiabatically follow the variation of the magnetic field and probe an effective shaking of the trap, that can transfer energy to the external degrees of freedom. We found that even a small noise in the compensation coils contributing to the bias field (see Sec. 2.1.4) may result in a larger heating rate and strongly reduce the lifetime.

2.2.4 Evaporative cooling

The evaporative cooling is performed by using energy-selective radiofrequency transitions towards untrapped states. In Fig. 2.8A we sketch the principle of evaporative cooling. Since the atoms are trapped in an inhomogeneous magnetic field, the Zeeman shift will be position-dependent (this is actually the principle of operation of any magnetic trap). Hence, using a radiofrequency field with narrow linewidth, we can excite the transition from the trapped state $|1,-1\rangle$ to the untrapped state $|1,0\rangle$ only in a given region of the trap, the one for which the energy of the RF photon matches the Zeeman shift between the levels. Initially, the velocity distribution of the ensemble is characterized by the classical Maxwellian distribution for a sample in thermal equilibrium at $T = T_0$. The most energetic atoms of the ensemble have higher mean velocities

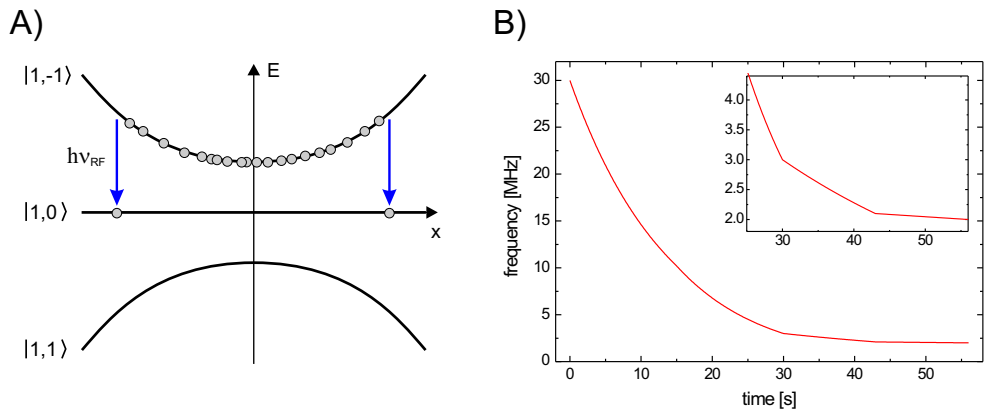

Figure 2.8: A) Principle of RF forced evaporation cooling. A radiofrequency field is used to induce spatially-selective transitions to an untrapped state. The hottest atoms are removed from the trap and the system thermalizes at a lower temperature. B) Evaporative ramp used in the experiment. The inset shows a zoom of the final part of the ramp.

and can reach the outer regions of the parabolic potential. By applying a radiofrequency resonant with the transition for atoms in the external part of the cloud, it is possible to remove the more energetic atoms. The resulting velocity distribution will be an out-of-equilibrium Maxwellian with truncated wings. If now the sample has time to thermalize via atom-atom elastic collisions, the new velocity distribution will be a Maxwellian characterized by a lower temperature $T < T_0$. Decreasing the value of the radiofrequency ν_{RF} it is possible to lower the temperature of the system, at the expense of a loss of atoms. If the initial number of trapped atoms and phase-space density are high enough, the latter increases during the process and at the end of the evaporative ramp it can reach the critical value for Bose-Einstein condensation.

In the ideal case the slower evaporation is the better. However, due to the finite lifetime of the trapped sample, there is an optimal duration of the ramp which allows a good rethermalization without too many losses. The velocity of rethermalization is given by the elastic collisional rate

$$\gamma_{el} \propto n\sigma v, \tag{2.14}$$

where n is the numerical density, $\sigma = 8\pi a^2$ is the elastic cross section (with a the s-wave scattering length) and $v \sim \sqrt{k_B T/m}$ is the mean velocity. During the evaporation v decreases and n increases, but for an efficient cooling the collisional rate γ_{el}, proportional to their product, should not decrease in time. The evaporative ramp used in the experiment (Fig. 2.8B) is faster at the beginning (with exponential dependence $\nu_{RF} \sim A^{-t/\tau}$) and very slow in the last part (with linear dependence $\nu_{RF} \sim A - Bt$): the parameters of the ramp

have been chosen experimentally in order to have the maximum number of condensed atoms at the end of the process.

The radiofrequency is produced with a function generator Stanford Research DS345 computer-controlled via GPIB. The coupling with the atoms is guaranteed by a coil, placed at 2 cm from the cell, producing an oscillating magnetic field that induces magnetic quadrupole transitions. A resonance with the trap coils has been found around 7 MHz, in correspondence of which the voltage at the terminals of the trap coils suddenly increases for a fixed current. In order to avoid this undesired coupling, that causes the power supply for the trap to work in voltage-limited mode and to erogate a smaller current, in proximity of the resonance the RF amplitude is decreased.

2.3 Detection

The condensate is detected with an absorption imaging technique. In this method a beam of resonant light is directed onto the atoms and then is detected by a CCD camera, which takes a picture of the shadow cast by the atoms on the spatial beam profile. This kind of technique, the most commonly used for detecting Bose-Einstein condensates, is quite easy to implement and gives a good signal/noise ratio. However, due to its nature, this detection scheme is destructive, because the absorption of few resonant photons is enough to cause a major heating of the sample and destroy the condensate. For different techniques exploiting the non-absorptive interaction of atoms with off-resonant light and thus allowing for a non-destructive detection, see for example [79].

2.3.1 Imaging system

In the experiment the atoms are illuminated by a resonant beam of light, collimated to a diameter ~ 12 mm much larger than the cloud size, and directed along the radial horizontal $\hat{x}$ axis. The beam is resonant with the closed transition $|F = 2, m_F = 2\rangle \rightarrow |F' = 3, m_{F'} = 3\rangle$: open transitions are not suited for this purpose since the atoms, after a few optical cycles, decay into other levels and cannot absorb again. Since the atoms are in the hyperfine state $F = 1$, we first apply a 50 μs long repumper pulse in order to optically pump them in the $F = 2$ state, then the imaging beam is switched on for 100 μs. The imaging beam is σ^+ polarized and, after a short transient, the atomic population starts to cycle between the levels $|F = 2, m_F = 2\rangle$ and $|F = 3, m_F = 3\rangle$. The absorption of light is described by the Beer-Lambert's law

$$dI = -\sigma n I \, dx, \tag{2.15}$$

where dI is the attenuation of the intensity I in a distance dx, n is the numerical density and $\sigma = 3\lambda^2/2\pi$ is the resonant absorption cross section. Integrated

over the optical path, this equation takes the form

$$I_t = I_0 e^{-\sigma \int n(x)dx}, \tag{2.16}$$

where I_t is the transmitted intensity and I_0 is the incident intensity. From the absorption of the imaging beam one can obtain quantitative information about the column density of the sample, i.e. the density integrated along the direction of propagation of the beam

$$\tilde{n}(y,z) = \int n(x,y,z)dx = -\frac{1}{\sigma} \ln\left(\frac{I_t}{I_0}\right) \tag{2.17}$$

Actually, in the experiment each imaging sequence is obtained processing three different pictures: 1) we first record the transmitted intensity $I_t(x,y)$ of the imaging beam after interaction with the atoms; 2) then we remove the atoms and record the intensity $I_0(x,y)$ of the imaging beam in absence of absorption; 3) we finally record the intensity of the background light $I_d(x,y)$ without the imaging beam and subtract it from the first two pictures in order to compensate for a residual background. The three pictures are taken with the same exposure time 10 ms and are transferred in 600 ms to the computer for the successive analysis. The column density $\tilde{n}(y,z)$ can thus be calculated as

$$\tilde{n}(y,z) = -\frac{1}{\sigma} \ln\left(\frac{I_t - I_d}{I_0 - I_d}\right) \tag{2.18}$$

The beam intensity is $I \simeq 0.6$ mW/cm^2, quite smaller than the saturation intensity $I_s = 1.67$ mW/cm^2 of the cycling transition. Keeping far from saturation is indeed necessary to avoid underestimating the optical density of the sample. The CCD camera used for the detection is a THETA-SYSTEM SIS1-s285 equipped with a CCD sensor Sony ICX285AL. The dimension of the array is 1392 $\times$ 1040 pixels, the size of each pixel 6.45 μm $\times$ 6.45 μm, with a quantum efficiency 40% at 780 nm. The digitalization is made by a 14-bit ADC. In front of the CCD array an interferential filter centered around 780 nm allows only the resonant light to be transmitted, thus suppressing the background signal due to ambient light.

Between the cell and the CCD a simple optical system is used to image the object we want to detect onto the plane of the CCD array. To this aim we use two convergent lenses, the first with $f = 60$ mm placed at $d = 65$ mm from the center of the cell, the second with $f' = 100$ mm placed at $d' = 330$ mm from the first lens. The CCD camera is placed at a distance $d'' = 82$ mm from the second lens in the conjugate plane to the parallel plane passing through the center of the magnetic trap. The magnification factor of this imaging system has been calibrated taking pictures of the atoms released from the trap after different times of flight. The fit of the vertical position with a parabolic function of time (with the gravity acceleration g) allows us

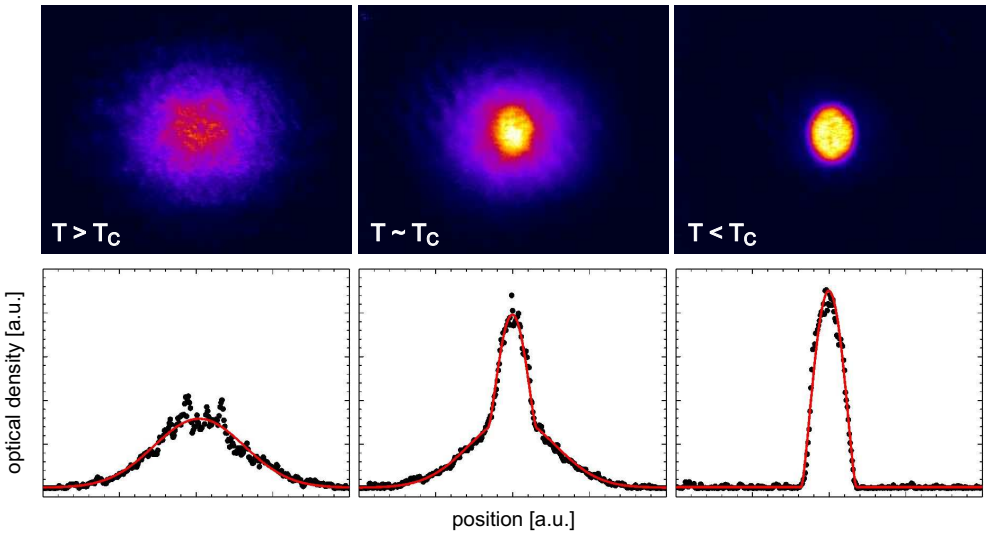

Figure 2.9: BEC transition. Top) Absorption images of an expanded atomic cloud varying the temperature T across the BEC transition at T_C. From left to right, the images show a thermal cloud, a partially condensed cloud and a pure BEC. Bottom) Horizontal cross sections of the density distribution. The lines are fits of the experimental points with a gaussian, a bimodal distribution and an inverted parabola, respectively.

to determine the effective size of the pixels in the plane of the object. The measured magnification factor is 2.22 ± 0.03, with the pixel size corresponding to a linear distance (2.91 ± 0.04) μm in the plane conjugated to the CCD. However, the limiting factor for the imaging resolution is not the finite size of the pixels, but the finite numerical aperture of the optics, which sets a lower limit of the order of 8 μm.

2.3.2 BEC transition

The first and most striking experimental signature of Bose-Einstein condensation [39, 40] in a trapped gas of neutral atoms is the modification of the density distribution crossing the phase transition. Because of the small size and extremely large optical density, the diagnostic of such systems is typically performed after expansion, i.e. imaging the atomic cloud after its release from the trap. When lowering the temperature of the sample below the critical value T_C, a pronounced peak in the expanded density distribution appears. Furthermore, besides this increase in optical density, the distribution itself changes shape. An expanded thermal cloud is well fitted by a gaussian function whose width is related to the momentum distribution and hence to the temperature of the cloud. For a condensate with repulsive interactions, in the

Thomas-Fermi limit of large number of atoms where interactions dominate, the shape of the distribution is strongly modified by the mean-field term and takes the form of an inverted parabola (see Sec. 1.1.2). Moreover, in the case of a BEC confined in a highly elongated trap, the expansion is strongly anisotropic, being faster in the direction where the confinement was stronger. This is the consequence of the Heisenberg uncertainty principle $\Delta p_x \Delta x \sim \hbar$ holding for the wavefunction of a Bose-Einstein condensate: the tighter the confinement in the $\hat{x}$ direction, the bigger the momentum spread Δp_x and the faster the condensate expands in that direction. On the contrary, for long expansion times the density distribution of a thermal cloud is spherically symmetric and no evidence of the trap anisotropy can be found. In the upper row of Fig. 2.9 we show three absorption images of the expanded atomic cloud crossing the critical temperature for Bose-Einstein condensation.

Here we report the expression for the density, the column density and the total number of atoms in the case of an axially-symmetric Gaussian and Thomas-Fermi distribution:

Gaussian distribution:

$$n(x,y,z) = n_0 \exp\left(-\frac{x^2+y^2}{2\sigma_\perp^2} - \frac{z^2}{2\sigma_z^2}\right) \tag{2.19}$$

$$\tilde{n}(y,z) = (2\pi)^{1/2}\sigma_\perp n_0 \exp\left(-\frac{x^2}{2\sigma_\perp^2} - \frac{z^2}{2\sigma_z^2}\right) \tag{2.20}$$

$$N = (2\pi)^{3/2}\sigma_\perp^2 \sigma_z n_0 \tag{2.21}$$

Thomas-Fermi distribution:

$$n(x,y,z) = n_0 \left(1 - \frac{x^2+y^2}{R_\perp^2} - \frac{z^2}{R_z^2}\right) \theta\left(1 - \frac{x^2+y^2}{R_\perp^2} - \frac{z^2}{R_z^2}\right) \tag{2.22}$$

$$\tilde{n}(y,z) = \frac{4}{3} R_\perp n_0 \left(1 - \frac{y^2}{R_\perp^2} - \frac{z^2}{R_z^2}\right)^{3/2} \theta\left(1 - \frac{y^2}{R_\perp^2} - \frac{z^2}{R_z^2}\right) \tag{2.23}$$

$$N = \frac{8\pi}{15} R_\perp^2 R_z n_0 \tag{2.24}$$

In the lower row of Fig. 2.9 we show a horizontal cross section of the above images together with a least-squares fit of the 2D column density with three different functions, from left to right: a gaussian, a bimodal gaussian + Thomas-Fermi, a pure Thomas-Fermi. The 2D fit is made by a program written in C and linked with the FORTRAN package MINUIT from the CERN

libraries [80]. The main program evaluates the χ^2 of the measured density distribution $f(y,z)$ with respect to a function $\tilde{n}(y,z;\alpha)$ (gaussian, Thomas-Fermi, bimodal, ...) dependent on the set of parameters $\vec{\alpha}$

$$\chi^2 = \sum_{y,z} [f(y,z) - \tilde{n}(y,z;\vec{\alpha})]^2 \tag{2.25}$$

and passes this function to the MINUIT routine, which finds its minimum in the space of the fit parameters. According to the maximum likelihood criterion, the function χ^2 has a local minimum in correspondence of the most probable set of parameters governing the measured distribution. The numerical algorithm used by MINUIT to find the minimum of χ^2 is a modified version of the Davidon-Fletcher-Powell method [81].

Chapter 3

Collective dynamics of a BEC in an optical lattice

In this chapter we describe the results of two experiments devoted to the investigation of the collective dynamics of a Bose-Einstein condensate in a periodic potential. Collective excitations have been extensively studied in the presence of a harmonic trapping potential [15, 16, 82] and have first contributed to the demonstration of BEC superfluidity. An interesting question, related to the problem of quantum transport in periodic structures, is whether the addition of a lattice potential modifies the collective dynamics and if it can affect the BEC superfluidity.

In Sec. 3.1 we will discuss how it is possible to create periodic potentials with laser light. A standing wave configuration is used to produce a 1D *optical lattice*, whose height can be easily controlled by an accurate choice of the laser parameters. We will introduce some useful notations and we will describe how the optical lattice is produced and calibrated.

In a first experiment [29], described in Sec. 3.2, we have studied the collective excitations of a BEC trapped in a harmonic + periodic potential. The frequencies of the dipole and quadrupole modes exhibit a strong dependence on the lattice height, that can be explained in terms of a modified *effective mass* introduced by the lattice. We demonstrate that the frequencies of these two modes still scale in the same way as the height of the lattice is changed, a clear indication of superfluid behavior.

In a second experiment [30], described in Sec. 3.3, we have studied large amplitude dipole oscillations of the BEC in the harmonic + periodic potential. Increasing the initial displacement of the condensate from the trap center we observe the disruption of coherent oscillations and the onset of an *insulating* regime. The experimental findings, interpreted in terms of a *dynamical instability* induced by the interplay between periodicity and (repulsive) nonlinearity, are compared with a 1D analytical model [83] and with the solution of the 3D Gross-Pitaevskii equation [84].

3.1 The optical lattice

3.1.1 Dipole forces

Light is a powerful tool for the manipulation of the motional degrees of freedom of neutral atoms. Transfer of momentum in the interaction between atoms and light is at the heart of the laser cooling and trapping techniques developed in the last thirty years and acknowledged by the award of the Nobel Prize in Physics to S. Chu, C. Cohen-Tannoudji and W. Phillips in 1997. There are essentially two kinds of radiative forces, associated with the absorptive and the dispersive properties of the interaction [85]:

1. There is a dissipative force, also called *radiation pressure force*, associated with the transfer of momentum from light to atoms in a resonant scattering process. The atoms, absorbing photons from an incident light beam, are pumped into an excited state, then they spontaneously decay back into the ground state, emitting photons in random directions. This dissipative force, characterized by a net momentum transfer $\hbar\mathbf{k}$ for each absorption/emission cycle, with $\mathbf{k}$ the wavevector of the laser light, is at the basis of the most common laser cooling techniques.

2. There is a conservative force, also called *dipole force*, arising from the dispersive off-resonant interaction between light and atoms and proportional to the intensity gradient of the field. In this process there is no excitation of atoms to higher energy states and mechanical effects are caused by a redistribution of the photons among the elementary plane waves in which the radiation field can be expanded. Exploiting this effect, several different beam configurations can be used to create conservative optical traps with different geometries.

A complete theoretical analysis of these effects, founded on an elegant and rigorous quantum-mechanical treatment, can be found in [85]. We will instead follow the semiclassical approach of [86], that gives some useful expressions for the dissipative and reactive component of the radiation force. We consider a simple model in which the atom, treated as a two-level system, is subject to a classical radiation field oscillating at frequency ω:

$$\mathbf{E}(\mathbf{r},t) = \hat{e}E(\mathbf{r})e^{-i\omega t} + h.c. \tag{3.1}$$

This field induces an atomic dipole moment

$$\mathbf{p}(\mathbf{r},t) = \hat{e}p(\mathbf{r})e^{-i\omega t} + h.c. \tag{3.2}$$

oscillating at the same frequency of the driving field and proportional to the latter through the *complex polarizability* α:

$$p(\mathbf{r}) = \alpha E(\mathbf{r}). \tag{3.3}$$

This relation holds only in the linear regime, when saturation effects can be neglected and the atomic population is almost entirely in the ground state. The real part of α, describing the component of $\mathbf{p}$ oscillating in phase with $\mathbf{E}$, is responsible for the dispersive properties of the interaction, while the imaginary part, describing the out-of-phase component of $\mathbf{p}$, is connected with the absorptive properties. Both these components strongly depend on ω as the frequency of the laser is scanned across the atomic resonance ω_0.

We define the *dipole potential* as the interaction energy of the induced dipole $\mathbf{p}$ interacting with the driving electric field $\mathbf{E}$

$$U_{dip}(\mathbf{r}) = -\frac{1}{2}\langle \mathbf{p} \cdot \mathbf{E} \rangle = -\frac{1}{2\epsilon_0 c}\mathrm{Re}(\alpha) I(\mathbf{r}), \tag{3.4}$$

where the angle brackets indicate the time average over the optical oscillations and $I(\mathbf{r})$ is the average field intensity. By differentiating Eq. (3.4) one can calculate the *dipole force* exerted on the atom:

$$F_{dip}(\mathbf{r}) = -\nabla U_{dip}(\mathbf{r}) = \frac{1}{2\epsilon_0 c}\mathrm{Re}(\alpha)\nabla I(\mathbf{r}). \tag{3.5}$$

This force is proportional to the intensity gradient ∇I, so it vanishes when the field intensity is uniform, as in a plane wave. By engineering the geometry of the light beams it is possible to create almost any kind of potential and to change their depth tuning the laser parameters.

We also derive an expression for the dissipative effects related to the imaginary part of α, which describes the absorption of photons from the incident light beam. The average energy absorbed by the atom in the unit of time, divided by the photon energy $\hbar\omega$, gives the average number of photons which are scattered in the unit of time through cycles of absorption and subsequent spontaneous emission

$$\Gamma_{sc}(\mathbf{r}) = \frac{\langle \dot{\mathbf{p}} \cdot \mathbf{E} \rangle}{\hbar\omega} = \frac{1}{\hbar\epsilon_0 c}\mathrm{Im}(\alpha) I(\mathbf{r}), \tag{3.6}$$

Eqs. (3.4) and (3.6) are the fundamental equations describing the mechanical effects of the interaction between atoms and coherent light. Solving the optical Bloch equations for a two-level system, one can easily derive an analytical expression for the atomic polarizability $\alpha(\omega)$. In the far-off resonant regime, in which the detuning $\Delta = \omega - \omega_0$ from the atomic resonance ω_0 is much larger than the radiative linewidth of the excited state Γ and of the Rabi frequency Ω, Eqs. (3.4) and (3.6) become [86]

$$U_{dip} = \frac{3\pi c^2}{2\omega_0^3}\left(\frac{\Gamma}{\Delta}\right) I \tag{3.7}$$

$$\Gamma_{sc} = \frac{3\pi c^2}{2\hbar\omega_0^3}\left(\frac{\Gamma}{\Delta}\right)^2 I \tag{3.8}$$

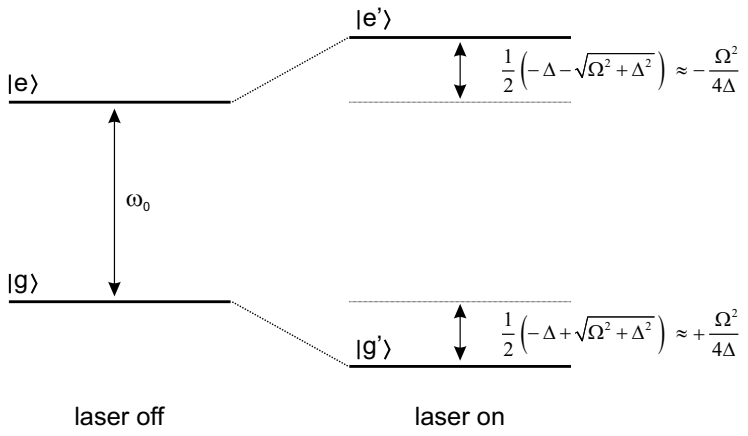

Figure 3.1: Light shift in a two-level system.

From Eq. (3.7) we note that the sign of the dipole potential depends on the sign of the detuning. More precisely, if the light is red-detuned ($\Delta < 0$) the dipole potential is negative, and hence the maxima of intensity correspond to minima of the potential: as a consequence, the atoms tend to localize in regions of high field intensity. On the contrary, if the light is blue-detuned ($\Delta > 0$) the dipole potential is positive, hence maxima of intensity correspond to maxima of the potential and the atoms tend to localize in regions of low field intensity. From Eqs. (3.7) and (3.8) we also note that the dependence on the detuning is different in the two cases: while the dipole potential U_{dip} scales as $1/\Delta$, the scattering rate Γ_{sc} scales as $1/\Delta^2$. As a consequence, moving further out of resonance, the contribution of the dipole force will be more dominated by the dissipative processes, that may cause a heating of the atomic sample. In other words, for a fixed height of the dipole potential, the spontaneous scattering of photons can be suppressed increasing Δ while increasing I in order to keep the ratio I/Δ constant.

This simple model is not the only possible approach to the derivation of the dipole force. Following a more quantum-mechanical treatment, the dipole force can be obtained from the energy shift introduced by the optical field to the atomic levels [87]. Let us consider a two-level system with a ground state $|g\rangle$ and an excited state $|e\rangle$ with energies $\hbar\omega_g$ and $\hbar\omega_e$ respectively. In the presence of coupling with the radiation field, which introduces off-diagonal terms in the Hamiltonian, these two states cease to be eigenstates of the system. After diagonalizing the total Hamiltonian including the interaction term, we find new eigenstates $|g'\rangle$ and $|e'\rangle$, that can be written as mixtures of the initial states $|g\rangle$ and $|e\rangle$. The new eigenstates have energies $\hbar\omega_g + \hbar(-\Delta + \sqrt{\Omega^2 + \Delta^2})/2$ and $\hbar\omega_e + \hbar(-\Delta - \sqrt{\Omega^2 + \Delta^2})/2$ respectively, as shown in Fig. 3.1. The energy shift in the atomic states introduced by the coupling with the radiation field

is called *light shift*, or *ac Stark shift*. In the far detuned regime, when $\Delta \gg \Omega$, the two states $|g'\rangle$ and $|e'\rangle$ are almost identical to the initial states $|g\rangle$ and $|e\rangle$ and the energy shifts reduce to $+\hbar\Omega^2/4\Delta$ and $-\hbar\Omega^2/4\Delta$. Let us now assume that the field intensity $I \propto \Omega^2$ is a function of the position. Since the light shift is proportional to the intensity, also the energy of the ground state turns out to be a function of the position. The dipole potential can thus be defined as the spatially dependent light shift of the ground state

$$U_{dip} = \frac{\hbar\Omega^2}{4\Delta} = \frac{\mu^2 E^2}{4\hbar\Delta} \tag{3.9}$$

By using the definition of the atomic dipole moment $\mu = (3\pi\epsilon_0\hbar c^3\Gamma/\omega_0^3)^{1/2}$ and of the average field intensity $I = \epsilon_0 c E^2/2$ it is easy to demonstrate that this definition reduces to the one given in Eq. (3.7).

3.1.2 Optical lattices

It is clear that, using the dipole interaction (3.7) with the proper choice of the laser setup, it is possible to create almost any kind of potential geometry. If we want to create a periodic potential, the simplest configuration is a standing wave, obtained through the interference of two counterpropagating beams. Such a configuration takes the name of *optical lattice*. Let us consider two plane waves with the same frequency ω travelling in opposite directions along $\hat{z}$ and linearly polarized along the same axis $\hat{e}$:

$$\mathbf{E_1}(z,t) = \hat{e}E_1\cos(kz + \omega t + \delta) \tag{3.10}$$

$$\mathbf{E_2}(z,t) = \hat{e}E_2\cos(kz - \omega t - \delta), \tag{3.11}$$

where $k = \omega/c$ and δ accounts for an arbitrary relative phase. The instantaneous intensity will be given by the square modulus of the total field:

$$I(z,t) = \epsilon_0 c|\mathbf{E_1}(z,t) + \mathbf{E_2}(z,t)|^2. \tag{3.12}$$

Using some mathematics and averaging over the terms oscillating at the optical frequency ω, we obtain the following expression for the average intensity

$$I(z) = \frac{1}{2}\epsilon_0 c\left[(E_1 - E_2)^2 + 4E_1E_2\cos^2(kz)\right], \tag{3.13}$$

that in the particular case $E_1 = E_2 = E_0$ reduces to

$$I(z) = I_0\cos^2(kz), \tag{3.14}$$

where $I_0 = 2\epsilon_0 c E_0^2$ is the peak intensity. Using Eq. (3.7), the dipole potential experienced by the atoms in this standing wave laser field is

$$U_{dip}(z) = \frac{3\pi c^2}{2\omega_0^3}\left(\frac{\Gamma}{\Delta}\right) I_0\cos^2(kz), \tag{3.15}$$

that in the following will be indicated with the notation

$$V(z) = V_0 \cos^2(kz). \tag{3.16}$$

This is a perfect 1D periodic potential with spacing $\lambda/2$ and a harmonic content limited to only one spatial frequency component k. In the following section we will describe how this potential is produced and we will give some useful definitions and scales.

3.1.3 Experimental setup

The light for the optical lattice comes from a commercial Ti:Sa ring laser (Coherent 899) pumped by a high power solid state laser (Spectra-Physics Millennia). The laser wavelength can be tuned from 750 to 830 nm by acting on the intracavity birefringent filters, which, together with an etalon, allow for the selection of a single lasing mode. The maximum power at the center of the gain curve of the active medium is 800 mW. The beam coming from the Ti:Sa laser passes through an acousto-optic modulator used for fast switching on and off (commutation time ~ 10 μs) and a mechanical shutter for ensuring a complete extinction of the light when the lattice is switched off (commutation time ~ 1 ms). The quasi-collimated beam is aligned along the weak axis $\hat{z}$ of the magnetic trap and, after passing through the vacuum cell, is retroreflected by a mirror to produce the standing wave configuration (as sketched in Fig. 3.2). The transverse size of the beam in the center of the trap is ~ 300 μm, large enough to allow us to completely neglect the variation of intensity across the radial width of the condensate.

In the direction of the optical lattice the Thomas-Fermi radius of the condensate is $R_z \simeq 70$ μm. For $\lambda = 800$ nm the lattice spacing is $d = 400$ nm, hence the condensate occupies ≈ 350 sites. If we consider the characteristic length scale of the lattice, the condensate wavefunction can be treated with good approximation as a plane wave, since its extension is much larger than the lattice spacing. This consideration, together with the fact that the BEC ground state is Heisenberg-limited, has an important consequence on the condensate momentum distribution. Following [88, 89], the effective rms width of the momentum distribution Δp_z in the Thomas-Fermi limit is connected to the condensate size by $\Delta p_z \simeq 1.58\hbar/R_z$. From this expression we obtain that

$$\frac{\Delta p_z}{\hbar k} = \frac{\lambda}{2\pi\hbar}\frac{1.62\hbar}{R_z} = \frac{1.62}{\pi}\frac{d}{R_z} \approx 0.003\,, \tag{3.17}$$

where we have used $k = 2\pi/\lambda$. The condensate wavefunction can thus be considered as a δ-like distribution in momentum space with respect to the width of the Brillouin zones $2\hbar k$. For comparison, the momentum spread of a thermal sample at the critical temperature for condensation $T_C \simeq 100$ nK is

$$\frac{\Delta p_z}{\hbar k} = \frac{\sqrt{m k_B T_C}}{\hbar k} \approx 0.55\,, \tag{3.18}$$

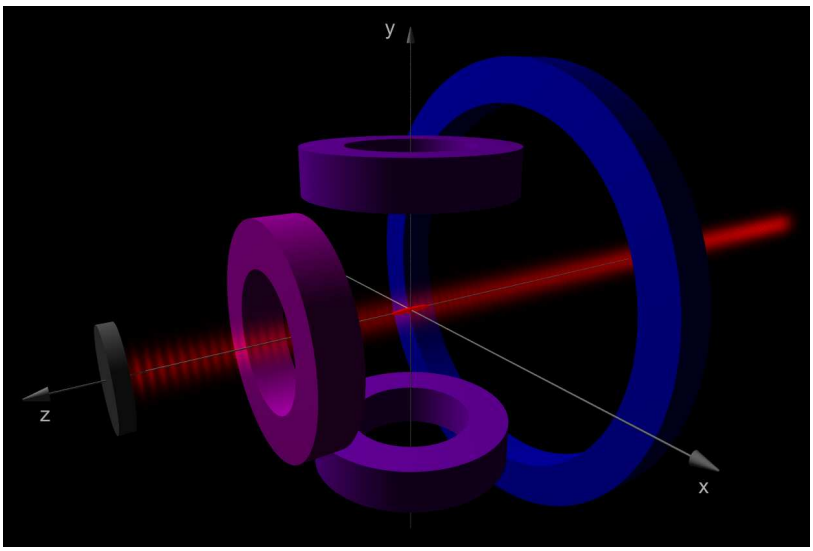

Figure 3.2: Lattice geometry. The collimated lattice beam is aligned along the trap axis and is retroreflected by a mirror (beam size and lattice spacing are not in scale with the magnetic trap coils).

almost 200 times bigger than the width of the condensate.

The following table shows some important quantities regarding the interaction of an ^{87}Rb atom with an optical lattice at $\lambda = 800$ nm:

Lattice spacing	$d = \dfrac{\lambda}{2} = 400$ nm
Recoil energy	$E_R = \dfrac{\hbar^2 k^2}{2m} = h \times 3.59$ kHz
Bragg velocity	$v_B = \dfrac{\hbar k}{m} = 5.74$ mm/s

The recoil energy E_R is the kinetic energy gained by an atom initially at rest after absorbing one lattice photon. The Bragg velocity v_B is the recoil velocity acquired by the atom in the same absorption process. This two quantities, together with the laser wavenumber k, completely set the scales of Figs. 1.4 and 1.6 showing the peculiar features of the band structure. In the following sections the height of the periodic potential will be expressed in units of recoil energy with the dimensionless parameter s defined as

$$s = \frac{V_0}{E_R} \tag{3.19}$$

The finite coherence length of the Ti:Sa laser producing the optical lattice has practically no effect on the stability of the periodic potential. In principle, the position of the standing wave nodes and antinodes is determined by both the laser wavelength and the position of the mirror retroreflecting the lattice beam. The frequency jitter of the laser $\Delta\nu \simeq 1$ MHz corresponds to a fluctuation $\Delta\lambda/\lambda \simeq 3 \times 10^{-9}$ on the laser wavelength. If the mirror is placed at $l = 20$ cm from the position of the condensate, considering that this distance corresponds to $n = l/\lambda = 2.5 \times 10^5$ laser wavelengths, the phase slip accumulated on the round-trip distance $2l$ due to the laser frequency jitter is $\Delta\phi/2\pi = 2n\Delta\lambda/\lambda \simeq 1.5 \times 10^{-3}$, that means a fluctuation in the nodes and antinodes position of $\lambda\Delta\phi/2\pi \simeq 1$ nm. We expect that this effect is much smaller than the one produced by mechanical noise on the mounting of the mirror retroreflecting the lattice beam, which is the limiting factor for the stability of the periodic potential (see also the discussion in Sec. 4.1.2).

3.1.4 Lattice calibration

In principle the height of the optical lattice can be calculated using Eq. (3.15), provided that the laser parameters I_0 and Δ are known. However, this method can be affected by systematic errors concerning the measurement of the real intensity I_0 experienced by the atoms. As a matter of fact, besides the possibility of instrumental calibration errors, small misalignments of the lattice beams or not completely parallel polarizations can result in a different intensity from the one calculated. For these reasons, it is important to have a method for calibrating *in situ* the height of the optical lattice. In order to accomplish this task we use *Bragg scattering* [3, 88].

Let us assume that the condensate is initially moving along $\hat{z}$, with a momentum $-\hbar k$ in the laboratory frame. At time $t = 0$ we suddenly switch on the optical lattice we want to calibrate. The two lattice beams can induce Raman transitions between the momentum states $-\hbar k$ and $+\hbar k$ in a two-photon process that conserves both energy and momentum. This mechanism is schematically shown in Fig. 3.3. The two black curves show the total energy of the atoms (internal + kinetic) as a function of the atomic momentum for both the ground and the excited state. The double arrow represents the two-photon transition, in which a photon is absorbed from one lattice beam (exciting the system to a virtual state) and then re-emitted in the counterpropagating beam. The initial momentum state $-\hbar k$ has been chosen in order to satisfy the resonance condition: the two photons have the same energy and the initial and final atomic states have the same energy too. If the initial momentum is different from $\pm\hbar k$ and the two counterpropagating photons have the same frequency, energy is not conserved and the probability of the process is smaller. As a result of this excitation, the atomic population starts to oscillate between the momentum states coupled by the lattice beams. The population in the

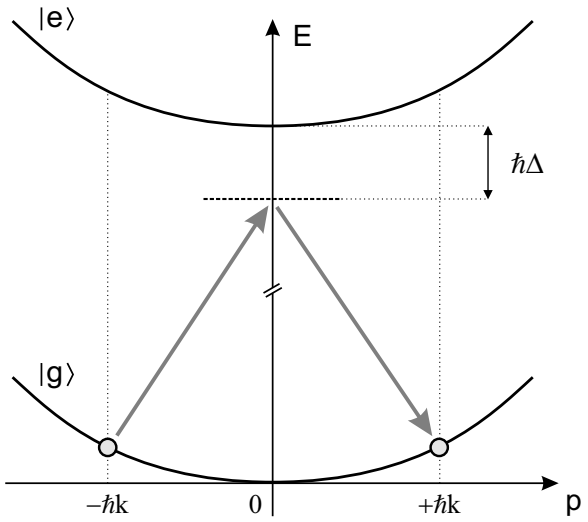

Figure 3.3: Schematics of Bragg transitions. An atom is illuminated by two counterpropagating off-resonant laser beams. If the initial momentum of the atom is $-\hbar\mathbf{k}$ (with $\mathbf{k}$ laser wavevector), a two-photon transition to the momentum state $+\hbar\mathbf{k}$ is possible by absorption of one photon from one lattice beam and stimulated emission into the other beam. In this Raman process energy is conserved and the net momentum transfer is $2\hbar\mathbf{k}$.

momentum state $+\hbar k$ is

$$N_{+\hbar k} = \frac{N}{2}\left[1 - \cos\left(\Omega_B t\right)\right], \tag{3.20}$$

the effective Rabi frequency Ω_B of the two-photon excitation being

$$\Omega_B = \frac{\Omega_0^2}{2\Delta}, \tag{3.21}$$

where Δ is the detuning from the excited state and $\Omega_0 = \mu E_0/\hbar$ is the Rabi frequency associated to the single beam excitation, with μ the atomic dipole moment and E_0 the field amplitude of the single beam. In the far detuned regime ($\Delta \gg \Gamma, \Omega_0$) single photon transitions to the excited state can be neglected and this two-photon excitation is the dominant process.

The Rabi frequency (3.21) of the Bragg transition, which can be precisely measured, is used to calibrate the height of the optical lattice. In the antinodes of the standing wave, where the two lattice beams constructively interfere, the field amplitude is $2E_0$, hence the local single-photon Rabi frequency Ω that appears in the dipole potential (3.9) is twice the single beam Rabi frequency Ω_0. Substituting $\Omega = 2\Omega_0$ in Eq. (3.9) evaluated in the antinodes of the

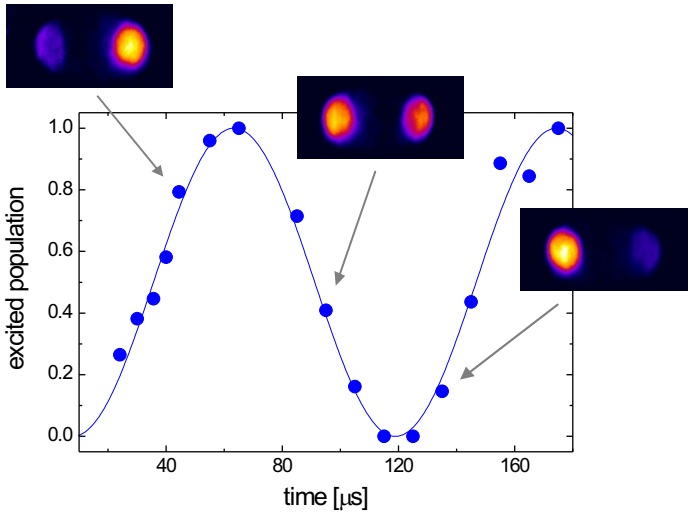

Figure 3.4: Rabi oscillations induced by Bragg scattering. The points show the population of the excited state $+\hbar k$ as a function of the pulse length Δt. The left peak in the images refers to the momentum state $-\hbar k$, the right peak to the momentum state $+\hbar k$. From the fitted Rabi frequency Ω_B we calculate the lattice height s through Eq. (3.23).

standing wave and using Eq. (3.21), we obtain a relation connecting the lattice height to the Rabi frequency of the Bragg transitions:

$$V_0 = U_{dip}^{max} = \frac{\hbar\Omega^2}{4\Delta} = \frac{\hbar\Omega_0^2}{\Delta} = 2\hbar\Omega_B, \tag{3.22}$$

hence the height of the optical lattice in units of recoil energy $E_R = \hbar\omega_R$ is

$$s = \frac{2\Omega_B}{\omega_R}. \tag{3.23}$$

The experimental procedure for the lattice calibration is the following. By slightly changing the current configuration in the trap coils, we displace the center of the magnetic trap along the axis direction in order to induce a center-of-mass oscillation of the condensate in the magnetic trap[1]. When the velocity of the condensate is $-v_B = -\hbar k/m$, the trap is suddenly switched off and the condensate starts to expand with a constant horizontal velocity $-v_B$. After 2 ms of expansion[2] we switch on the lattice beams for a time Δt, then we let the atomic cloud expand for a time long enough for the momentum components

[1] The procedure for the excitation of collective modes in the trapped condensate will be more carefully described in Sec. 3.2.2.

[2] At this time the atoms have moved only 20 μm in the vertical direction, but the density has become small enough to avoid mean-field effects that could complicate the analysis [90].

$-\hbar k$ and $+\hbar k$ to spatially separate. After a total expansion time $t_{exp} = 28$ ms we take an absorption image of the atoms and measure the population of the two momentum states. In Fig. 3.4 we plot the population fraction in the state $+\hbar k$ as a function of Δt. From the fit of the experimental data with a sine function we extract the Rabi frequency of the oscillation and, through Eq. (3.23), the height of the optical lattice.

This calibration technique is valid in the limit of low lattice heights, when only two momentum components are present. For higher field intensities the two-level approximation fails: more than one momentum states start to be populated and the theoretical analysis gets more complicated.

3.2 Collective excitations of a BEC in the lattice

3.2.1 Introduction

The study of collective excitations represents an invaluable tool for investigating the quantum macroscopic behavior of many-body systems. Collective excitations of a harmonically trapped BEC of neutral atoms were first studied in [15] and [16] and constituted a first stringent test of the mean field theory for a condensed gas of weakly interacting bosons. These results share with the detection of quantized vortexes [11, 12] and with the observation of a reduced moment of inertia (with respect to the classical rigid value) [13, 14] the importance of being one of the most striking evidences of the superfluidity of these systems. In this section we describe the experimental investigation of the low-lying collective modes in a harmonically trapped BEC in the presence of a 1D optical lattice [29]. Although the periodic potential deeply modifies the transport properties of the BEC in the harmonic trap, we show that the frequency of the collective modes can be obtained from the pure harmonic case with a simple *effective mass* renormalization.

Collective excitations in a harmonic potential. Let us first consider the theory of collective excitations for a BEC trapped in a pure harmonic potential, as developed in [82]. In this work it is shown that in the regime of validity of the Thomas-Fermi approximation $Na/a_{ho} \gg 1$, the GPE can be conveniently recast in the form of hydrodynamic equations for the atomic density $\rho(\mathbf{r}, t)$ and the velocity field $\mathbf{v}(\mathbf{r}, t)$:

$$\frac{\partial \rho}{\partial t} + \nabla (\mathbf{v}\rho) = 0 \tag{3.24}$$

$$m\frac{\partial \mathbf{v}}{\partial t} + \nabla \left(\delta\mu + \frac{1}{2} m\mathbf{v}^2 \right) = 0, \tag{3.25}$$

where $\delta\mu$, dependent on the external potential and the interaction term, is the variation of the chemical potential with respect to its ground state value μ.

These equations, formally equivalent to the GPE, have the general structure of the equations describing the dynamics of superfluids at zero temperature. The frequencies of the collective modes can be calculated perturbing the ground state density

$$\rho_0(\mathbf{r}) = \frac{m}{4\pi\hbar^2 a}\left[\mu - V_{ext}(\mathbf{r})\right] \tag{3.26}$$

with small deviations $\delta\rho$ of given geometry and calculating the energy corresponding to these excitations. In the case of spherical symmetry, writing the perturbation $\delta\rho$ in the form of spherical harmonics, one can label the modes with the quantum numbers (n, l, m) indicating, respectively, the number of radial nodes, the total angular momentum of the excitation and its component along the symmetry axis. Though these quantum numbers correctly identify the excitation modes in a spherical trap, in the case of axially symmetric traps m is still a good quantum number.

We specialize the discussion to the case of a cigar-shaped geometry, where the axial trapping frequency ω_z is much smaller than the radial trapping frequencies $\omega_x = \omega_y = \omega_\perp$. The lowest energy excitation mode is the *axial dipole mode* (0,1,0), that corresponds to a rigid center-of-mass oscillation along the trap axis with frequency

$$\omega_D = \omega_z \tag{3.27}$$

equal to the axial trap frequency. The lowest energy shape oscillations with $m = 0$ are obtained from the mixing of the quadrupole mode $(0, 2, 0)$ and the monopole mode $(1, 0, 0)$. The dispersion law of the decoupled modes is

$$\omega^2 = \omega_\perp^2\left(2 + \frac{3}{2}\lambda^2 \mp \frac{1}{2}\sqrt{9\lambda^4 - 16\lambda^2 + 16}\right), \tag{3.28}$$

where $\lambda = \omega_\perp/\omega_z$ is the aspect ratio of the trap. The mode at lower frequency (minus sign) is characterized by an oscillation of the axial and radial widths at the same frequency but with opposite phase. The mode at higher frequency (plus sign) is characterized by an oscillation of the axial and radial widths at the same frequency and with the same phase. For a highly elongated cigar-shaped geometry ($\lambda \ll 1$), these two modes have quite different frequencies

$$\omega_Q = \sqrt{\frac{5}{2}}\omega_z \tag{3.29}$$

$$\omega_T = 2\omega_\perp \tag{3.30}$$

and the axial and radial oscillations are almost decoupled[3]. While the mode at frequency (3.29), usually called *quadrupole mode* (or *axial breathing mode*), is mostly characterized by an oscillation of the axial width, the mode at frequency (3.30), usually called *transverse breathing mode*, is mostly characterized by an

[3]The first correction term to the frequencies (3.29) and (3.30) due to the finite aspect ratio of the trapping potential is of order $\lambda^2/8 \simeq 10^{-3}$ for our trap geometry with $\lambda \simeq 0.1$.

oscillation of the radial width. The frequencies of these collective modes in the Thomas-Fermi limit of large number of atoms have been first verified with excellent accuracy in [16].

Collective excitations in a harmonic + 1D periodic potential. Let us now consider the case of collective excitations of a harmonically trapped BEC in the presence of a 1D optical lattice. The authors of [91] solved the problem using a tight binding approximation in which the condensate wavefunction is written as the sum of many functions localized at the lattice sites (see Sec. 1.2.4). If one assumes that the quantum tunnelling between adjacent optical wells is sufficient to ensure long-range coherence across the entire array, the order parameter of the system can still be described by the Gross-Pitaevskii theory. Using the same approach as [82], even in the presence of the periodic potential the equation describing the system can be mapped into hydrodynamic equations similar to Eqs. (3.24) and (3.25) [91, 92]. The presence of the periodic potential has two main effects:

- The tighter axial confinement produced by the lattice wells results in a local compression of the gas, hence in an increased strength of the interactions. This effect can be described with a renormalized interaction constant $\tilde{g}$, which is generally larger than g.
- The energy as a function of the quasimomentum (along the lattice axis) does not have the free-particle quadratic form (as discussed introducing the Bloch theory in Sec. 1.2.1). Actually, for small velocities (or, equivalently, small phase gradients across the lattice), this term can still be expressed by a quadratic form where the real mass m is replaced by an effective mass m^* dependent on the tunnelling rate K (see Sec. 1.2.4):

$$m^* = m\frac{E_R}{\pi^2 K}, \tag{3.31}$$

This derivation also shows that the *effective* potential probed by the condensate is still harmonic with an effective axial frequency $\omega_z^* = \sqrt{m/m^*}\omega_z$ renormalized by the effective mass. In particular, this means that the above expressions (3.27), (3.29) and (3.30) for the frequencies of the collective modes in a parabolic potential still hold in the presence of the optical lattice, provided that the trap frequency ω_z along the direction of the lattice is substituted with the renormalized frequency $\sqrt{m/m^*}\omega_z$:

$$\omega_D = \sqrt{\frac{m}{m^*}}\omega_z \tag{3.32}$$

$$\omega_Q = \sqrt{\frac{5}{2}}\sqrt{\frac{m}{m^*}}\omega_z \tag{3.33}$$

$$\omega_T = 2\omega_\perp \tag{3.34}$$

The frequencies of the dipole and the quadrupole modes, being proportional to the axial trap frequency, are thus rescaled by the effective mass. The transverse breathing mode, instead, being proportional to the radial trap frequency, is expected to be unaffected by the optical lattice. We note that the frequencies of these collective modes, as well as the frequencies in the pure harmonic case, do not explicitly depend on the coupling constant g (or $\tilde{g}$), hence on the strength of the interactions. However, the presence of the factor $\sqrt{5/2}$ in the quadrupole frequency ω_Q is a nontrivial consequence of the mean-field term and is peculiar of the superfluid nature of the system[4].

3.2.2 The experiment

In the experiment, we produce the BEC in the ground state of the combined harmonic + periodic potential. In order to do this, we perform the evaporative cooling in the magnetic trap until the sample has reached a temperature $T \gtrsim T_C$. Then the optical lattice is switched on and the evaporative cooling is completed in the harmonic + periodic potential until $T \ll T_C$, when the atomic sample is almost entirely condensed. In this experiment the Ti:Sa laser is tuned at a wavelength $\lambda = 757$ nm and the maximum achievable lattice height is $s \simeq 5$. The radial size of the lattice beam $w \sim 300$ μm is much larger than the radial size of the condensate, so that we can neglect the effect of the optical potential on the radial dynamics. In this configuration the photon scattering rate (3.8) is smaller than 0.04 s^{-1} and can be completely ignored on the timescale of the experiment.

In the tight binding regime, when the lattice height is much higher than the chemical potential ($sE_R \gg \mu$), the system realizes an array of condensates localized at the lattice sites and behaving as a linear chain of Josephson junctions, as introduced in Sec. 1.2.4 and experimentally demonstrated in [20]. If the harmonic + periodic potential is suddenly switched off the condensates located at the individual lattice sites start to expand and overlap. The density distribution after expansion from this potential shows well resolved interference peaks [19] at momenta $+2\hbar k$ and $-2\hbar k$. The presence of such interference peaks is an indication of the long-range phase coherence of the sample. When the phase coherence is absent or strongly reduced, one should expect to see a reduction of the contrast in the interferogram. Even if an array of independent condensates still produces resolved interference fringes [35], in average their visibility (which depends on the particular realization of the experiment) decreases in the case of incoherent sources.

Once we have produced the condensate in the ground state of the harmonic + periodic potential, we excite dipole and quadrupole oscillations. The excitation procedure is different for the different modes:

[4] Indeed, for a noninteracting thermal sample in a pure harmonic potential the quadrupole mode frequency is $2\omega_z$, while for a strongly interacting non-condensed gas in the hydrodynamic limit the quadrupole mode frequency is $\sqrt{12/5}\omega_z$.

Dipole mode. The dipole mode along the z direction is excited by non-adiabatically displacing the center of the magnetic trap. In our trap geometry this task can be accomplished quite easily by slightly changing the configuration of the currents flowing in the trap coils. According to Eqs. (2.9) and (2.10), the center of the trap is located in $z_0 = (b_1' - b_1)/2b_2$, which is zero when the same current I flows in all the trap coils and the gradient of the quadrupole field b_1' exactly cancels the gradient of the curvature field b_1. In order to displace the trap center we change the current flowing in the curvature + antibias coils from I to $I(1-\epsilon)$, thus changing the curvature gradient in the center from $b_1 = b_1'$ to $b_1'(1-\epsilon)$. After this change the center of the trap is displaced in the direction opposite to the curvature coil by

$$\Delta z_0 = \frac{b_1'}{2b_2}\epsilon \approx \epsilon \times 10\text{mm}, \tag{3.35}$$

with the trap frequencies almost unaffected.

Experimentally, we suddenly change the voltage V_Q applied to the gate of the MOSFETs controlling the current in the curvature and antibias coils (see Fig. 2.7). These MOSFETs, which are completely closed in the magnetic trap phase, deviate a small fraction of the current flowing in the quadrupole coils, thus letting a lower current flow in the curvature coil. The trap displacements used in the experiment are typically of the order of $\Delta z_0 = 15\mu$m, corresponding to $\epsilon = 1.5 \times 10^{-3}$. This change occurs in much less than 1 ms, so it can be considered completely non-adiabatic on the timescale of the axial dynamics, set by the inverse of the trap frequency $\nu_z^{-1} \approx 100$ ms. The atoms, initially in a minimum of the potential, suddenly experience a non-equilibrium configuration and start oscillating around the center of the displaced trap.

Quadrupole and transverse breathing modes. The procedure for the excitation of these shape oscillations is different. Instead of suddenly modifying the trap potential, we (quasi-)resonantly excite these modes by modulating in time the trapping frequencies. In our setup the simplest way to produce this effect is by changing the bias field b_0, which enters the radial trap frequency (2.13). In the experiment we modulate the current flowing in the pair of compensation coils having the same symmetry axis $\hat{z}$ of the trap with a function generator (Agilent 33120A) driving the current controller. According to Eq. (2.13), the time-dependent bias field

$$b_0(t) = b_0(0)\left[1 + \alpha \sin(\Omega t)\right] \tag{3.36}$$

produces a modulation of the radial trap frequency

$$\omega_\perp(t) = \omega_\perp(0)\left[1 - \frac{\alpha}{2}\sin(\Omega t) + O(\alpha^2)\right]. \tag{3.37}$$

This mechanism is quite efficient for the selective excitation of collective modes, provided that the modulation frequency Ω is close to the eigenfrequencies of the

system. We typically apply five cycles of resonant modulation with $\alpha = 0.02$, corresponding to 1% variation of the trap frequency.

After the excitation of the collective mode we wait for different evolution times Δt in the harmonic + periodic potential, then we suddenly switch off both the magnetic trap and the optical lattice. The diagnostic of the condensate is made after 29 ms of expansion, when we take an absorption image of the atomic cloud. In the case of the dipole mode, we extract the center-of-mass position of the condensate along the lattice axis from the fit of the measured density distribution with a Thomas-Fermi profile. In the case of the quadrupole and transverse breathing modes, we consider the aspect ratio $\lambda = R_z/R_\perp$, defined as the ratio between the axial and the radial (Thomas-Fermi) widths of the condensate[5]. In both the cases, we consider the evolution of these observables as a function of Δt and from a fit of the experimental data with a sinusoidal function we extract the frequency of the mode we are studying.

The investigation of collective excitations after a (fixed) time of flight is a common procedure used in many experimental works [58, 15, 16, 93] to increase the accuracy of the measurement. As a matter of fact, the expansion modifies both the phase and the amplitude of the oscillation. This can be easily understood considering the fact that, after expansion, one obtains a combined information on the density distribution $\rho(\mathbf{r})$ and the velocity field $\mathbf{v}(\mathbf{r})$ at the moment of release from the trap. In any case, the frequency of the mode and the damping rate (if a damping is present) are not modified at all by the expansion.

For the highest lattice heights considered in the experiment ($s \simeq 5$) the density distribution after expansion shows interference peaks at momenta $+2\hbar k$ and $-2\hbar k$. In this case both the center-of-mass position (for the dipole mode) and the aspect ratio (for the quadrupole and transverse breathing modes) refer to the central density peak.

Dipole mode. The experimental points in Fig. 3.5A clearly show that the frequency of the dipole mode gets smaller with increasing lattice height s. This dependence has already been investigated in [20] in conjunction with the current/phase dynamics in a linear chain of Josephson junctions. The line shows the theoretical value of the dipole frequency calculated from Eq. (3.32) with the measured value of the trapping frequency ω_z and the effective mass m^* obtained from a single-particle band structure calculation. Indeed, for our experimental parameters, the effective mass depends only weakly on the presence of interactions, and can thus be calculated with good approxima-

[5]The measurement of the aspect ratio, and not of the axial and radial widths separately, contributes to an increase of the signal-to-noise ratio, since in the Thomas-Fermi limit this quantity does not depend on the shot-to-shot fluctuations in the number N of condensed atoms, differently from the absolute widths which indeed depend on N.

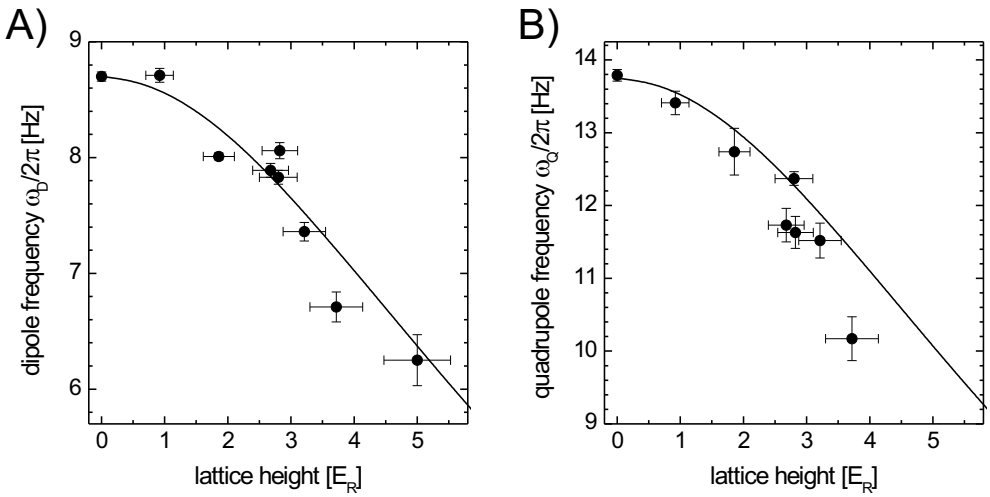

Figure 3.5: Frequencies of the dipole (A) and the quadrupole (B) modes for a BEC trapped in a harmonic + periodic potential. The points show the measured frequencies as a function of the lattice height. The lines are obtained rescaling the trap frequency ω_z with the effective mass m^* (see Sec. 3.2.1) introduced by the lattice.

tion using a single-particle model. The agreement between the experimental points and the theoretical curve is remarkable, demonstrating that the simple effective mass scaling well explains the experimental findings. As a matter of fact, this scaling of the dipole mode frequency with the effective mass can be obtained also from the single-particle band theory, integrating the semi-classical equations of motion (1.35) and (1.36) in the limit of small amplitude oscillations. The frequency of the dipole mode is indeed independent on the nature of the fluid under investigation (interacting or not, superfluid or not), differently from the case of the quadrupole mode, whose frequency strongly depends on the properties of the system.

Quadrupole mode. In Fig. 3.5B we show the frequency of the quadrupole mode as a function of the lattice height s. The experimental points clearly indicate that also the frequency of the quadrupole mode, characterized by a breathing oscillation along the lattice axis, decreases with increasing lattice height. Again, the line shows the theoretical frequency calculated from Eq. (3.33) with the effective mass m^* obtained from a single-particle band structure calculation. Also for the quadrupole mode the experimental results can be nicely explained in terms of a modified (single-particle) effective mass at the bottom of the band. We remark that the quadrupole frequency strongly depends on the interactions between the atoms forming the BEC, as indicated

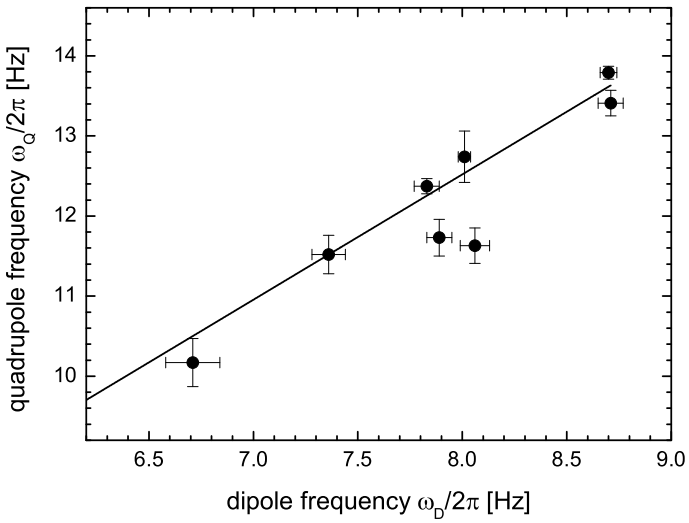

Figure 3.6: Frequency of the quadrupole mode as a function of the dipole mode frequency for different lattice heights. The line is a fit of the experimental data with a linear function, giving a slope 1.57 ± 0.01, in very nice agreement with the theoretical value $\sqrt{5/2} \simeq 1.58$ holding for a highly elongated harmonically trapped condensate in the Thomas-Fermi limit [41].

by the factor $\sqrt{5/2}$ in Eq. (3.33), that is peculiar of the superfluid nature of the system. In particular, from Eqs. (3.32) and (3.33) it turns out that, even in the presence of the periodic potential, the quadrupole and the dipole frequencies are still proportional, independently of the lattice height:

$$\omega_Q = \sqrt{\frac{5}{2}}\omega_D. \tag{3.38}$$

In order to check this relation, we have plotted in Fig. 3.6 the quadrupole mode frequency as a function of the dipole mode frequency varying the lattice height from $s = 0$ to $s = 3.7$. From a linear fit of the experimental data we obtain a a slope 1.57 ± 0.01 in very good agreement with the theoretical prediction $\sqrt{5/2} \simeq 1.58$.

Increasing the lattice height above $s = 4$ presents some technical difficulties, related to the nature of the excitation procedure. If the lattice height becomes bigger the frequency of the quadrupole mode decreases, hence the time needed for the resonant excitation, as well as the period of the oscillation that has to be detected, increases. As a matter of fact, for the maximum lattice height considered in the experiment, we start to observe a significant heating of the trapped sample. The final temperature of the atomic cloud $T \simeq 150$ nK, measured from the width of the thermal component after the

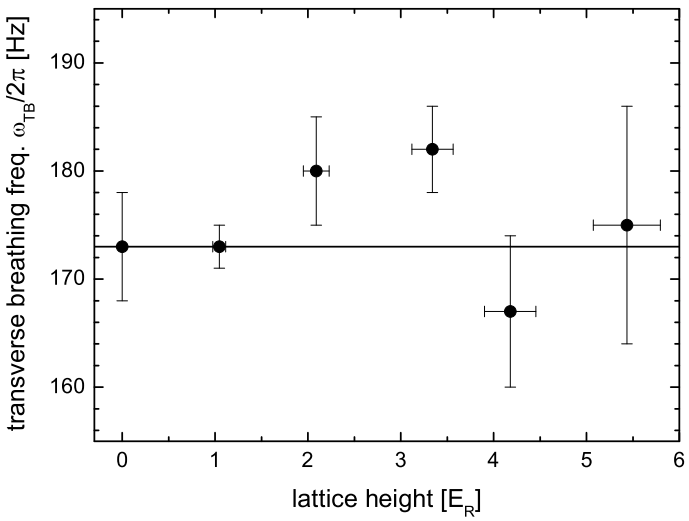

Figure 3.7: Frequency of the transverse breathing mode for a BEC trapped in a harmonic + periodic potential. The measured frequencies (filled circles) show no appreciable dependence on the lattice height. The line corresponds to the theoretical value $2\omega_\perp$ (see Sec. 3.2.1).

excitation of the collective mode, is consistent with the heating rate measured in our apparatus even in the absence of the optical lattice.

Transverse breathing mode. In Fig. 3.7 we show the frequency of the transverse breathing mode as a function of the lattice height s. The experimental data are in agreement with the expected value (3.34) indicated by the horizontal line and no dependence on the lattice height is observed. This confirms the prediction that the dynamics of the condensate along the transverse direction is not affected by the periodic potential.

This experiment demonstrates that the lowest energy excitations of a trapped BEC in the presence of a periodic potential can be well described by an extension of the hydrodynamic equations of superfluids for a harmonically trapped BEC [91]. The main result of such an analysis is the prediction that the frequencies of the modes which involve an oscillation of the cloud along the lattice axis (in our case the axial dipole and the axial breathing modes) are modified according to a simple effective mass scaling. The frequencies of the modes which involve an oscillation of the cloud along the orthogonal directions (in our case the transverse breathing mode) are not modified. Although the theoretical treatment of [91] is strictly valid only in the tight binding regime, our experiment shows that it gives reliable results also for small lattice heights.

3.3 Large amplitude oscillations

3.3.1 Introduction

As we have seen in the previous section, for small amplitude oscillations the dynamics of the BEC in a harmonic + periodic potential is well described in terms of a frequency shift induced by the different effective mass at the bottom of the band. In the case of dipole oscillations the single particle Bloch theory, strictly valid for a noninteracting system, is a good model to describe the experimental findings. However, when the amplitude of the oscillation becomes "larger", nontrivial effects connected with the interactions among atoms forming the BEC deeply modify this simple picture. In [83] the authors use a 1D tight binding model to predict the occurrence of a dynamical superfluid-insulator transition for large amplitude oscillations of a BEC in a harmonic + periodic potential. When the center-of-mass velocity is larger than a critical value, a rapid growth of excitations breaks the phase coherence of the system, resulting in the disruption of the superfluid oscillations. This is ultimately due to the *nonlinearity* introduced by the repulsive mean field term in the GPE combined with the *periodicity* set by the lattice.

The theoretical analysis of [83] is made in the tight binding limit discussed in Sec. 1.2.4, where one can derive analytical results. Including the nonlinear term and the harmonic trap potential Eq. (1.44) becomes

$$i\hbar\frac{d\Phi_j}{dt} = -K\left(\Phi_{j-1} + \Phi_{j+1}\right) + \epsilon_j\Phi_j + U|\Phi_j|^2\Phi_j, \tag{3.39}$$

where Φ_j is the complex amplitude of the wavefunction in the j-th site, K is the tunnelling rate, $U = gN\int d\mathbf{r}|\Psi|^4$ is the interaction energy and $\epsilon_j = \Omega j^2 = \frac{1}{2}m\omega_z^2 d^2 j^2$ is the on-site energy due to the harmonic confinement, with d the lattice spacing. We will refer to this equation as the Discrete Nonlinear Schrödinger Equation (DNLSE). In the absence of confinement ($\epsilon_j = 0$), among the stationary solutions of Eq. (3.39) we consider the Bloch states $\Phi_j = \Phi_0 e^{i(jqd - Et/\hbar)}$ with energy $E = -2K\cos(qd) + U|\Phi_0|^2$, where q is the quasimomentum. In order to study the stability of the system, the authors of [83] perturb this state with small amplitude phonon excitations with wavenumber p, whose energy spectrum turns out to be

$$\hbar\omega = 2K\sin(qd)\cos(pd) \pm 2\sqrt{4K^2\cos^2(qd)\sin^4\left(\frac{pd}{2}\right) + 2KU|\Phi_0|^2\cos(qd)\sin^2\left(\frac{pd}{2}\right)}. \tag{3.40}$$

For $q > \pi/2d$ the argument of the square root becomes negative for sufficiently small values of the excitation wavenumber p. In this case complex frequencies appear in the excitation spectrum, corresponding to an exponential growth of perturbations which may eventually destroy the initial state. The condition

$q = \pi/2d$ coincides with the situation in which the phase difference between adjacent sites is exactly equal to $\pi/2$. A naive interpretation of this mechanism is the following: when the center-of-mass velocity exceeds a critical value (and correspondingly the phase gradient across the sites becomes bigger than $\pi/2$), the tunnelling is not fast enough to lock the phases of adjacent sites, which start to run independently and the system loses its long range coherence. As a matter of fact, entering this unstable regime one expects to observe the following phenomena, as confirmed by numerical simulations [83]:

- The phases of adjacent sites become completely uncorrelated and the long range coherence of the superfluid state is rapidly lost. The lattice sites are still occupied by coherent states, but their phases start evolving independently (according to the on-site chemical potential). As a consequence, one expects to observe the disappearance (or at least a strong suppression) of the interference peaks in the expansion.

- Because of this effective dephasing among the lattice sites, the atomic current ceases to be driven by a coherent tunnelling process. The center-of-mass stops oscillating and the atomic sample stays blocked on a side of the harmonic potential. Tunnelling processes are still present, but their average effect on the center-of-mass motion is null.

For a harmonically trapped condensate ($\epsilon_j = \Omega j^2$) the above results are still valid, provided that the width of the wavepacket is much larger than the lattice spacing. In this case the trapping potential is treated as an external force driving the dynamics of the system. In the case of dipole oscillations induced by a displacement Δz of the trapping potential, the critical displacement above which one enters the unstable regime can be analytically calculated as

$$\Delta z_{cr} = \sqrt{\frac{4K}{m\omega_z^2}}. \tag{3.41}$$

The maximum velocity reached by the center-of-mass for this displacement is

$$v_{cr} = \frac{2Kd}{\hbar}, \tag{3.42}$$

that is the critical velocity for which the excitation spectrum of the DNLSE develops complex frequencies. We note that this critical velocity, as well as the critical displacement Δz_{cr}, depends on the tunnelling rate K, which decreases with increasing lattice height s.

This instability, called in [83] *modulational instability*, is more extensively treated in Sec. 4.3, where a more general approach, valid outside the tight binding limit, is presented. Indeed, this kind of instability, also called *dynamical instability*, is a general feature of nonlinear systems described by a GPE-like equation with a positive nonlinear term and a periodic external potential. For BECs with repulsive interactions in optical lattices it has been theoretically studied also in [8, 49, 50, 84, 94, 95, 96, 97].

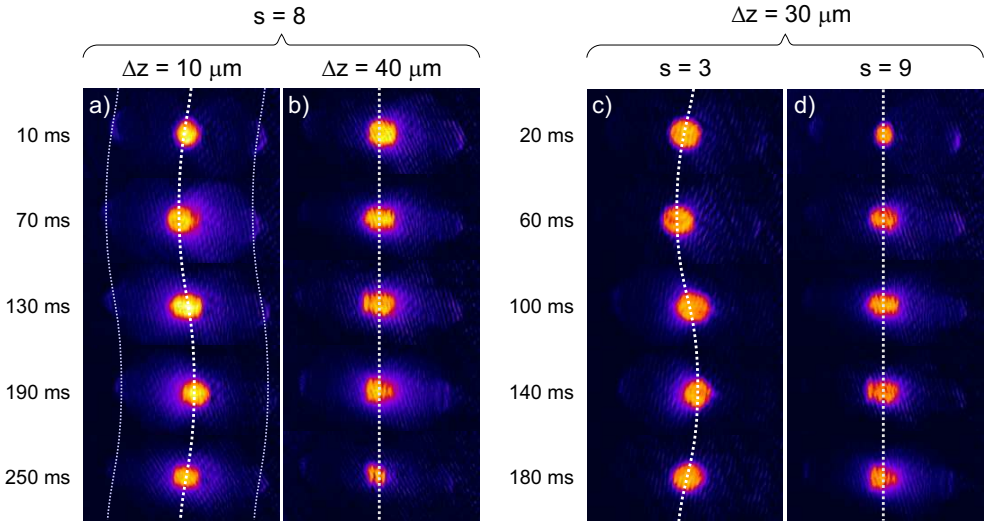

Figure 3.8: Absorption images of the expanded condensate after different evolution times in the harmonic trap + optical lattice. A dipole oscillation is excited by a sudden displacement Δz of the magnetic trap along the lattice axis (horizontal in figure). While in the cases a) and c) a nice oscillation can be seen, for the parameters of b) and d) the center-of-mass dynamics is blocked and the density distribution presents some complex structures.

3.3.2 The experiment

The large amplitude dipole oscillations are excited following the procedure described in Sec. 3.2.2: the condensate is produced in the ground state of the combined harmonic and periodic potential, then the center of the magnetic trap is suddenly shifted along the lattice axis by changing the configuration of the currents flowing in the trap coils. Let us consider a lattice height $s = 8$. For small trap displacements a nice center-of-mass oscillation can be observed at the frequency of the magnetic trap rescaled by the effective mass m^* calculated at the bottom of the band. This is the case shown in Fig. 3.8(a) for a trap displacement $\Delta z = 10$ μm. Increasing the displacement, instead of a larger amplitude oscillation, we observe the transition to an insulating regime in which the condensate stops oscillating and the center-of-mass motion is suppressed, as shown in Fig. 3.8(b) for a trap displacement $\Delta z = 40$ μm. The same behavior can be observed increasing the lattice height for a fixed trap displacement, as shown in Fig. 3.8(c,d) for $\Delta z = 30$ μm.

If the sampling of the expanded center-of-mass position as a function of time is sufficiently dense, we can reconstruct the motion in the trap by assuming that the condensate moves with constant velocity between two consecutive points. In Fig. 3.9 we show the center-of-mass position in the trap for different

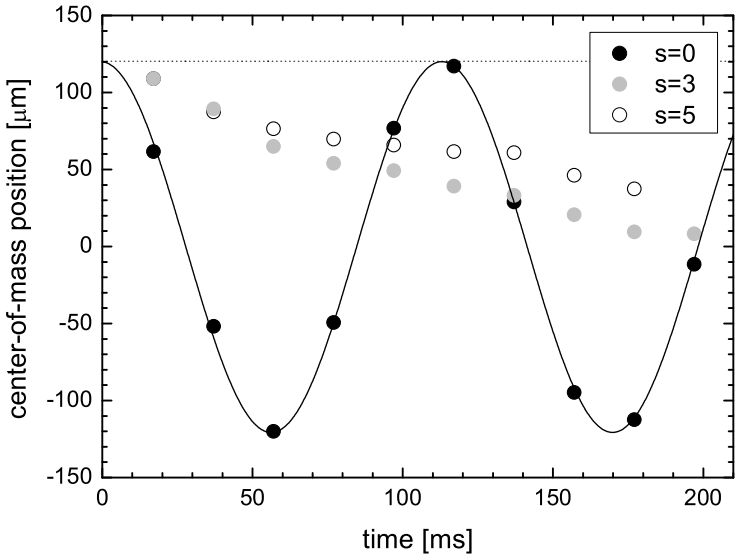

Figure 3.9: Center-of-mass position of the atomic cloud in the trap as a function of time after a trap displacement $\Delta z = 120$ μm. While for $s = 0$ the condensate performs an oscillation, when the lattice height is $s = 3$ and $s = 5$ the cloud, instead of oscillating, slowly moves towards the trap center.

lattice heights and a trap displacement $\Delta z = 120$ μm: while for $s = 0$ the condensate performs a clear oscillation, when the lattice height is $s = 3$ and $s = 5$ the atomic cloud, instead of oscillating, slowly moves toward the center of the trap, where it subsequently stops.

In Fig. 3.10 we plot a "phase" diagram in which we report the observed dynamical regime as a function of the lattice height and the trap displacement. The filled circles represent oscillations, while the empty circles denote an overdamped motion towards the trap center. The continuous line denotes the critical displacement (3.41) which should separate the two regimes according to the 1D tight-binding model developed in [83]. As one can see, this model gives a reliable estimate for the transition between the two dynamical regimes. However, there are some important differences between the experimental findings and the model developed in [83]:

- In the non-oscillating regime, for trap displacements just above Δz_{cr}, the atomic cloud is not pinned at a side of the trapping potential, as predicted in [83], but slowly moves towards the trap center.
- The interference peaks at $-2\hbar k$ and $+2\hbar k$ in the expanded density distribution are not completely washed out. Actually, we observe the appearance of more complex structures (irregular density modulations) within the three visible peaks. Only for very large displacements $\Delta z \sim 100$ μm

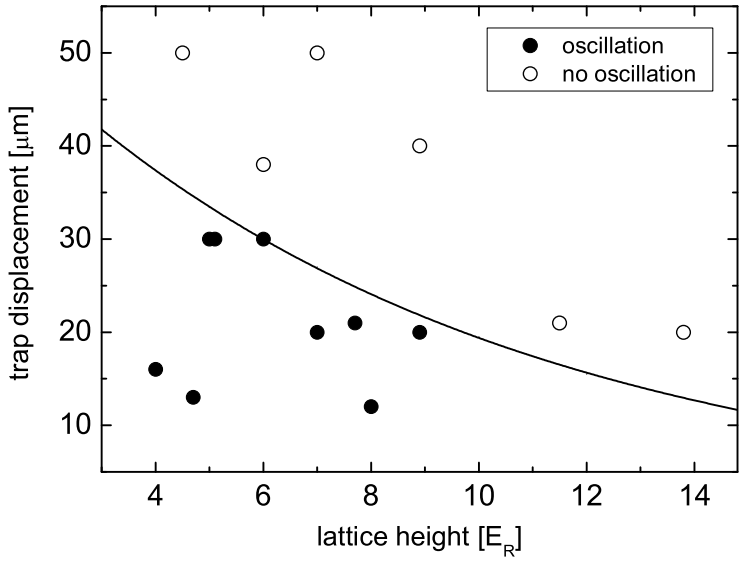

Figure 3.10: "Phase" diagram of the dynamical regimes for a BEC in a combined harmonic + periodic potential once the trap center is displaced along the lattice direction. Filled circles represent experimentally observed oscillations, while empty circles denote a slow overdamped motion towards the trap center. The line indicates the critical displacement analytically calculated in [83] separating the two regimes.

> we observe a dramatic broadening of the density distribution and the complete disappearance of the interference peaks.

Therefore, as a general comment, the transition observed in the experiment is not as sharp as the one predicted in [83]. Varying the trap displacement across the critical value Δz_{cr} for a fixed lattice height, both the center-of-mass motion and the density distribution after expansion evolve continuously from one regime to the other, suggesting that the actual transition is much smoother. However, keeping in mind these limitations, the 1D model is capable of well addressing the separation between the two regimes and has the merit to give analytical results for the transition point.

Actually, the 1D model does not include the excitation of the radial degrees of freedom, which could play a significant role in the evolution of the system in the insulating regime. In [84] the authors show that, owing to the 3D nature of the system, the breakdown of the superfluid current above the critical displacement is not associated with a sharp transition, but there exists a range of displacements for which the coherence across the sample can be partially restored. In this work they compare the numerical solution of the full 3D-GPE for the parameters of our experiment with the results of two different 1D

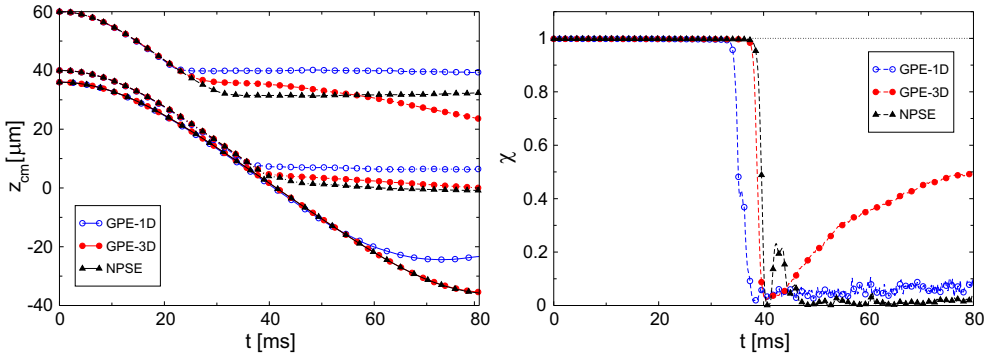

Figure 3.11: Results of the numerical integration of the 1D-GPE, 3D-GPE and NPSE (taken from [84]). Left) Center-of-mass position for a lattice height $s = 5$ and three different trap displacements $\Delta z = 36$, 40 and 60 μm. Right) Evolution of the coherence (3.43) as a function of time for a lattice height $s = 5$ and a trap displacement $\Delta z = 40$ μm.

models: the 1D-GPE (whose discretized version DNLSE has been used in the tight binding approach of [83]) and the NPSE (Non Polynomial Schrödinger Equation, an effective 1D model [98, 99] that takes into account also the radial degrees of freedom).

The graph on the left of Fig. 3.11 (taken from [84]) shows the center-of-mass position as a function of time for a lattice height $s = 5$ and different trap displacements. In the case of the largest displacement $\Delta z = 60$ μm, the solution of the 3D-GPE clearly shows that in the insulating regime the center of mass slowly moves towards the trap center, as indeed observed in the experiment, while the 1D-GPE predicts that it stays pinned on a side of the harmonic potential. The graph on the right of the same figure shows how the coherence of the sample evolves in time. The coherence χ is naturally defined as a correlation integral between the complex amplitudes at adjacent sites

$$\chi = \left| \int d\mathbf{r}\, \Phi^*(x,r)\Phi(x+d,r) \right|^2 , \tag{3.43}$$

normalized in such a way to be 1 for an entirely coherent sample (when the phase difference between neighboring sites is constant across the lattice) and 0 for a totally incoherent sample (when the phases are completely uncorrelated). While the solution of the 1D-GPE indicates that, after the onset of instability at $t \simeq 35$ ms, the coherence χ suddenly drops to zero (as predicted in [83]) and cannot be recovered, the integration of the full 3D-GPE shows that a relevant fraction of the initial coherence can be restored in few tens of ms. This revival of coherence in the 3D case shows that the radial degrees of freedom play indeed an important role in the reorganization of the system after the

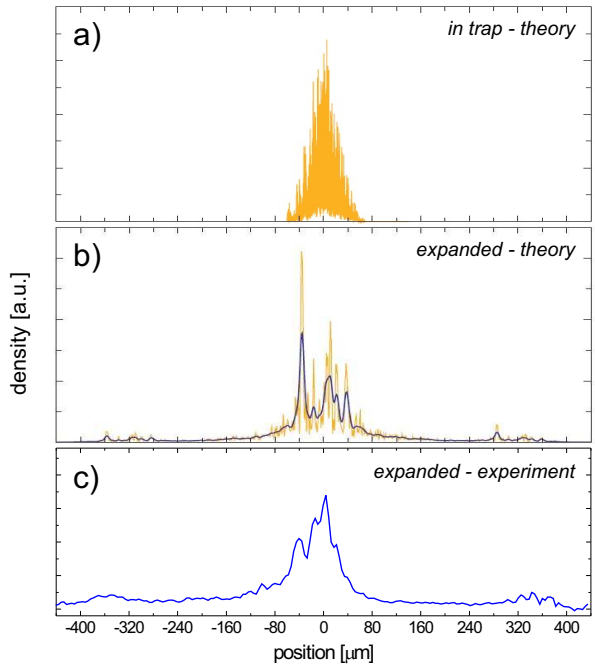

Figure 3.12: Density profile after $t = 70$ ms of evolution in the combined harmonic + periodic potential for a lattice height $s = 5$ and a trap displacement $\Delta z = 40$ μm (adapted from [84]). From top to bottom: a) density distribution in the trap calculated in [84]; b) density distribution after 28 ms expansion calculated in [84]; c) density distribution measured in the experiment after 28 ms expansion.

occurrence of dynamical instability and could explain the persistence of high contrast interference peaks that we experimentally observe in the insulating regime. The NPSE does not account for this rephasing mechanism, because the effective coupling between axial and radial degrees of freedom does not include information on the phase dynamics [84].

In Fig. 3.12 (adapted from [84]) we compare the density distribution obtained from the numerical integration of the 3D-GPE with the one measured in the experiment. The graph (a) shows the calculated density distribution in the trap after 70 ms of evolution in the combined harmonic + periodic potential for a lattice height $s = 5$ and a trap displacement $\Delta z = 40$ μm. The graph (b) shows the density distribution calculated from (a) assuming 30 ms of ballistic expansion, i.e. neglecting mean field effects in the expansion[6].

[6]Most of the initial energy of the condensate is associated with the fast density modulation due to the localization in the lattice sites, as shown in Fig. 3.12a. In this regime the kinetic energy dominates on the interaction energy and it is therefore correct to neglect the latter (at least for the expansion in the axial direction).

The dark thick line is the convolution of the expanded density distribution with a gaussian function (width 6 μm), in order to take into account the finite optical resolution of the imaging system. From this procedure we can clearly observe the persistence of some structures around ± 320 μm, corresponding to momentum components around $\pm 2\hbar k$. Even if the visibility of these lateral peaks is reduced from the fully coherent case, they are an indication that the coherence is not completely lost. We also observe the appearance of irregular fringes in the central peak, whose presence is an additional signature of the partial loss of coherence. As a comparison, we show in graph (c) the axial cross section of the experimentally recorded density profile for the same parameters of (b). Even if the position of the fringes in the central peak is not precisely the same (since it strongly depends on the initial conditions and the exact timing), there is a qualitative agreement between the calculated distribution and the measured one.

Chapter 4

Dynamics of a BEC in a moving optical lattice

The experiments described in the previous chapter have been performed with a Bose-Einstein condensate moving in a static optical lattice. Studying collective excitations, we have observed that the dynamics of the system can be explained in terms of an effective mass m^* leading to a shift of the collective modes frequencies. This picture is valid in the case of small amplitude oscillations, when the dynamics is limited to regions of the energy spectrum in which the dispersion law is parabolic. If we want to explore effects related to the full band structure in a controlled way, we need an experimental procedure that allows us to easily reach different regions of the Brillouin zone. In order to do this we use a *moving* optical lattice: by tuning the lattice velocity we can selectively access states with well defined quasimomentum and band index.

In a first experiment [31] we have studied the expansion of the BEC through the moving lattice. In this low density regime the single-particle band theory introduced in Sec. 1.2.1 gives an excellent description of the observed dynamics. A precise band spectroscopy of the system in the first and excited energy bands is carried out by looking at the real-space propagation of the atomic wavepacket in the optical lattice. We report the observation of a *lensing effect*, i.e. a change in the condensate shape after expansion through the lattice, which can be explained in terms of a modified dispersion of the matter wavepacket induced by the periodic potential. When the effective mass becomes negative (anomalous dispersion), the initially expanding condensate starts to compress along the lattice direction instead of continuing its expansion (as in the case of normal dispersion). The strength of this effect can be controlled tuning the initial velocity of the condensate in the lattice frame.

In a second experiment [32] we have studied the time evolution of a harmonically trapped BEC loaded in the moving lattice. In this high density regime, in which nonlinearities play an important role, the Bloch waves are no longer stable solutions of the Gross-Pitaevskii equation and different forms

of instabilities take place [8, 97]. The lifetime of the condensate in such a potential exhibits a dramatic dependence on the quasimomentum state, which we unambiguously attribute to the onset of *dynamical instability*. This mechanism has already been studied in Sec. 3.3 as the process responsible for the breakdown of coherent oscillations of the BEC in the harmonic + periodic potential. This kind of instability, driven by repulsive nonlinearities in a periodic potential, occurs when the excitation spectrum of the system presents complex frequencies, so that noise-induced perturbations of the wavefunction may grow exponentially in time, eventually destroying the initial state. The observed dynamics, featuring a nontrivial behavior near the band edges and the appearance of complex structures in the expanded atomic density profile, is compared with the numerical solution of the GPE, showing the validity of this interpretation. Working with a finite temperature sample we have also evidenced a different loss mechanism out of the dynamically unstable regime, which we relate to the onset of *energetic instability*. By using a time-resolved analysis of the atom losses in different regions of the quasimomentum space and for different temperatures we have clearly separated and characterized these two instability regimes.

4.1 A moving optical lattice

If we want to investigate in detail the full band structure of a BEC in an optical lattice we need to accurately control the relative motion of the condensate with respect to the periodic potential. In the experiments described in the previous chapter this task was accomplished by setting the BEC into motion through an optical lattice at rest in the laboratory frame. What about moving the lattice instead of the condensate? In the next sections we will show how the optical lattice can be moved in a much more controlled way than the atoms, allowing for a precise addressing of single Bloch states.

4.1.1 Some mathematics

A moving optical lattice can be obtained from the interference of two counterpropagating laser beams with slightly different frequencies. Let us consider two electromagnetic waves travelling in opposite direction along the z axis and linearly polarized along the same direction $\hat{e}$:

$$\mathbf{E_1}(z,t) = \hat{e}E_1 \cos(k_1 z + \omega_1 t + \delta) \tag{4.1}$$

$$\mathbf{E_2}(z,t) = \hat{e}E_2 \cos(k_2 z - \omega_2 t - \delta). \tag{4.2}$$

The total intensity is proportional to the square modulus of the total field:

$$I(z,t) = \epsilon_0 c|\mathbf{E_1}(z,t) + \mathbf{E_2}(z,t)|^2. \tag{4.3}$$

Using some mathematics and averaging on the terms oscillating at the optical frequencies ω_1 and ω_2, we can write the average intensity as

$$I(z) = \frac{1}{2}\epsilon_0 c \left[(E_1 - E_2)^2 + 4E_1 E_2 \cos^2(kz - \frac{\Delta\omega}{2}t) \right], \tag{4.4}$$

where $\Delta\omega = \omega_2 - \omega_1 \ll \omega_1, \omega_2$ is the frequency difference between the two beams and $k = (k_1 + k_2)/2$ is the average wavenumber. In the particular case $E_1 = E_2 = E$ this expression reduces to

$$I(z) = 2\epsilon_0 c E^2 \cos^2(kz - \frac{\Delta\omega}{2}t) \tag{4.5}$$

representing a standing wave whose nodes and antinodes move in the laboratory frame at a constant velocity

$$v_L = \frac{\Delta\omega}{2k} \tag{4.6}$$

Using Eq. (3.7) for the dipole potential, it immediately follows that this field configuration produces an optical lattice with spacing $d = \pi/k$ moving with constant velocity in the laboratory frame:

$$V(z) = V_0 \cos^2 \left[k(z - v_L t) \right]. \tag{4.7}$$

Following Eq. (4.6), the lattice velocity v_L can be easily controlled by adjusting the frequency difference $\Delta\omega$ of the two lattice beams.

4.1.2 Experimental setup

The derivation presented in the above section is correct provided that the phase difference δ between the two radiation fields is constant. This condition can be experimentally achieved if the beams producing the optical lattice are derived from the same laser source and then coherently frequency-shifted, in order to provide a stable detuning $\Delta\omega$. In a different way, this condition could be realized with two independent laser beams whose relative phase is stabilized by an optical phase-locked loop.

The experimental setup for the production of the moving optical lattice is schematically shown in Fig. 4.1. A commercial Ti:Sa ring laser (Coherent 899) is pumped by an high power solid state laser (Coherent Verdi V8). The beam coming from the Ti:Sa laser is split into two beams of adjustable intensities, which are then frequency shifted by two AOMs driven by two phase-locked radiofrequency generators (Agilent 33120A). In order to convey the light to the experiment area, we use two polarization-maintaining fibers.

In principle, the bandwidth of the phase-locked loop locking the two radiofrequency generators should be enough to make the frequency difference between the two laser beams stable at the sub-Hz level. Actually, since the

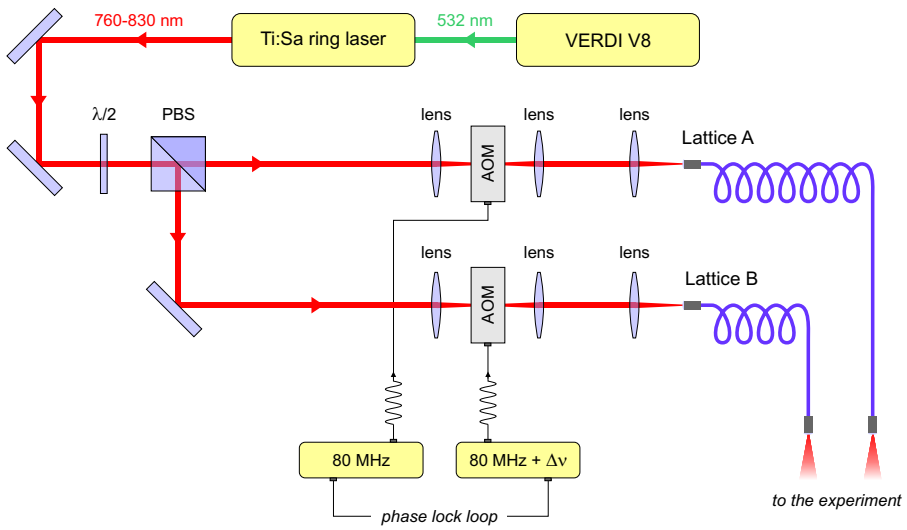

Figure 4.1: Schematics of the setup for the production of the moving optical lattice. The beam coming from a Ti:Sa laser is split into two separate beams, that are then modulated by two AOMs driven by two phase-locked radiofrequency generators. Two optical fibers are used to convey the light to the experiment.

two beams experience a different optical path before arriving to the vacuum cell, mechanical noise on the optics can induce a significant phase noise on the laser fields, degrading the quality of the phase-locked modulation. We have quantified this effect by observing the beating of the two laser fields on a fast photodiode and processing the signal with a spectrum analyzer (Fig. 4.2). The beat note has been fitted with a lorentzian shape, resulting in a HWHM $\delta\left(\frac{\Delta\omega}{2\pi}\right) = 197(6)$ Hz $\simeq 0.05 E_R/h$. Using Eq. 4.6 this finite width corresponds to an uncertainty $\delta v_L = 0.01 v_B$ on the lattice velocity.

This random phase modulation results in an effective shaking of the periodic potential at the frequencies typical of mechanical vibrations. If the laser creating the optical lattice is far detuned from the atomic resonance, so that heating due to the absorption of lattice photons can be neglected, this can be the limiting factor to the finite lifetime of the BEC in the periodic potential. In order to evaluate this effect, we have measured the lifetime of the condensate in the stationary lattice using two different configurations. In the first setup we have used two independent beams, both modulated at the same frequency, as described above. In the second setup we have used only one retroreflected beam, as in the experiments described in the previous chapter. The BEC is trapped in the harmonic potential in the presence of an RF-shield removing the thermal atoms produced by heating of the atomic sample.

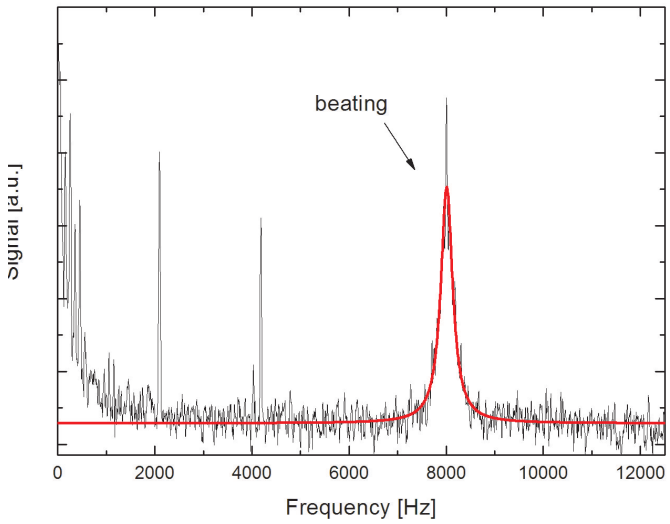

Figure 4.2: Frequency spectrum of the beat note of the two laser beams producing the optical lattice observed on a fast photodiode. The thick line is a fit with a lorentzian shape, resulting in a HWHM $\delta\left(\frac{\Delta\omega}{2\pi}\right) = 197(6)$ Hz.

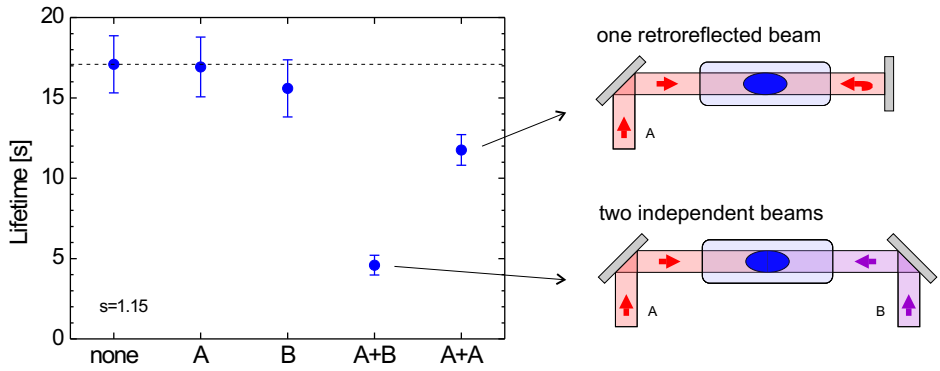

Figure 4.3: Lifetime of the BEC trapped in the harmonic potential for different experimental conditions: with no lattice beams ("none"), with one lattice beam only ("A" and "B"), with both the lattice beams ("A+B"), with one retroreflected beam ("A+A"). The laser parameters are $\lambda = 820.5$ nm and $I_0 = 15$ W/cm^2.

The results are shown in Fig. 4.3 for the laser parameters $\lambda = 820.5$ nm and $I_0 = 15$ W/cm^2, giving a lattice height $s = 1.15$ in units of recoil energy E_R. For this choice of the parameters the lifetime of the BEC held in the magnetic trap and exposed to a single lattice beam ($\tau_A = 16.9(1.9)$ s for one beam and $\tau_B = 15.6(1.8)$ s for the other beam) is consistent with the lifetime of the BEC in the pure magnetic trap $\tau_0 = 17.0(1.8)$ s. This measurement confirms the expectation that in the far-off resonant regime ($\Delta \simeq 25$ nm from the D1 Rb line) heating due to spontaneous scattering of laser photons can be neglected and the lifetime of the BEC is limited by other heating mechanisms (mainly, the current noise on the magnetic trap coils and collisions with the background gas). Instead, when both the lattice beams are present, we observe a significant change in the BEC lifetime, that drops to $\tau_{AB} = 4.6(0.6)$ s for the configuration with independent lattice beams. In the other configuration, when the lattice is created by the retroreflection of a single beam, we measure a lifetime $\tau_{AA} = 11.8(1.0)$ s, still shorter than the lifetime of the BEC in the pure magnetic trap, but significantly longer than the lifetime measured for the configuration with independent beams. This observation suggests that, when the two lattice beams experience longer separate optical paths (with more optical elements that are not in common), the accumulated phase noise in the optical oscillation is larger, resulting in an effective shaking of the optical lattice and an higher heating of the atomic sample.

4.1.3 Loading the BEC into the moving lattice

Let us consider a condensate at rest in the laboratory frame and an optical lattice moving with velocity $-v_L$. In the frame of the periodic potential the condensate has a velocity v_L (that we will consider positive), hence a momentum $\hbar q = m v_L$. Let us indicate this state with the symbol $|q\rangle$, denoting an eigenstate of the momentum operator. From Eq. (1.33) it follows that a Bloch state $|n, q\rangle_B$ may be expanded on the set of the momentum eigenstates:

$$|n, q\rangle_B = \sum_{j=-\infty}^{\infty} a_j^{n,q} |q + 2kj\rangle. \tag{4.8}$$

It is easy to demonstrate that, because the Bloch states form a complete basis, a momentum state $|q\rangle$ may be similarly expanded on a set of Bloch states with quasimomentum q and different band indexes n:

$$|q\rangle = \sum_{n=1}^{\infty} b_n^q |n, q\rangle_B. \tag{4.9}$$

If we suddenly switch on the optical lattice, the momentum state $|q\rangle$ will be projected onto a superposition of Bloch states $|n, q\rangle_B$ belonging to different bands [47]. Instead, if the optical lattice is switched on slowly enough, with

respect to the energy difference between different bands, only one Bloch state will get populated. This state is labelled by the quantum numbers

$$q = \left(\frac{v_L}{v_B}\right) k \tag{4.10}$$

$$n = \left[\frac{v_L}{v_B}\right], \tag{4.11}$$

where $v_B = \hbar k/m$ is the so-called *Bragg velocity* and the operator $[x]$ indicates the integer part of x.

In order to understand the origin of Eqs. (4.10)-(4.11), let us consider the limiting case of a periodic potential with zero intensity, as shown in Fig. 4.4A. In this fictitious potential the energy spectrum is identical to the free energy spectrum and thus we can identify the quasimomentum states with the momentum states. In particular, given a momentum state $|q\rangle$, it is straightforward to make the identifications $|q\rangle \equiv |1, q\rangle_B$ if $0 < q < k$, $|q\rangle \equiv |2, q\rangle_B$ if $k < q < 2k$, etc... If we increase the height of the periodic potential from zero to a finite value, as shown in Fig. 4.4B, energy gaps will appear at the zone boundaries and the free particle spectrum will be modified into energy bands. In particular, using the extended zone scheme, it is easy to understand that the n-th energy band arises from the deformation of the free particle spectrum in the n-th Brillouin zone. If this deformation of the energy spectrum is slow enough, the initial state adiabatically adapts itself to the new potential, remaining at each instant a stationary state of the time-dependent Hamiltonian. The requirement for this adiabatic passage is expressed by the condition [100]

$$\left|\left\langle n', q \left| \frac{\partial H}{\partial t} \right| n, q \right\rangle_B\right| \ll \frac{\Delta E^2(t)}{\hbar}, \tag{4.12}$$

where $|n, q\rangle_B$ and $|n', q\rangle_B$ denote, respectively, the initial state and a generic state with different band index, $\Delta E(t)$ is their energy difference, and $\partial H/\partial t$ is the time derivative of the Hamiltonian operator. We note that for quasimomenta lying at the zone boundaries it is impossible to satisfy the criterion imposed by Eq. (4.12), because at zero potential height the states belonging to adjacent bands are degenerate and $\Delta E = 0$. In the following sections we will extensively use the extended zone scheme, assuming that quasimomentum states in the n-th Brillouin zone belong to the n-th energy band.

Experimentally, in order to adiabatically load the condensate in the optical lattice, we slowly increase the intensity of the lattice beams from zero to the maximum value in a time Δt. For this purpose we apply a linear ramp to the intensity of the radiofrequency driving the AOMs. Even though we use a linear ramp, because of the nonlinear response of the AOMs, the actual ramp on the beam intensities is smoothed both at the beginning and at the end. The minimum rise time Δt, that is chosen to ensure adiabaticity, depends on the lattice height and the lattice velocity, but typically is of the order of a

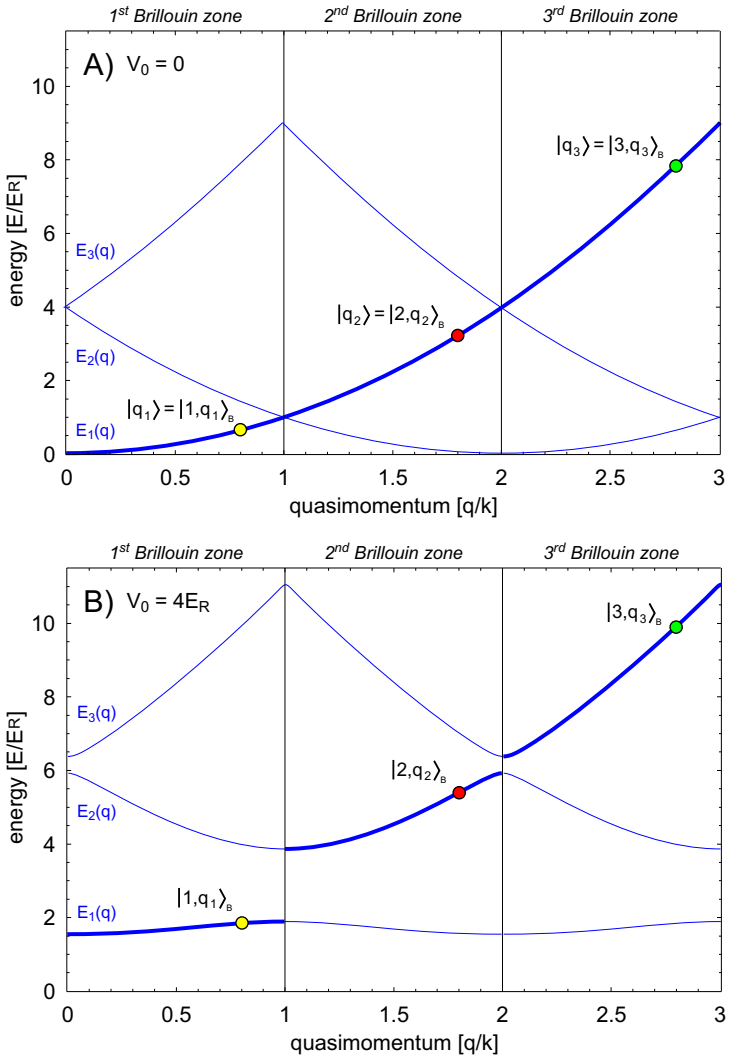

Figure 4.4: The BEC can be loaded in a single Bloch state by adiabatically increasing the height of the optical lattice from zero to its final value. A) At $t = 0$, when the periodic potential has zero amplitude, a natural identification of momentum states with quasimomentum states is possible. B) If the height of the periodic potential is increased slowly enough, the quasimomentum states adiabatically follow the new potential.

few ms. We check the adiabaticity of this loading procedure by applying a reverse ramp in the same time Δt. If the overall procedure is adiabatic, the initial momentum state $|q\rangle$ is slowly converted into a single Bloch state $|n, q\rangle_B$ by the ascending ramp and then is reverted back into the initial momentum

state $|q\rangle$ by the descending ramp: at the end only one momentum component will be detected. Instead, if the procedure is not adiabatic, the ascending ramp maps the momentum state $|q\rangle$ in a superposition of Bloch states $|n, q\rangle_B$ with several band indexes; the time evolution of these states will be different (because they have different energies) and, after the descending ramp, their interference will be mapped into a superposition of multiple momentum states $|q + 2kj\rangle$ differing by multiples of $2\hbar k$.

4.2 Expansion of a BEC in a moving optical lattice

4.2.1 Introduction

In a first experiment we have studied the expansion of a Bose-Einstein condensate through a moving optical lattice. The expansion of a BEC through a stationary lattice has already been studied in [101], in which effects on the condensate size due to the presence of the lattice have been seen. In our experiment, by controlling the lattice velocity, we have studied how the expansion of the condensate in the optical lattice changes as a function of the quasimomentum. First, we have carried out a precise band spectroscopy by looking at the real-space propagation of the matter wavepacket in the periodic potential. Then we have observed how it is possible to use a moving lattice to manage the dispersion of a cloud of ultracold atoms. One of most fascinating consequences of the Bloch theory is the possibility to describe the dynamics of a wavepacket in terms of a modified mass and even to have states with negative effective mass. In this section we will study how this property of periodic potentials can be used to produce a controlled focusing of the matter wavepacket, thus making the optical lattice act as a lens for matter waves.

Let us consider the expansion of a harmonically trapped condensate once the confining potential is removed. For the sake of simplicity, we can restrict to the one-dimensional case in which the expansion takes place in only one direction. After the first phase of the expansion, in which the mean-field energy is rapidly converted into kinetic energy, the nonlinear term in the Gross-Pitaevskii equation can be neglected and the wavepacket expands in free space according to the linear Schrödinger equation

$$i\hbar\frac{\partial\Psi}{\partial t} = -\frac{\hbar^2}{2m}\nabla^2\Psi. \tag{4.13}$$

Suppose now to switch on a moving optical lattice, along the same axis in which the expansion takes place, in order to load the condensate in a state with well defined quasimomentum q. In the frame of the optical lattice the expansion will continue according to the equation

$$i\hbar\frac{\partial\Psi}{\partial t} = -\frac{\hbar^2}{2m}\nabla^2\Psi + V_0\cos^2(kz). \tag{4.14}$$

We can naively assume that the effect of the periodic potential can be included in a modified kinetic term in which the real mass m is replaced with the effective mass m^*:

$$i\hbar\frac{\partial\Psi}{\partial t} \approx -\frac{\hbar^2}{2m^*}\nabla^2\Psi. \tag{4.15}$$

In this simple picture the periodic potential has the effect of changing the dispersion of the wavepacket, eventually inverting the sign of the dispersion when the effective mass is negative.

This problem is studied more quantitatively in [102], where the authors simulate the expansion of a cigar-shaped Bose-Einstein condensate propagating in an optical lattice. Instead of using the full 3D Gross-Pitaevskii equation, which generally requires a significant computational effort for its solution, they introduce a 1D effective model capable of taking into account both the axial and the radial degrees of freedom. This model combines the scaling and gauge transformations introduced in [103, 104] with the factorization of the condensate wavefunction into an axial function and a radial gaussian component, as in the case of the Non-Polynomial Schrödinger Equation (NPSE) introduced in [98, 99]. In the experiment proposed in [102], the authors consider the case of a cigar-shaped condensate initially in the ground state of a pure harmonic potential; they accelerate the condensate to a given velocity v and, after switching off the harmonic confinement, they increase the intensity of a static periodic potential during the expansion of the condensate. In Fig. 4.5A they report the axial size of the condensate as a function of time for different values of the initial velocity v of the condensate, hence different values of the quasimomentum $q = mv/\hbar$ [1]. The continuous line (a) shows the expansion of the condensate in a lattice with $s = 2$ for $q = 0$, when the effective mass $m^* \simeq 1.1m$ is close to the real mass. An interesting behavior is shown by the long-dashed line (b), which refers to the expansion of the condensate for $q = 0.7k$, close to the value for which the effective mass becomes infinite: as one can clearly see, after 15 ms, when the lattice intensity arrives at the final value, the expansion of the condensate along the lattice direction freezes and the axial size stays constant. Further moving towards the band edge, when the effective mass becomes negative, the condensate stops expanding and starts to compress along the lattice direction, as shown by the short-dashed line (c) for $q = 0.8k$, when the effective mass is $m^* \simeq -1.1m$. Finally, for $q = 1.2k$ in the second band, when the effective mass $m^* \simeq 0.3m$ is positive but smaller than the real mass, the axial expansion of the condensate is enhanced with respect to the normal case, as indicated by the dotted line (d).

The numerical solution of this Gross-Pitaevskii model confirms the first idea that the effect of the optical lattice on the expansion of the condensate can be modelled with a modified dispersion term depending on the effective

[1] We note that this adiabatic loading procedure is exactly the same we have discussed in Sec. 4.1.3, but is presented here in the rest frame of the lattice.

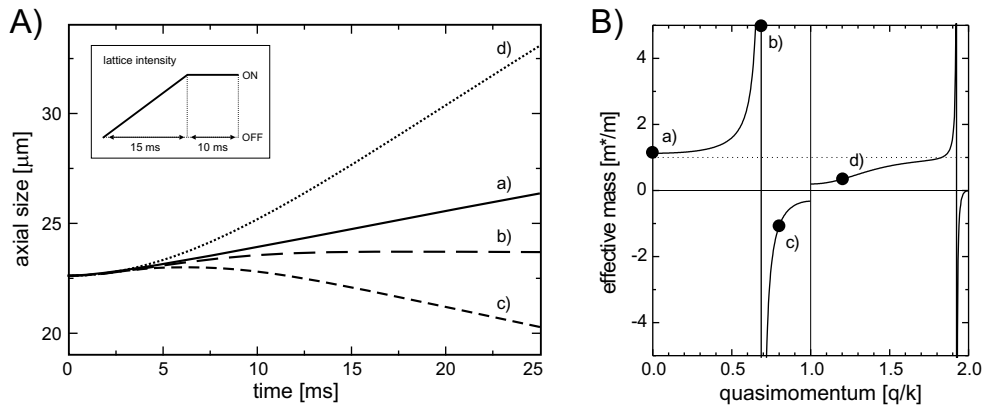

Figure 4.5: A) Expansion of a cigar-shaped condensate in an optical lattice with $s = 2$, as obtained from the solution of the 1D effective model introduced in [102]. The data show the time evolution of the size of the condensate along the lattice direction for different values of the quasimomentum. The origin of the timescale is set to the instant of the trap switching off. B) Effective mass as a function of the quasimomentum for a periodic potential with $s = 2$. The points correspond to the four quasimomentum states considered in A: a) $q = 0$, b) $q = 0.7k$, c) $q = 0.8k$, d) $q = 1.2k$.

mass. This result suggests the possibility to use optical lattices to engineer the dispersion of matter-waves, allowing for a fine control of the wavepacket size. In particular, the realization of a negative effective mass state could allow an expanding wavepacket to invert its outward motion and start compressing along the lattice direction. We note that this effect occurs only if the wavepacket is initially expanding. Actually, as can be easily demonstrated (see for example [100]), the free expansion of a wavepacket initially at rest is not dependent on the sign of the mass. If we consider the Schrödinger equation (4.15), we realize that a change of sign in m^* corresponds to a time-reversed evolution of the system. If the sign of the effective mass is changed when the condensate is at rest, i.e. in a turning point of the dynamics, the subsequent expansion would be the same, regardless of the sign of m^*. Instead, if the wavepacket is initially expanding outward, when the effective mass becomes negative the dynamics is reversed and the focusing effect takes place.

4.2.2 The experiment

The experimental procedure is schematically shown in Fig. 4.6. After producing the condensate we switch off the magnetic confinement and, after 1 ms of expansion of the atomic cloud, we increase the intensity of an optical lattice moving at constant velocity v_L using a linear ramp of 2 ms. We have checked

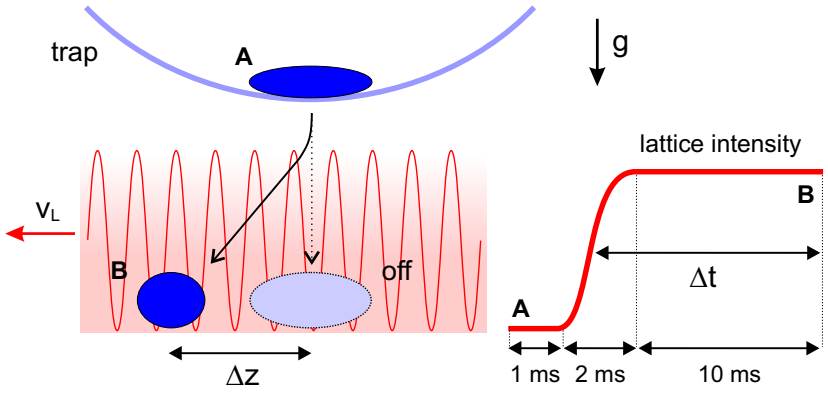

Figure 4.6: Schematics of the experimental procedure. After releasing the condensate from the magnetic trap (A) we adiabatically ramp the intensity of an optical lattice moving at velocity v_L. We let the condensate expand in the periodic potential and after 10 ms at the maximum light intensity we look at the position and shape of the atomic cloud by absorption imaging along the radial horizontal direction (B).

that, for the lattice heights used in the experiment, this time is long enough to ensure an adiabatic loading of the condensate in a single Bloch state (see Sec. 4.1.3). At this time, when the lattice intensity has arrived to the final value, the density of the cloud is reduced from the one in the magnetic trap by a factor ~ 4 and the interaction energy drops to ~ 0.25 of the total release energy [41]. Since the mean field energy has been mostly converted into kinetic energy in this first phase of the expansion, we can expect interactions to play a negligible role in the following dynamics.

The condensate is left expanding for 10 ms in the moving lattice at the maximum intensity, then we image the atomic density distribution looking at the position and the size of the cloud. This interaction time is ultimately limited by the finite size of the lattice beams, since the atoms, not being confined in the vertical direction, are falling under the effect of gravity. At the time of detection, 13 ms after the trap switching off, the atomic cloud has moved along the vertical direction 0.8 mm. The beam waist 3 mm is large enough that we can neglect the variation of intensity in the vertical direction and we can assume that the atoms are moving in a lattice with constant height throughout their fall.

Before presenting the results of the experiment, which will be discussed in detail in the following sections, let us spend some words on the experimental method we have used to verify the above assumption on the spatial variation of the lattice intensity. In order to check this condition we have used the same Bragg scattering technique described in Sec. 3.1.4 for the calibration of the

lattice height, taking advantage of the condensate, falling under the effect of gravity, to probe the lattice intensity at different vertical positions. Differently from the technique described in Sec. 3.1.4, here the BEC expands with zero horizontal velocity and the Bragg resonance condition is met by changing the relative frequency $\Delta\omega$ of the two lattice beams. After different BEC expansion times t_{exp} we flash the two lattice beams detuned by $\Delta\omega = 4\omega_R/2\pi$ (where $\omega_R = \hbar k^2/2m = 2\pi \times 3.77$ kHz is the recoil frequency) in order to induce Bragg transitions between the momentum states $p = 0$ and $p = 2\hbar k$. After a further time of flight, necessary for the two momentum components to spatially separate, we detect via absorption imaging the number of atoms in the two states, in the same way as we do when calibrating the lattice height. The duration Δt of the pulse is chosen in such a way to be in the first half-period of the Rabi oscillation induced in the atomic population

$$N_e = \frac{N}{2}\left[1 - \cos\left(\Omega_B \Delta t\right)\right], \tag{4.16}$$

where N_e is the population in the momentum state $p = 2\hbar k$ and Ω_B is the Rabi frequency, connected to the lattice height s by Eq. (3.23). Substituting Eq. (4.16) in Eq. (3.23) one obtains an expression for the lattice height as a function of the excited population:

$$s = \frac{2}{\omega_R \Delta t} \arccos\left(1 - \frac{2N_e}{N}\right). \tag{4.17}$$

In Fig. 4.7 we plot the lattice height obtained from the measured excited fraction through Eq. (4.17) as a function of the expansion time t_{exp}. This measurement allows us to verify that in the first 13 ms of expansion the lattice height stays almost constant.

This technique can also be used to obtain quantitative information about the spatial beam profile, since the atoms, once released from the trap, probe at different times different regions of the beam. For a TEM-00 Gaussian beam propagating horizontally, the intensity changes in the vertical direction according to the expression

$$I(z) = I_0 e^{-\frac{2(z-z_0)^2}{w^2}}, \tag{4.18}$$

where I_0 is the peak intensity, w is the waist, i.e. the distance from the beam axis at which the intensity drops to $1/e^2$ of the central value, and z_0 is the vertical position of the beam axis with respect to the center of the magnetic trap. The atoms fall according to the law $z(t_{exp}) = g t_{exp}^2/2$, where g is the acceleration of gravity. Hence the time-dependent lattice height they experience, proportional to the beam intensity, is given by

$$s(t_{exp}) = s_0 e^{-\frac{2(g t_{exp}^2/2 - z_0)^2}{w^2}}. \tag{4.19}$$

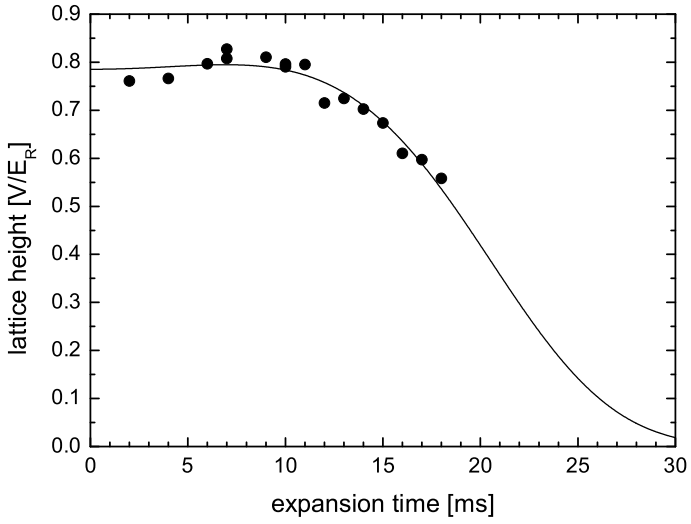

Figure 4.7: Intensity of the optical lattice probed by the atoms, once released from the magnetic trap, as a function of the expansion time t_{exp}. The line is a fit of the experimental points, obtained through a Bragg scattering calibration, with Eq. (4.19) holding for a Gaussian beam profile.

The line in Fig. 4.7 is a fit of the experimental points with Eq. (4.19), giving as best parameters the waist $w = 3.0 \pm 0.2$ mm and the central vertical position $z_0 = 0.26 \pm 0.09$ mm below the magnetic trap center.

4.2.3 Band spectroscopy

Let us come back to the experiment described in Fig. 4.6 on the expansion of the condensate through the moving lattice, first considering the center-of-mass motion. We observe that, when the velocity of the lattice is not zero, the atoms are partially dragged by the lattice in the same direction as $\mathbf{v}_L$. Measuring the displacement Δz with respect to the ordinary expansion we can determine the velocity of propagation of the condensate in the lattice. In the moving frame of the periodic potential this is given by

$$v = \frac{\Delta z}{\Delta t} - v_L, \tag{4.20}$$

where Δt is the time of expansion inside the lattice (Fig. 4.6). In Fig. 4.8A we report the experimental velocities as a function of the quasimomentum for two different lattice heights $s = 1.3(1)$ and $s = 3.8(1)$. Each point is the average of ten measurements and the error bars are calculated taking into account a 1 ms uncertainty in Δt due to the adiabatic ramp on the lattice intensity. This source of systematic uncertainty completely dominates the statistic error.

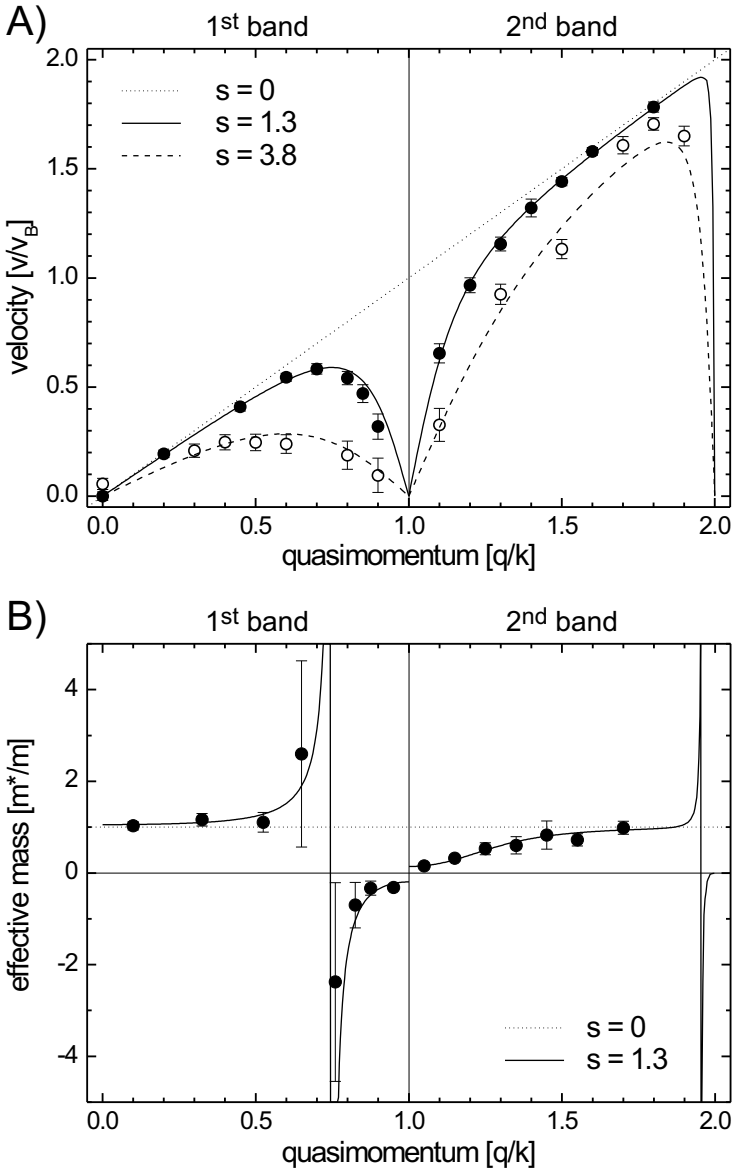

Figure 4.8: A) Velocity of the condensate in the frame of the moving lattice for the lowest two energy bands and two different lattice heights: $s = 1.3$ (filled circles) and $s = 3.8$ (empty circles). The experimental data are obtained from the measured displacements of the condensate center-of-mass after expansion through the lattice. The lines are calculated from band theory. B) Effective mass of the condensate in the lowest two energy bands for $s = 1.3$. The experimental points (filled circles) are obtained by numerically evaluating the incremental ratios $\Delta v/\Delta q$ from the data shown in A). The lines are obtained from a single-particle band theory calculation.

We can now compare the experimental velocities with the group velocity $v_n(q)$ describing the propagation of a Bloch wavepacket (see Sec. 1.2.2). The lines shown in figure 4.8A are obtained calculating the eigenspectrum $E_n(q)$ of the Mathieu equation (1.30) in the first two energy bands and evaluating the Bloch velocities with (1.34). The experimental points show a very good agreement with the velocity spectrum calculated from the Bloch theory for our measured lattice heights with no free parameters. We note that the theoretical curves are derived from the simple one-particle model neglecting the effect of interactions. As a matter of fact, since the experiment is performed in a low density regime, we expect that interactions do not substantially modify the energy spectrum of the system.

Following the Bloch theory, the effective mass in Eq. (1.38) can be rewritten using Eq. (1.34) as

$$m^* = \hbar \left(\frac{\partial v}{\partial q} \right)^{-1} . \tag{4.21}$$

Therefore, a sufficiently dense sampling of the quasimomentum space allows us to obtain an experimental determination of the effective mass by numerically approximating the derivative $\partial v/\partial q$ with the ratio $\Delta v/\Delta q$ of the finite increments between consecutive points. In Fig. 4.8B we report the results of such an analysis on the experimental data for $s = 1.3$ and the corresponding theoretical curve calculated from Eqs. (1.30) and (1.38).

This experimental study allows us to make a precise spectroscopy of the energy bands, measuring the velocity spectrum and the effective mass of the condensate in the periodic potential. The actual limitation of this system is the finite interaction time Δt, which gives an uncertainty on the calculated velocities. Using larger lattice beams could slightly increase the accuracy of the measurement, because of the longer available interaction time. However, the ultimate limit is fixed by the fact that the atoms rapidly escape from the field of view of the imaging setup and eventually reach the bottom of the vacuum cell. The ideal system would be realized by getting rid of the axial trapping while keeping a radial confinement in order to avoid the effect of gravity. This could be done, for instance, letting the condensate expand in a far off resonant optical trap in which the axial confinement is very weak.

4.2.4 Lensing effect

In the above section we have studied the center-of-mass motion of the condensate expanding in the moving lattice. This is not the only information we can get from this experiment. Actually, the most interesting effect concerns the dependence of the shape of the expanded condensate on different lattice velocities (hence different quasimomenta of the condensate in the frame of the moving lattice). In Fig. 4.9A we report absorption images of the expanded condensate for three cases: a) expansion without lattice; b) expansion in a lattice

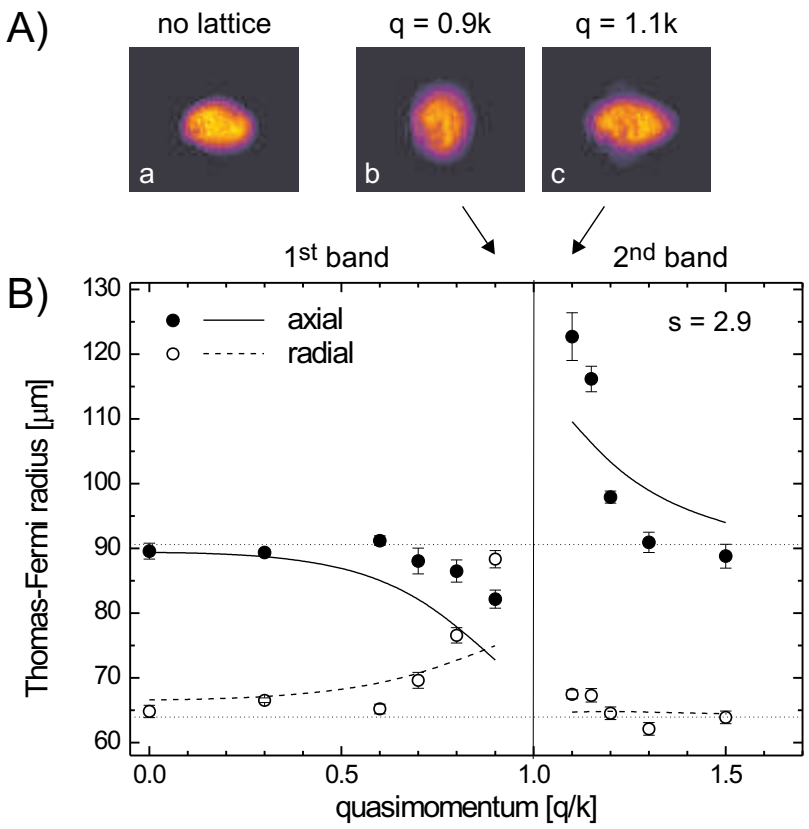

Figure 4.9: A) Absorption images of the expanded condensate, from left to right: a) normal expansion of the condensate without lattice; b) axial compression in a lattice with $s = 2.9$ and $q = 0.9k$ (first band); c) enhanced axial expansion in a lattice with $s = 2.9$ and $q = 1.1k$ (second band). The lattice is oriented from left to right. B) Axial and radial widths of the condensate after an expansion of 10 ms in an optical lattice with $s = 2.9$ as a function of the quasimomentum q in the first two energy bands. The horizontal dotted lines show the widths of the expanded condensate in the absence of the optical lattice. The continuous and dashed lines are calculated with the 1D effective model described in Sec. 4.2.1.

with $s = 2.9$ and $q = 0.9k$ (first band); c) expansion in a lattice with $s = 2.9$ and $q = 1.1k$ (second band). From these images we can clearly observe that the shape of the condensate actually depends on the quasimomentum state. In Fig. 4.9B we report the measured axial and radial sizes of the condensate as obtained from a 2D fit of the density distribution with an inverted parabola Thomas-Fermi profile. The size of the condensate also depends on the number of atoms, since interactions tend to enlarge the trap ground state, hence

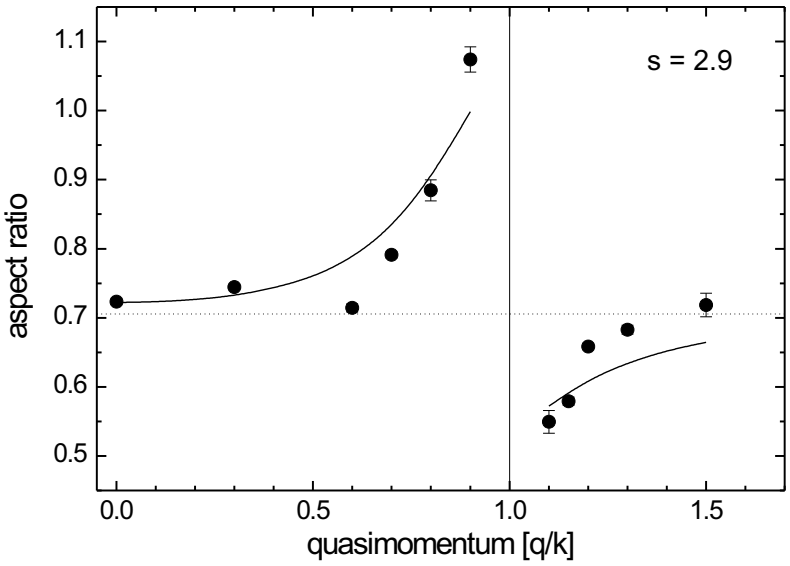

Figure 4.10: Aspect ratio of the condensate after 10 ms of expansion in an optical lattice with $s = 2.9$. The dotted line shows the aspect ratio of the expanded condensate in the absence of the optical lattice. The continuous line is calculated with the 1D effective model presented in Sec. 4.2.1.

an accurate control of this quantity is required not to introduce systematic effects. In our setup, because of fluctuations of the trap bias field, we measure small variations ($\sim 20\%$) of the number of atoms for different realizations of the condensate. In order to compensate for this effect, we have scaled the measured radii to an average number of atoms using the relation $R \propto N^{1/5}$ valid in the Thomas-Fermi limit [41]. Each data point in Fig. 4.9B corresponds to an average of 10 repeated measurements analyzed with this method.

We note that, approaching the boundary of the first Brillouin zone for $q \lesssim k$, the axial size of the condensate gets smaller as a consequence of the modified effective mass $m^* < 0$ (see Fig. 4.9A,b). This focusing effect along the axial direction is balanced by an increased expansion along the radial axis. This can be explained considering that, because of the compression along the lattice direction, the fast radial expansion is further enhanced by the increase of the residual mean-field energy. Instead, when the condensate is loaded in the second band, for $q \gtrsim k$, the axial expansion is enhanced due to the strong positive curvature of the second energy band near the zone boundary, where $0 < m^* < m$ (see Fig. 4.9A,c). As one would expect, in this case the radial dynamics is not modified, since the residual mean-field energy is further reduced by the increased axial expansion, causing a suppression of the non-linear coupling between the axial and radial dynamics. In Fig. 4.10

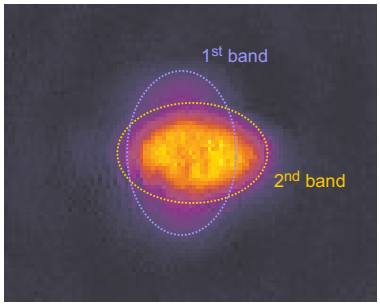

Figure 4.11: Non-adiabatic loading of a condensate in a lattice with velocity $v_L = 1.1v_B$ and height $s = 2.9$. In this picture, showing the atomic density distribution after an expansion of 10 ms in the lattice, we distinguish the presence of two clouds with different shapes resulting from the population of different energy bands corresponding to different effective masses.

we also show the aspect ratio (defined as the ratio between the radial and the axial size), which is characterized by a marked discontinuity across the boundary between the first and the second zone. The aspect ratio does not depend on the number of atoms in the condensate (differently from the axial and radial widths considered separately), hence possible systematic effects due to fluctuations in this quantity are avoided.

To get further insight on the behavior of the condensate during the expansion, we have compared the experimental results with the predictions of the 1D effective model introduced in [102]. Actually, the lines in Fig. 4.9B show that the model qualitatively reproduces the behavior observed in the experiment, even though it does not fit precisely the data. In particular, approaching the first zone boundary, the observed focusing effect along the axial direction is slightly smaller than the calculated one, and at the same time the expansion along the radial direction (not directly affected by the lattice) is enhanced. Instead, in the second band the radial behavior is well reproduced by the model, whereas there is still a discrepancy concerning the axial expansion.

We remark that in the region near the band edge ($0.95k < q < 1.05k$) the 2 ms ramp is not sufficiently long to ensure an adiabatic loading of the BEC in the optical lattice, and the description of the system is complicated by the fact that more than one energy band gets populated. Indeed what we actually see in the experiment is a superposition of two atomic clouds with different shapes resulting from the minor population of a different energy band. A typical example of a partial non-adiabatic loading is shown in Fig. 4.11, referring to an initial lattice velocity $v_L = 1.1v_B$. In this image (1 ms ramp time) one can clearly distinguish a high density cloud, elongated in the horizontal direction and corresponding to $q = 1.1k$ in the second band, and a lower density cloud,

extending mostly in the vertical direction and corresponding to $q = 1.1k$ in the first band [2].

In conclusion, we have studied the effect of a moving optical lattice on the expansion of a Bose-Einstein condensate, explaining the observed focusing effect in terms of a modified dispersion induced by a change in the effective mass. This suggests the possibility of using optical lattices as lenses for matter waves. Tuning the velocity of the lattice it is indeed possible to set the "focal length" of the periodic potential, changing the lensing power all the way from focusing to defocusing of the atomic cloud. The interaction of cold atoms with coherent light has been extensively used in the field of atom optics for the implementation of the matter wave equivalents of many components commonly used in ordinary optics [105, 106]: atomic mirrors and beam splitters (using Bragg scattering [3]) as well as matter wave amplifiers (using superradiant Rayleigh scattering [107, 108]). With this experiment we suggest the possibility to use optical lattices to manage the shape (dispersion) of matter waves, thus extending the rich field of application of optical lattices to create new devices in the atom-optician toolkit.

Similar results regarding the control of the matter wave dispersion have been obtained almost at the same time also in the group of M. Oberthaler in Konstanz [109]. In particular, a similar technique has been used in the same group to recently achieve the experimental realization of bright gap solitons [110]. This type of solitonic propagation, analogous to the one existing for condensates with attractive interactions [111, 112], can be obtained under appropriate conditions in a condensate with repulsive interactions in the presence of a periodic potential. Bright gap solitons are generated at the border of the Brillouin zone, when the anomalous dispersion term induced by the negative effective mass exactly cancels the nonlinear interaction term in the Gross-Pitaevskii equation. When these conditions are satisfied, the wavepacket behaves as a solitary wave and propagates in space without spreading.

4.3 Unstable regimes for a BEC in a moving lattice

4.3.1 Introduction

When the interactions among the atoms forming the condensate become important, the simple Bloch picture is complicated by the emergence of new effects connected with the nonlinearity of the Gross-Pitaevskii equation. From a fundamental point view, one interesting problem is related to the stability of the Bloch states. In the last years this problem has been addressed experimentally [30, 113, 114] and in many theoretical papers [8, 49, 50, 83, 84, 94, 95, 96, 97, 115, 116], which have evidenced how the superfluid properties

[2] Because the band spectrum is symmetric for transformations $q \to -q$ and $q \to q + 2nk$, this state is equivalent to $q = 0.9k$ shown in Fig. 4.9A.

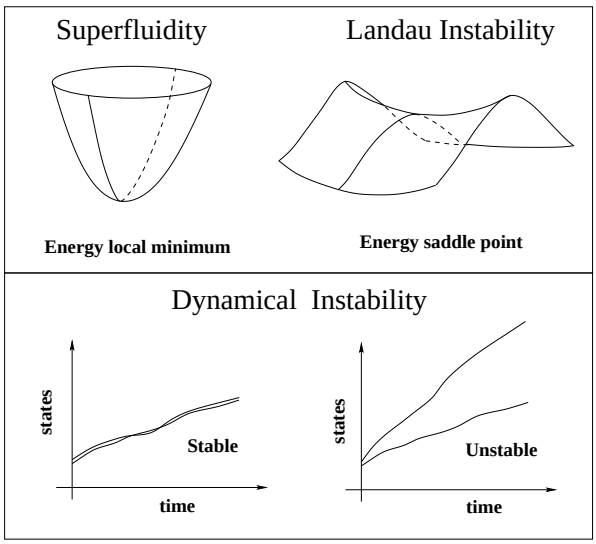

Figure 4.12: Sketch of energetic and dynamical instability taken from [49]. Energetic (Landau) instability is connected with the existence of energy saddle points in the configuration space. Dynamical instability is caused by the existence of perturbations exponentially growing in time.

of a BEC with repulsive interactions in a periodic potential can be affected by two main mechanisms: an *energetic* instability and a *dynamic* instability. The difference between the two processes is pictorially sketched in Fig. 4.12, taken from [49]. While energetic instability is a static property, referring to the existence of energy saddle points in the configuration space, dynamical instability comes from the equation of motion of the system, and is connected with the existence of perturbations which may grow exponentially in time. As we will study, both these processes lead to a depletion of the initial state, but the underlying physical mechanisms are quite different. We will review in this section the basic notions of the standard approach developed in [49, 50, 97] to the study of these instabilities.

Energetic instability. Let us first consider the case of energetic instability. We assume that the condensate is in a Bloch state $\phi_0(x)$ solution of the time-independent Gross-Pitaevskii equation

$$\left[-\frac{\hbar^2}{2m}\nabla^2 + V(\mathbf{r}) + g|\phi_0|^2\right]\phi_0 = \mu\phi_0, \tag{4.22}$$

where $V(\mathbf{r})$ includes the periodic potential and any additional confinement. One can easily demonstrate that solutions of Eq. (4.22) can be calculated

with a variational method, by requiring the energy functional

$$E[\phi] = \int d\mathbf{r} \;\; \phi^* \left[-\frac{\hbar^2}{2m}\nabla^2 + V(\mathbf{r}) - \mu + \frac{g}{2}|\phi|^2 \right] \phi \tag{4.23}$$

to be stationary in the configuration space, i.e. that small variations around a solution ϕ_0 lead to null first order corrections in Eq. (4.23). We indicate a deviation from this stationary solution with

$$\phi(x) = \phi_0(x) + \delta\phi(x). \tag{4.24}$$

Expanding the energy functional (4.23) to the second order in $\delta\phi$ we obtain

$$E[\phi] = E[\phi_0] + \int d\mathbf{r} \;\; \delta\Phi^\dagger \hat{M} \delta\Phi, \tag{4.25}$$

where we have defined the perturbation vector

$$\delta\Phi = \begin{pmatrix} \delta\phi \\ \delta\phi^* \end{pmatrix} \tag{4.26}$$

and the matrix operator

$$\hat{M} = \begin{pmatrix} -\frac{\hbar^2}{2m}\nabla^2 + V - \mu + 2g|\phi_0|^2 & g\phi_0^2 \\ g\phi_0^{*2} & -\frac{\hbar^2}{2m}\nabla^2 + V - \mu + 2g|\phi_0|^2 \end{pmatrix}. \tag{4.27}$$

The first order term in the expansion (4.25) is missing because ϕ_0 is a stationary point of the energy functional. The sign of the second order term, which defines the nature of this point, is given by the spectrum of the operator $\hat{M}$. We note that $\hat{M}$ is hermitian, hence it admits only real eigenvalues. The system will be *energetically stable* if the operator $\hat{M}$ has only positive eigenvalues and thus the energy functional has a local minimum in ϕ_0. If the operator $\hat{M}$ has some negative eigenvalues, the system is no longer in a local energy minimum. In this case the system is *energetically unstable*, in the sense that some directions in the space spanned by $\delta\phi$ exist along which it can decrease its energy. This is a dissipative process and cannot be described by the GPE, which is a conservative equation. If the system moves towards lower energy states, the energy in excess must be transferred to some external degrees of freedom, hence energetic instability can take place only in the presence of some external disturbance providing the mechanism for dissipation.

Energetic instability is a general characteristic of superfluids. It can be demonstrated [49, 50] that, in the absence of periodicity, the above definition of energetic stability reduces to the well known Landau criterion for superfluidity, stating that the superfluid flow can be maintained only for velocities smaller than the sound velocity in the superfluid medium. When the velocity of the quantum fluid (with respect to some impurities) exceeds this value, the system can lower its energy by emitting elementary phonon-like excitations, thus destroying the superfluid flow. For this reason this kind of instability is also called *Landau instability*.

Dynamical instability. Let us now consider the case of dynamical instability. To explore this mechanism we need to examine the time-dependent Gross-Pitaevskii equation

$$i\hbar\frac{\partial\psi}{\partial t} = \left[-\frac{\hbar^2}{2m}\nabla^2 + V(\mathbf{r}) + g|\psi|^2\right]\psi \tag{4.28}$$

Again, we consider a perturbation of the state $\psi_0(x,t) = e^{-i\mu t/\hbar}\phi_0(x)$, that can be written in the same fashion as before in the form:

$$\psi(x,t) = e^{-i\mu t/\hbar}\left[\phi_0(x) + \delta\phi(x,t)\right] \tag{4.29}$$

Substituting Eq. (4.29) in Eq. (4.28) one obtains the following linearized equation of motion

$$i\hbar\frac{\partial\delta\Phi}{\partial t} = \hat{\sigma}_z\hat{M}\delta\Phi \tag{4.30}$$

where $\hat{\sigma}_z$ is the Pauli matrix

$$\hat{\sigma}_z = \begin{pmatrix} 1 & 0 \\ 0 & -1 \end{pmatrix}. \tag{4.31}$$

The time evolution of the perturbation $\delta\phi(x,t)$ is described by the operator $\hat{\sigma}_z\hat{M}$. Differently from $\hat{M}$, this operator is non hermitian, hence it admits complex eigenvalues. Let us consider the case in which the operator $\hat{\sigma}_z\hat{M}$ has an eigenstate $\delta\Phi_\omega$ with complex eigenvalue $\hbar\omega = \hbar(\omega_r + i\omega_i)$. According to Eq. (4.30) the evolution of this state will be described by the equation

$$i\hbar\frac{\partial\delta\Phi_\omega}{\partial t} = \hbar(\omega_r + i\omega_i)\delta\Phi_\omega, \tag{4.32}$$

that, once integrated, gives the solution

$$\delta\Phi_\omega(x,t) = \delta\Phi_\omega(x,0)e^{\omega_i t}e^{-i\omega_r t} \tag{4.33}$$

which is a perturbation exponentially growing in time with rate ω_i. This exponential growth of excitations on top of the unperturbed state ψ_0, occurring when $\hat{\sigma}_z\hat{M}$ has complex eigenvalues, is called *dynamical instability*.

Dynamical instability is a distinctive feature of nonlinear periodic systems. It does not exist either for noninteracting particles in a periodic potential or for a BEC (with repulsive interactions) in free space. However, it is not an exclusive property of interacting Bose-Einstein condensates in optical lattices. As a matter of fact, phenomena related to this kind of instability (also called *modulational instability*) appear in many different contexts, from fluid dynamics and nonlinear optics to plasma physics.

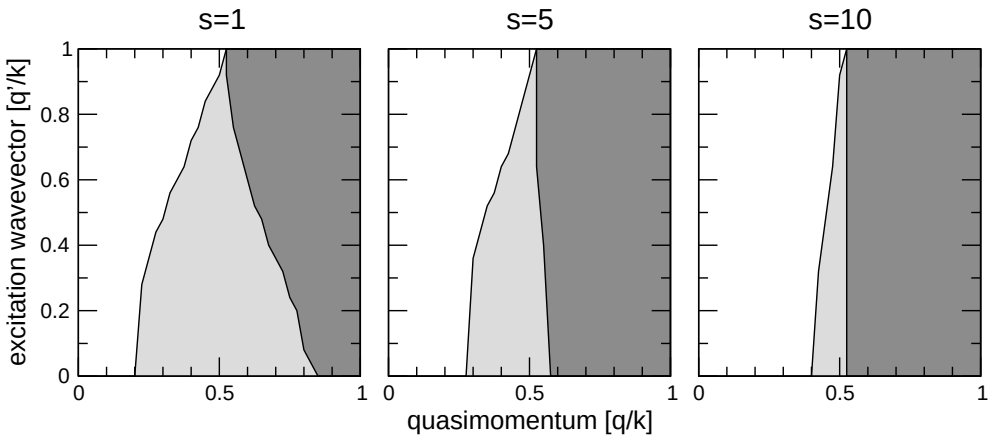

Figure 4.13: Stability diagrams for a BEC with repulsive interactions in a 1D periodic potential obtained from the analysis of the 3D Gross-Pitaevskii equation (adapted from [97]). Shaded areas represent the regions where the system is dynamically unstable (dark) and energetically unstable (both light and dark), while the white areas denote regions of stability. These diagrams are calculated for $k = 2\pi/(800\text{ nm})$, an interaction strength $g|\psi^2| \approx 0.2E_R$ and three lattice heights $s = 1$, $s = 5$, and $s = 10$.

Stability diagrams. One of the most common approaches in this perturbative analysis consists of studying the stability of the Gross-Pitaevskii equation as a function of the condensate quasimomentum and of the excitation wavevector. Let us consider deviations in the condensate wavefunction of the form $\delta\phi = (u_{q'}e^{iq'x} + v^*_{q'}e^{-iq'x})$, where q' is the wavevector of the perturbation. The study of the spectral properties of the operators $\hat{M}$ and $\hat{\sigma}_z\hat{M}$ allows us to trace stability plots like the ones reported in Fig. 4.13. In these diagrams, calculated in [97] for an infinite cylindrical BEC in a 1D periodic potential, the stability of the system is plotted for the lowest Bloch band as a function of the quasimomentum q and the perturbation wavevector q'. From diagrams of this kind [8], we can extract some general information:

1. If the system is homogeneous along the lattice direction, both energetic and dynamical instability are *threshold processes*, since they appear only for quasimomenta larger than a critical value dependent both on the lattice height and the strength of nonlinearities.

2. The dynamically unstable region is always included in the energetically unstable region. As a general result, dynamical instability implies energetic instability [49]. On the other hand, energetically unstable states are not necessarily dynamically unstable.

3. While the threshold for energetic instability can lie at very small quasi-momenta (and even approach $q = 0$ for vanishing nonlinearities), the threshold for dynamical instability has a lower bound fixed at $q = 0.5k$.

Even if the threshold conditions for energetic and dynamical instability can be precisely calculated in the frame of the Gross-Pitaevskii theory, a complete theoretical description of the system after entering the unstable regimes is quite complex. In the case of energetic instability we expect that the system, not being in a local minimum of the energy, should move somehow towards lower energy states. However, the evolution of the system after the onset of this instability cannot be accounted for by the same Gross-Pitaevskii model, which describes a Hamiltonian system and thus includes energy conservation. On the contrary, dynamical instability can be entirely described by the time-dependent Gross-Pitaevskii equation, i.e. the evolution of the system after the onset of the instability can still be calculated solving Eq. (4.28). In particular, it is possible to precisely calculate the growth rates of the unstable modes [8, 97]. However, out of the linear regime, when the excitations are not just weak perturbations of the initial state, the exponential growth of unstable modes could drive the system outside the limits of validity of the Gross-Pitaevskii theory.

Experimental investigation. Although the distinction of these two mechanisms is straightforward from the theoretical point of view, in the experiments it is much more difficult to separate energetic and dynamical instability. As a general comment, no matter which is the mechanism responsible for the onset of instability, we expect the original BEC superfluidity to be compromised and losses of atoms from the ground state to be detected. The experimental technique used in Sec. 3.3 and in the very first experiments devoted to the study of these regimes [113], namely the excitation of dipole oscillations in a harmonic + periodic potential, cannot be used to really separate the effects of energetic and dynamical instability. This happens because, while performing dipole oscillations, the condensate quasimomentum evolves throughout the first band and thus explores both regimes, as indicated in Fig. 4.13. A more detailed investigation of the unstable regimes could provide important information on the distinction between these two mechanisms, a problem that in the past years has attracted a large interest. In this context, the phenomena observed in [113] were attributed to energetic instability mainly because the 1D Gross-Pitaevskii theory used to analyze the data could not reproduce some of the observed experimental features. This in turn suggested that finite temperature effects connected with the activation of energetic instability could play a role. This interpretation lead to a debate [113] and finally in [97], by making a comparison with the full 3D theory, it was shown that the density profiles observed in [113] could be attributed to dynamical instability.

In the following sections we show how the precise control of the BEC quasimomentum, obtained with an optical lattice moving at constant velocity, is crucial to distinguish the different instabilities. We have chosen to investigate the regime of low lattice heights, since in this condition the regions of energetic and dynamical instability are much more separated, as evidenced in the stability plots in Fig. 4.13.

4.3.2 The experiment

The instabilities described in the previous section are connected with the presence of the nonlinear term in the Gross-Pitaevskii equation, arising from the interactions among the atoms forming the condensate. If we want to experimentally investigate these unstable regimes, in order to make this term relevant for the evolution of the system, we need a high density atomic sample. For this reason, instead of investigating the BEC during its expansion (as in the experiment described in Sec. 4.2), we study the time evolution of a magnetically trapped condensate interacting with the moving optical lattice. Similarly to the experiment described in Sec. 4.2, the possibility to control the lattice velocity allows us to accurately set the quasimomentum of the condensate and to make a precise investigation of the stability regimes in the full Brillouin zone and for different energy bands.

The experimental procedure is the following. First we produce the BEC in the magnetic trap, then we adiabatically switch on the moving optical lattice in order to load the condensate in a state with well defined quasimomentum q and band index n. We let the BEC evolve in this potential for a variable time Δt, then we switch off both the magnetic trap and the optical lattice and, after an expansion of 28 ms, we image the atomic cloud along the radial horizontal direction. In this experiment the Ti:Sa laser producing the optical lattice operates at $\lambda = 820$ nm, far detuned with respect to the Rb D1 line at $\lambda = 795$ nm. The lattice beams are aligned along the symmetry axis of the condensate and are only slightly focused (400 μm diameter), so that the optical radial confinement may be completely neglected.

In order to quantify the effect of the instabilities, we study the decay of the number of atoms in the condensate as a function of the time Δt spent in the periodic potential. To this aim it is important to control and reduce all the other spurious effects that can limit the BEC lifetime. In Sec. (4.1.2) we have discussed in detail how the presence of a stationary optical lattice may induce heating and atom losses in the BEC. In particular, the presence of a residual thermal component, whatever is the mechanism responsible for its creation, may seriously decrease the lifetime. For this reason we use an RF-shield in order to keep the temperature constant by removing the hottest atoms from the atomic sample. In this way we measure lifetimes of the order of ≈ 10 s in the optical lattice at $v_L = 0$, with no discernable thermal fraction even on long timescales.

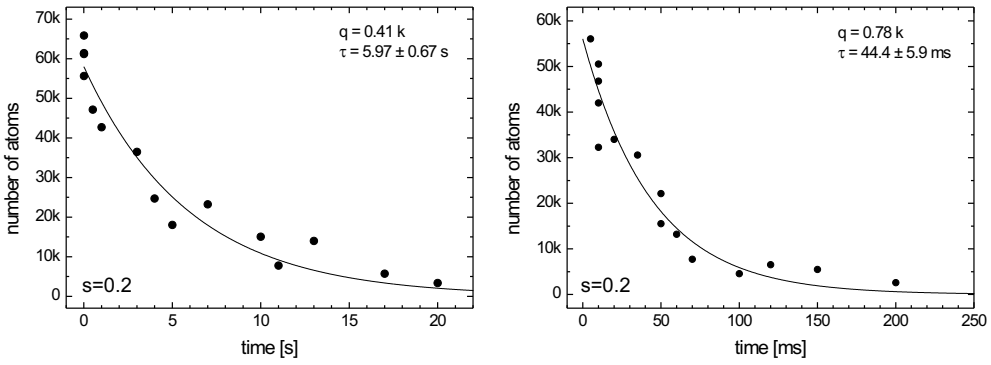

Figure 4.14: Decay of the number of atoms in a magnetically trapped BEC loaded in a 1D moving optical lattice with $s = 0.2$. The graphs refer to two different quasimomentum states $q = 0.41k$ (left) and $q = 0.78k$ (right), below and above the calculated threshold for dynamical instability. The lines are fit of the experimental points with an exponential decay. The lifetime τ obtained from the fit turns out to be strongly dependent on q.

4.3.3 Dynamical instability

Increasing the lattice velocity, hence the quasimomentum of the condensate, we observe that the decay of the number of atoms is still well described by an exponential function $N(\Delta t) = N_0 e^{-\Delta t/\tau}$, as shown in Fig. (4.14). From the fit of the experimental data with such a function we extract a characteristic lifetime τ, which turns out to be a function of the quasimomentum state. In Fig. 4.15 we plot the loss rate $1/\tau$ as a function of the quasimomentum q for a lattice height $s = 0.2$. With increasing q, from the bottom of the first band to the zone boundary, the lifetime changes dramatically, spanning three orders of magnitude from ≈ 10 s to ≈ 10 ms. In particular, we observe a sudden increase of the loss rate around $q = 0.55k$, in good correspondence with the threshold for dynamical instability calculated with this lattice height and the measured BEC peak density $n \simeq 10^{14}$ cm^{-3} (vertical line) [32].

The theoretical threshold for the onset of dynamical instability is obtained from a linear stability analysis of the Non-Polynomial Schrödinger Equation (NPSE) [98, 99]. This 1D equation, much easier to solve than the full 3D GPE, takes into account the transverse dynamics with an effective radial-to-axial coupling, and provides a more realistic description of the system with respect to the simple 1D GPE used in previous works [8]. It has been verified that, for the range of lattice heights we have considered, the instability thresholds and the growth rates of the unstable modes obtained from the NPSE are in good agreement with the results of the full 3D GPE [97].

As we have discussed in the previous sections, our experimental procedure allows us to load the condensate not only in the lowest band, but also in excited

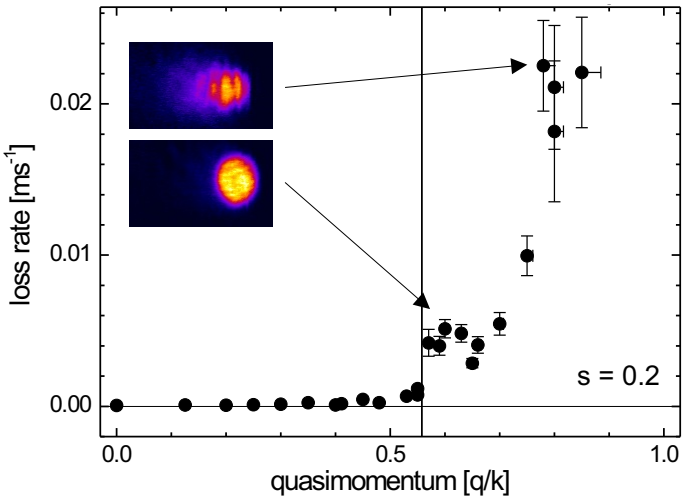

Figure 4.15: Loss rates for a trapped BEC loaded in a moving optical lattice with $s = 0.2$. The vertical line corresponds to the calculated threshold for the onset of dynamical instability [97]. The images show the density distribution of the expanded cloud. Near the zone boundary, where instability is faster, we observe the appearance of some complex structures, evidencing the loss of coherence in the BEC. The lattice is directed from right to left.

bands. The study of the system in these regions of the energy spectrum offers precious information on the observed phenomena and is particularly important for a clear interpretation of the experimental results. In Fig. 4.16A we extend the loss rates measurements for $s = 0.2$ to the lowest three energy bands. After entering the second band, the loss rate starts to decrease with increasing q, in a quite symmetric way with respect to the first band, with the exception of the threshold behavior near $q = 0.55k$, which we do not observe in the second band. In the third band, eventually, we do not detect any peculiar feature and the measured lifetimes approach the value for the stationary lattice. This behavior can be explained considering the fact that, for this small lattice height, only the very lowest bands significantly differ from the free energy spectrum. For higher energies one therefore expects to recover the free condensate behavior. With similar considerations, we can expect that increasing the lattice height the observed depletion of the condensate should be even more dramatic. As a matter of fact, increasing the height of the optical lattice from $s = 0.2$ to $s = 1.15$, as shown in Fig. 4.16C, the measured loss rates get larger and strong losses appear in the full second and third bands. In particular, we note that the picture in the higher bands starts to develop asymmetric features around the zone edges. This is particularly evident entering the second band, where the loss rate has a local maximum as a function of the quasimomentum, and

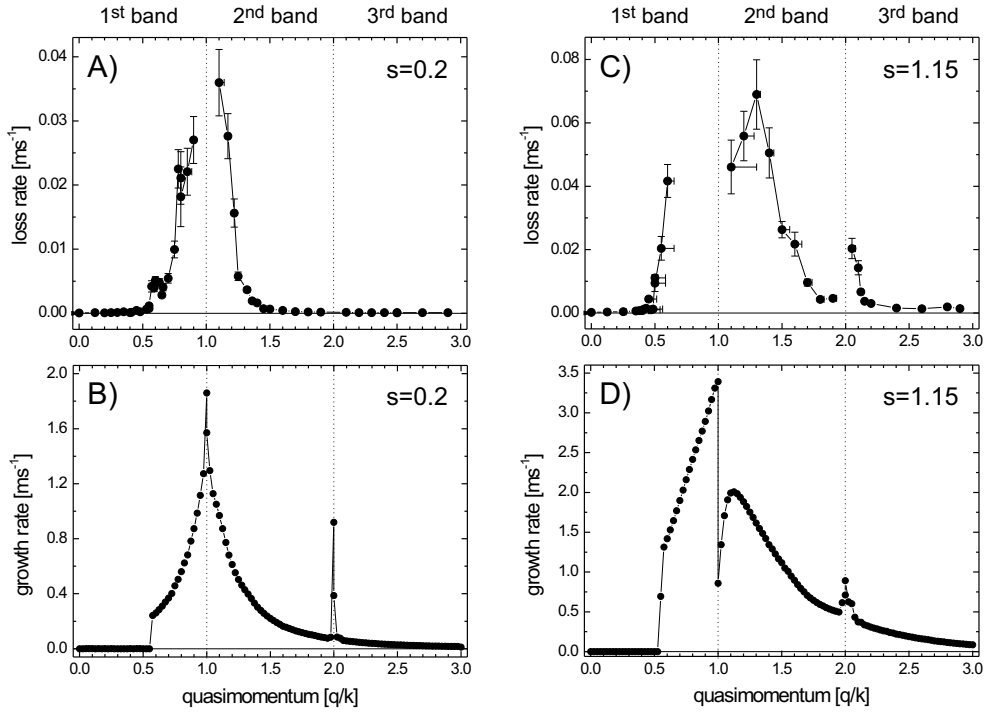

Figure 4.16: Top) Experimental loss rates for a BEC loaded in a moving lattice with $s = 0.2$ (A) and $s = 1.15$ (C). Bottom) Theoretical growth rates of the most dynamically unstable modes obtained from a linear stability analysis of the NPSE [97] for the same lattice heights $s = 0.2$ (B) and $s = 1.15$ (D).

crossing the boundary between the second and the third Brillouin zone, where we observe a marked change in the instability rates.

In order to validate our interpretation of these results in terms of dynamical instability, we have compared the measured loss rates with the growth rates of the unstable modes calculated with a linear stability analysis of the NPSE [97]. Since the range of unstable modes that can be excited for a fixed quasimomentum q can be very large, we have chosen to consider only the growth rate of the most unstable mode, i.e. the excitation whose frequency has the biggest imaginary part, hence the faster evolution in time. Comparing the experimental graphs (A,C) of Fig. 4.16 with the corresponding theoretical graphs (B,D), we observe the same distinctive shapes. This remarkable agreement between theory and experiment enforces our interpretation that the observed change in the BEC lifetime is indeed due to dynamical instability. The experimental loss rates, however, should not be quantitatively compared with the theoretical growth rates, since these two quantities have different physical meanings: the first measures how fast the atoms are removed from

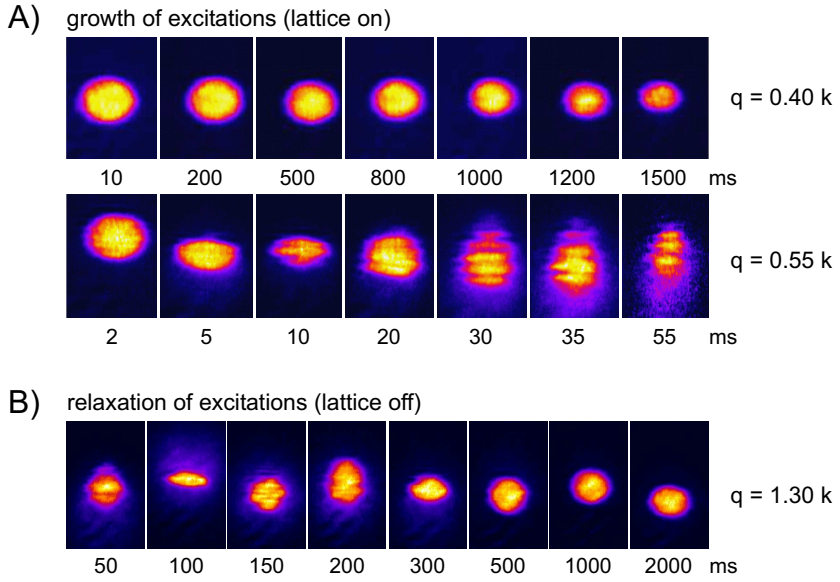

Figure 4.17: A) Expanded atomic density profile for different times spent by the BEC in a lattice with $s = 1.15$. The images correspond to the quasimomentum values $q = 0.4k$ and $q = 0.55k$, respectively below and above the threshold for dynamical instability. Note the different timescales. B) Expanded atomic density profile for different times spent by the BEC in the pure magnetic trap after 5 ms spent in an optical lattice with $s = 1.15$ and $q = 1.30k$ (sufficient to induce a strong modulation in the density). In all these pictures the lattice is directed from top to bottom.

the condensate; the second is the rate at which the unstable modes grow in the linear regime, i.e. at the onset of the instability. Out of the linear regime, when excitations have grown and the unstable modes are not just weak perturbations of the carrier Bloch wave, the dynamical evolution of the system cannot be explained with this perturbative approach and a different theoretical analysis is required. However, the remarkable similarity between the experimental and theoretical curves indicates that the onset of the instability produces a significant imprinting on the subsequent dynamics of the system.

Deeply in the dynamically unstable regime (as shown in the pictures of Fig. 4.15) we observe the appearance of complex structures in the expanded BEC density profile, suggesting the ongoing fragmentation of the Bloch wave. These interference-like structures are more evident for larger lattice heights and near the zone boundaries, where the evolution of instability is faster. In Fig. 4.17A we present two sequences of images showing the time evolution of the expanded density distribution for a lattice height $s = 1.15$ and two values of quasimomentum below and above the threshold for dynamical instability.

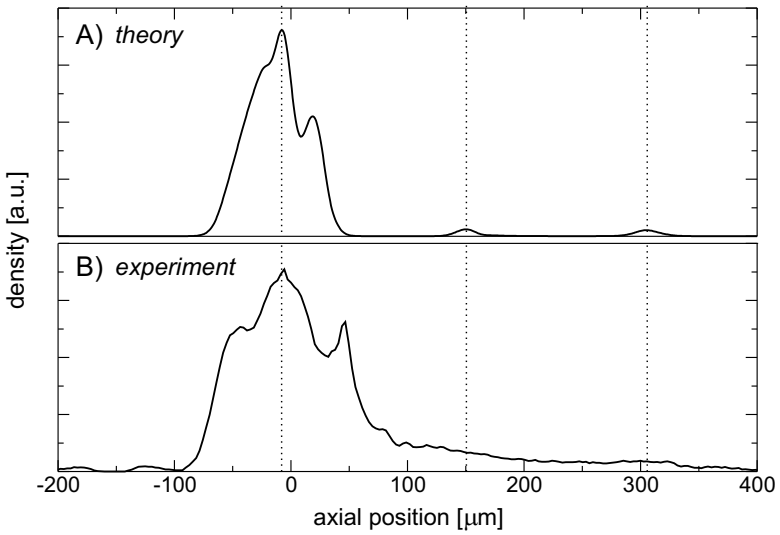

Figure 4.18: Axial cross sections of the density distribution after 50 ms of interaction with the lattice and 28 ms of free expansion. A) Numerical solution of the 3D Gross-Pitaevskii equation assuming ballistic expansion of the calculated momentum distribution. B) Measured density distribution. In both cases the lattice height is $s = 1.15$, the quasimomentum is $q = 0.55k$ (in the dynamically unstable region), and the lattice is switched off ramping down the intensity in 2 ms. The vertical lines mark the main peaks of the calculated momentum distribution, corresponding respectively to 0, $1.01k$ and $2k$. In both cases the lattice is moving from left to right.

This behavior may reflect the creation of phase domains induced by the growth of instabilities, which break the phase uniformity of the BEC. When these structures are not just weak perturbations of the ground state density profile, the number of atoms in the condensate cannot be measured with a Thomas-Fermi fit of the column density. In order to measure the number of atoms more precisely, we let the atomic cloud evolve for 1 s in the pure magnetic trap, allowing relaxation of the excitations. We have measured typical relaxation times of the order of $\approx$ 500 ms, after which the BEC recovers its smooth density profile, as shown in Fig. 4.17B. This observation suggests the existence of mechanisms that, once the lattice is switched off and the cause of instability is removed, allow the system to come back to the ground state, damping the excitations and restoring the coherence. We have verified that this relaxation occurs also in the absence of the RF-shield and with the same timescale.

In order to get further insight into the nature of these structures, we compare the experimental observations with the numerical solution of the full 3D Gross-Pitaevskii equation [33]. This comparison is shown in Fig. 4.18,

where we plot the theoretical and experimental axial cross sections of the expanded density distribution for a lattice height $s = 1.15$ and a quasimomentum $q = 0.55k$, in the dynamically unstable region. In this case the ramp time is 10 ms, the interaction time is $\Delta t = 50$ ms, while the expansion time is $t_{exp} = 28$ ms. The curve in (A) is obtained by numerically solving the full 3D GPE for these parameters and evaluating the expanded density profile by assuming ballistic expansion of the calculated momentum distribution. The curve in (B) shows the experimental density profile measured for the same parameters. From the comparison of the two curves we note that the simulation well reproduces the structure of the central peak observed in the experiment. This long-wavelength modulation of the density is a consequence of the nonlinear processes taking place after the initial growth of the unstable modes. As a matter of fact, the simulation shows that for shorter times ($\Delta t \approx 10$ ms for these parameters) the momentum distribution is characterized by the emergence of peaks corresponding to the most dynamically unstable modes that start to grow (seeded by numerical noise). Afterwards, when the amplitude of these components becomes macroscopic ($\Delta t \approx 40$ ms for these parameters), the nonlinear dynamics introduce processes of mode-mixing and the momentum distribution gets quite complicated [33].

However, the naive expectation that the expanded density profile of the condensate would simply reflect the structure of the momentum spectrum could not be correct. We note that the occurrence of dynamical instability may lead to a rapid population of the non-condensed (thermal) fraction, that is not included in the Gross-Pitaevskii approach. In order to account for this mechanism one should include in the theory also the interaction between the condensate and the non-condensed fraction. In the experiment the formation of a thermal component (which could not be efficiently removed by the RF-shield on this fast timescales) could affect the expanded density distribution masking the momentum peaks populated by the interaction with the lattice (indicated by the vertical dotted lines at 150 μm and 305 μm in figure). Actually the experimental density profile reported in Fig. 4.18B shows a low-density tail on the right side of the main peak, that is compatible with a small thermal fraction dragged away by the lattice (moving in figure from left to right).

4.3.4 Energetic instability

The experiment described in the previous section has been performed with quasi-pure condensates, i.e. ultracold samples where the non-condensed component is not detectable. In this condition the system is well described by the Gross-Pitaevskii theory, which is strictly valid only at zero temperature. In order to investigate finite-temperature effects, we have repeated the same experiment in the presence of a non-vanishing thermal fraction. The temperature of the sample can be easily controlled by varying the frequency of the RF-shield slightly below the critical value for Bose-Einstein condensation.

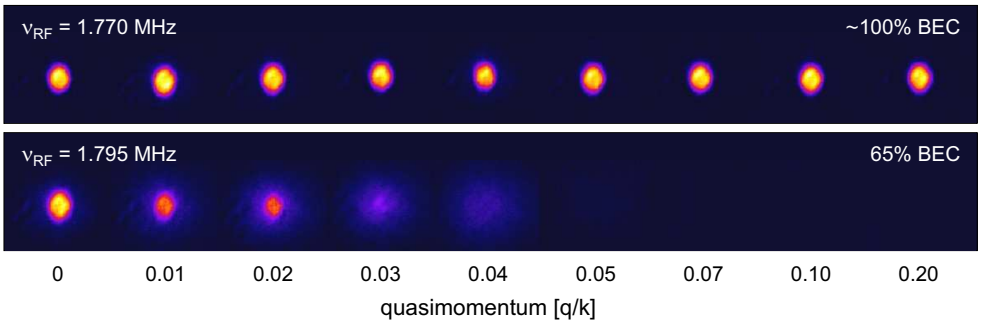

Figure 4.19: Expanded density distribution of the atomic sample after 15 s spent in a moving optical lattice with $s = 0.2$ for different values of the BEC quasimomentum. The pictures in the upper row refer to a pure BEC, the ones in the lower row to a 65% condensed cloud.

From the images of Fig. 4.19 one can get a first indication that in the presence of a thermal component the system behaves differently. In the figure we report the expanded density distribution of the atomic sample following 15 s spent in an optical lattice with $s = 0.2$ for different lattice velocities (hence BEC quasimomenta). The pictures in the upper row refer to an almost pure condensate, while the lower row shows the behavior of a $\sim 65\%$ condensed cloud. While the pure condensate seems to be unaffected by the moving lattice, in the case of a mixed cloud even a small lattice velocity induces strong losses and heating, in such a way that for $q = 0.04k$ no atoms remain in the condensed part. We note that the range of quasimomenta shown in figure is well below the threshold for dynamical instability.

This behavior, triggered by the presence of a thermal component, can be attributed to the onset of energetic instability. As we have introduced in Sec. 4.3.1, energetic instability is a mechanism peculiar to the physics of superfluids and takes place when the velocity of the superfluid (with respect to some impurities) is higher than the sound velocity inside the superfluid medium. When this condition is satisfied, the superfluid ground state ceases to be the lowest energy state and the system can lower its energy by emitting elementary (phonon-like) excitations, which deplete the original ground state. In the case of an ultracold atomic gas, this mechanism applies only to the Bose-condensed component, which behaves as a superfluid, and not to the thermal part, which behaves as an ordinary fluid. However, in order to be activated, energetic instability requires the presence of a mechanism for dissipation, that can be provided by the presence of a thermal component. The thermal fraction, behaving as a reservoir of excitations, can provide a mechanism for the BEC to lower its energy, thus triggering the onset of energetic instability.

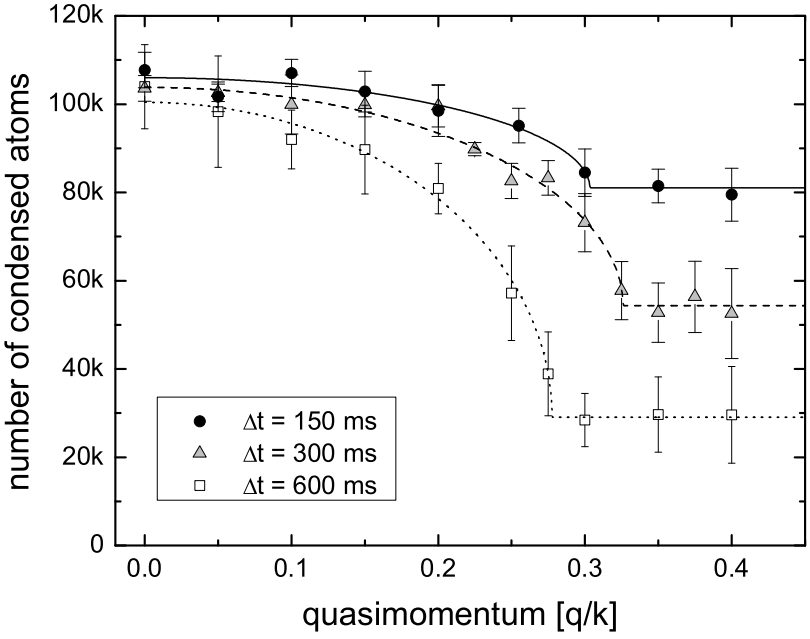

Figure 4.20: Number of atoms remaining in the condensed part of a $\sim 65\%$ condensed sample after different interaction times $\Delta t = 150$, 300 and 600 ms with an optical lattice with $s = 0.2$. The lines are fit of the experimental points with Eq. (4.42).

We have carried out a systematic study of the behavior of the mixed cloud by measuring the number of atoms in the condensed component for different values of the quasimomentum q and different interaction times Δt with the optical lattice. In Fig. 4.20 we report the results of this experiment for a lattice height $s = 0.2$, a condensed fraction $\sim 65\%$ and three interaction times $\Delta t = 150, 300$ and 600 ms. The number of condensed atoms has been obtained with a bimodal fit (Thomas-Fermi and gaussian) of the density distributions of the expanded clouds. We observe that, keeping constant Δt, the number of atoms in the condensate decreases with increasing q, eventually reaching a plateau value when $q \approx 0.3k$. This plateau value depends on the interaction time and it decreases with increasing Δt. Each point is the average of five different measurements corresponding to different realizations of the sample and the error bar is their standard deviation. In this measurement the statistics is particularly important, since the number of condensed atoms is very sensitive to the temperature of the sample and erratic variations in the thermal fraction (mainly caused by fluctuations in the trap bias field) may induce a significant source of noise. We stress that, also in this case, the range of quasimomenta shown in figure is below the threshold for the onset of dynamical instability.

In order to validate our first interpretation in terms of energetic instability, we must compare these experimental results with the predictions of the theory. In [97] the authors study the stability of the 3D-GPE and of the simplified NPSE in the ideal case of a cylindrical condensate, with a finite radial size due to the transverse harmonic confinement and an infinite extension along the symmetry axis, where the periodic potential is present. They show that a threshold for energetic instability exists, as in the case of dynamical instability, but for lower values of quasimomenta. The behavior observed in the experiment suggests a smooth dependence on the quasimomentum that is not compatible with the threshold process predicted for the axially uniform system. In the experiment, however, the condensate has a finite extension along the direction of the lattice, differently from the system considered in [97], and its density along this axis is not uniform, decreasing (and eventually going to zero) with increasing distance from the center. Actually, the thresholds for both dynamical and energetic instability depend on the density [97]. As a consequence, in an axially inhomogeneous system, one can expect to observe a continuous transition from the stable to the unstable regimes: since the density is not constant across the BEC, the low density outer region should behave differently from the high density bulk, with respect to the onset of instabilities. In the previous section, where we have discussed the observation of dynamical instability, we have not considered the inhomogeneity of the sample. Actually, the threshold for dynamical instability depends only weakly on the atomic density: for our measured peak density the calculated threshold is between $q = 0.5k$ and $q = 0.6k$ (depending on the lattice height) and for vanishing density it approaches the asymptotic value $q = 0.5k$. Instead, in the case of energetic instability, the calculated threshold for the bulk of the condensate lies around $q = 0.3k$, while for vanishing density it goes to $q = 0$.

We derive now a simple model for energetic instability that takes into account the inhomogeneity of the condensate along the axial direction. In [117] the authors calculate the sound velocity c for an infinite cylindrical condensate in the presence of transverse confinement and a periodic potential applied along the symmetry axis $\hat{z}$. They find the analytical expression

$$c = \sqrt{\frac{\tilde{g} n_0}{2m^*}}, \tag{4.34}$$

where n_0 is the central density, m^* the effective mass and $\tilde{g}$ an effective interaction constant which takes into account the presence of the optical lattice. For the lattice height and the range of quasimomenta we have considered in the experiment, we can safely substitute $\tilde{g}$ with g and m^* with m. The inhomogeneity of our system can be taken into account by using a local density approximation, assuming that Eq. (4.34) still holds when the density n_0 is a function of z. In this approximation, the condensate can be ideally divided along the symmetry axis into many slices having an almost constant central

density. Assuming that each of these slices has the same properties of the infinite system, we can calculate the z-dependent sound velocity substituting the peak density n_0 in Eq. (4.34) with the central density $\tilde{n}_0(z)$ calculated along the axis $\hat{z}$. Within these approximations we obtain an analytical expression for the local sound velocity

$$c(z) = \sqrt{\frac{g\tilde{n}_0(z)}{2m}}. \tag{4.35}$$

According to the Landau criterion, energetic instability should arise when the superfluid velocity exceeds this value. For our experimental conditions (small lattice height and small quasimomenta) the periodic potential does not substantially modify the energy spectrum of the system, so that the velocity takes the same form as in the case of the free condensate

$$v = \frac{\hbar q}{m}, \tag{4.36}$$

where we assume the quasimomentum q to be positive. Combining Eq. (4.35) and Eq. (4.36), the Landau criterion for local energetic stability $v < c(z)$ can be written in the form

$$\tilde{n}_0(z) > \frac{2\hbar^2 q^2}{gm}. \tag{4.37}$$

For a given value of q one can split the condensate in a high density region which satisfies the criterion (4.37) and is energetically stable, and a low density region which does not satisfy (4.37) and is energetically unstable. The condensate "mass" fraction which is expected to be stable can be calculated integrating the density $n(\mathbf{r})$ on the domain which satisfies Eq. (4.37):

$$\eta(q) = \frac{1}{N} \int_{\tilde{n}_0(z) > 2\hbar^2 q^2/gm} dz \iint dxdy \; n(\mathbf{r}). \tag{4.38}$$

Neglecting the modification of the condensate density caused by the weak optical lattice, we assume a Thomas-Fermi distribution

$$n(\mathbf{r}) = n_0 \left(1 - \frac{x^2+y^2}{R_\perp^2} - \frac{z^2}{R_z^2}\right) \theta \left(1 - \frac{x^2+y^2}{R_\perp^2} - \frac{z^2}{R_z^2}\right), \tag{4.39}$$

which, evaluated along the symmetry axis $\hat{z}$, gives

$$\tilde{n}_0(z) = n_0 \left(1 - \frac{z^2}{R_z^2}\right) \theta \left(1 - \frac{z^2}{R_z^2}\right). \tag{4.40}$$

Substituting Eq. (4.40) in Eq. (4.38) and carrying out the integrations, one obtains an analytical expression for the stable fraction:

$$\eta(q) = \sqrt{1 - \left(\frac{q}{q_0}\right)^2} \left[1 + \frac{1}{2}\left(\frac{q}{q_0}\right)^2 + \frac{3}{8}\left(\frac{q}{q_0}\right)^4\right] \theta \left(1 - \frac{q}{q_0}\right), \tag{4.41}$$

where $\theta(x)$ is the Heaviside function and $q_0 = \sqrt{2gmn_0}/\hbar$ is the threshold quasimomentum for which the condition (4.37) ceases to be satisfied with the peak density n_0 and the condensate is entirely unstable. As one can easy check, Eq. (4.41) satisfies the two boundary conditions $\eta(0) = 1$ and $\eta(q_0) = 0$ corresponding, respectively, to entire stability and entire instability. Once we have calculated the stable fraction, relying on purely geometric considerations, we need to make some hypothesis about the time evolution of the system. We can likely assume that the number of atoms in the stable fraction $\eta(q)$ remains constant, while the number of atoms in the unstable fraction $[1-\eta(q)]$ decays according to an unknown function $f(\Delta t)$, where Δt is the time of interaction with the lattice. Following these assumptions, we can describe the decay of the number of atoms in the condensate with the function

$$N(q, \Delta t) = N_0 \left\{\eta(q) + [1 - \eta(q)]\, f(\Delta t)\right\}, \tag{4.42}$$

where N_0 is the initial number of atoms.

The lines in Fig. 4.20 correspond to a fit of the experimental points with Eq. (4.42) assuming N_0, q_0 and $f(\Delta t)$ as free parameters. In Fig. 4.21 (left) we compare the values of q_0 obtained from this fit with the shaded area representing the calculated threshold for the onset of energetic instability in an axially homogeneous condensate with peak density $n_0 \simeq 10^{14}$ cm^{-3}, corresponding to the value we measure in the experiment. The finite width of this shaded region corresponds to the experimental uncertainty in the determination of n_0. From this comparison it turns out that the simple model derived above fairly reproduces the behavior of the experimental points as a function of the quasimomentum q. The values of q_0 obtained from the fit, even if slightly different for the three interaction times, show a nice agreement with the theoretical prediction for the onset of energetic instability in the axially homogeneous system. This is a further indication that the dissipation we observe in the presence of a thermal fraction is indeed due to energetic instability.

In Fig 4.21 (right) we plot the number of atoms $N_0 f(\Delta t)$ remaining in the condensate fraction for $q > q_0$ for different interaction times Δt. Assuming an exponential decay $N(\Delta t) = N_0 f(\Delta t) = N_0 e^{-\Delta t/\tau}$, we extract a characteristic timescale $\tau = 416 \pm 55$ ms for the onset of energetic instability in our system. In the regime of low lattice heights studied in our experiment this timescale is much longer than the one characterizing the onset of dynamical instability, for which we measure lifetimes ranging from 15 to 200 ms. However, the timescale for energetic instability is expected to strongly depend on the temperature of the system, eventually becoming extremely long at zero temperature (as suggested by the images in Fig. 4.19 showing the behavior of the pure BEC). We have not carried out a systematic investigation of the dependence of this timescale on the condensed fraction. This study could be particularly important for better understanding the effect of the finite temperature on the superfluid dynamics of a BEC.

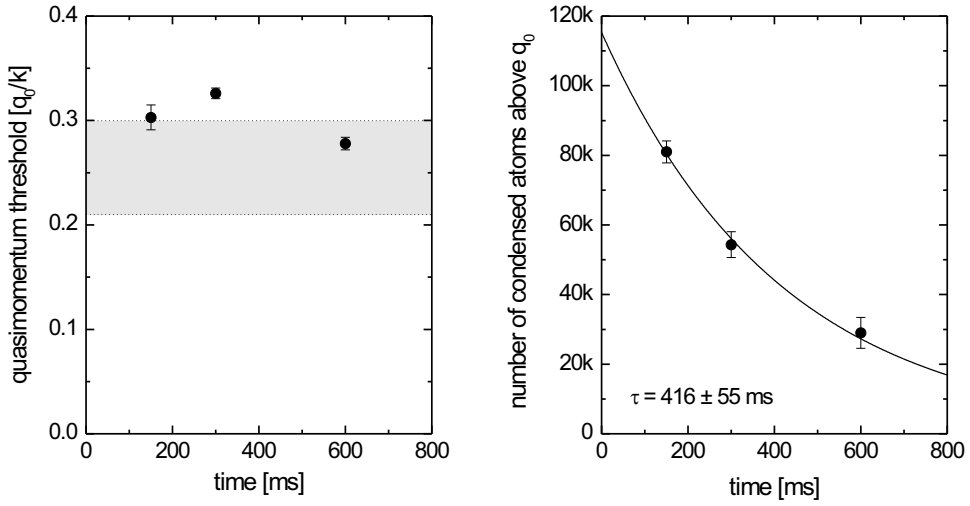

Figure 4.21: Left) The points show the threshold q_0 for energetic instability as obtained from the fit of the experimental data in Fig. 4.20 with Eq. (4.42) for different interaction times Δt with the optical lattice. The shaded area corresponds to the range of theoretical values for this threshold obtained taking into account the experimental error in the determination of the condensate peak density. Right) Number of atoms $N(\Delta t)$ remaining in the condensed fraction of the sample for $q > q_0$ after different interaction times Δt. The line is a fit of the experimental data with an exponential decay $N(\Delta t) = N_0 e^{-\Delta t/\tau}$, giving a characteristic timescale $\tau = 416 \pm 55$ ms.

4.3.5 Effect of the harmonic potential

In the above discussion we have not considered the effect of the trapping potential. In the experiment the presence of the magnetic trap is fundamental in order to have high density samples and long observation times. On the other hand, the presence of the harmonic potential may induce dynamics in the quasimomentum space, thus changing the conditions for instability. As soon as the optical lattice is switched on, the condensate acquires a finite velocity in the laboratory frame, mainly in those regions of the quasimomentum space where the energy spectrum $E(q)$ mostly differs from the free particle spectrum $E_0(q) = \hbar^2 q^2/2m$. As a consequence, moving out of the center of the trap, the condensate is subject to the restoring force $F = -m\omega_z^2 z$. As discussed in Sec. 1.2.2, from the Bloch theory it follows that, in a semiclassical approach, a force F acting on the system results in a variation of the quasimomentum according to the law $F = \hbar(dq/dt)$. Hence, equating these two expressions, one obtains the law of motion

$$\hbar \frac{dq}{dt} = -m\omega_z^2 z, \tag{4.43}$$

which can be integrated using the connection between coordinate and quasi-momentum space provided by the relation

$$\frac{dz}{dt} = \hbar^{-1}\frac{\partial E(q)}{\partial q} - v_L, \tag{4.44}$$

which gives the velocity of the wavepacket in the laboratory frame as a function of the quasimomentum q (dependent on t), with v_L velocity of the lattice. The initial condition is $q(0) = q_0$, where $q_0 = mv_L/\hbar$ is the quasimomentum state in which the condensate has been loaded.

An analytical solution of Eqs. (4.43)-(4.44) can be obtained in the limit in which q does not vary too much in time ($q(t) - q_0 \ll k$), so that a second order expansion of the energy spectrum $E(q)$ around q_0 can be applied. In this case the solution is:

$$q(t) = q_0\left[1 + \frac{m_0^*}{m}\left(1 - \frac{v_0}{v_L}\right)\cos\left(\sqrt{\frac{m}{m_0^*}}\omega_z t\right)\right], \tag{4.45}$$

which represents an oscillation with amplitude $q_0[m_0^*/m(1 - v_0/v_L)]$ and frequency $\sqrt{m/m_0^*}\omega_z$. In this expression $v_0 = \hbar^{-1}(\partial E/\partial q)|_{q_0}$ is the Bloch velocity and $m_0^* = \hbar^2(\partial^2 E/\partial q^2)^{-1}|_{q_0}$ the effective mass of the condensate in the initial quasimomentum state q_0. Using Eq. (4.43) one obtains that this solution corresponds to an oscillation also in coordinate space, as can be seen in Fig. 4.22A, where we plot the results of the integration of Eqs. (4.43)-(4.44) in this small amplitude limit.

When q_0 approaches the zone boundary, and the energy spectrum $E(q)$ significantly differs from the free particle spectrum, the amplitude of the oscillation in quasimomentum space may become macroscopic, if compared with the extent of the Brillouin zone. In this case the second order expansion of $E(q)$ cannot be used and a numerical integration of Eqs. (4.43)-(4.44) is required. In particular, when q_0 approaches the critical value for which the effective mass becomes infinite, the system may enter the anomalous dispersion region in which the effective mass is negative. At this point the atoms are pushed away from the center of the trap and, instead of oscillating around an equilibrium position, start to climb the harmonic trap wall, with q growing and growing spanning the entire Brillouin zone (in a "Bloch-oscillations like" way), as shown in Fig. 4.22B. This picture ceases to be valid when the restoring force of the magnetic trap becomes big enough to induce interband transitions (that are not included in this simple model).

We have calculated the effect of the harmonic trapping for all the combinations of q_0 and s considered in the experiment. We have taken into account this dynamics including horizontal error bars in Fig. 4.15 and 4.16, which represent the "uncertainty" in our determination of the quasimomentum state due to its variation during the measurement. All the datapoints reported in these figures refer to the oscillating case, in which q stays for all times in

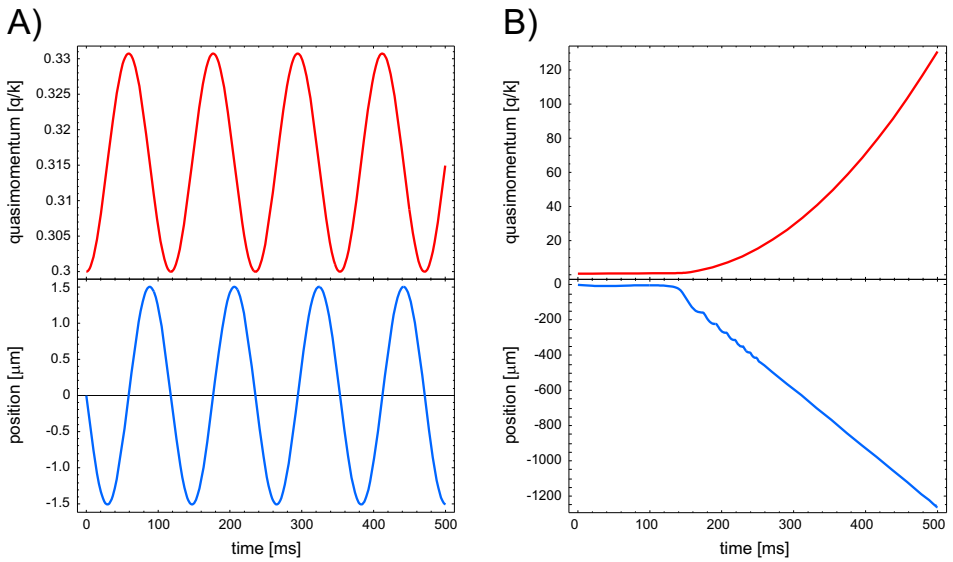

Figure 4.22: Effect of the harmonic confinement for a BEC in a moving optical lattice. The lines are obtained from the numerical integration of Eqs. (4.43)-(4.44) for a lattice height $s = 1.15$ and two different initial quasimomenta q_0. A) For $q_0 = 0.3k$ both q and z make small amplitude oscillations around an equilibrium position. B) For $q_0 = 0.6k$ the system enters a regime in which both q and z grow indefinitely.

proximity of the initial value, and the width of the horizontal error bar is the amplitude of this oscillation[3]. Increasing the lattice height, hence deforming more the free energy spectrum, the effect of the harmonic confinement becomes more and more important, seriously limiting the investigation method we have implemented.

[3]The amplitude of the oscillation in real space (~ 1 μm) is too small to be measured by our imaging system.

Chapter 5

Large spacing lattices and random potentials

In Chapters 3 and 4 we have dealt with optical lattices produced by the interference of two near-infrared counterpropagating laser beams. In this chapter we will present a different approach, that consists of imaging an arbitrary intensity pattern directly onto the condensate, thus allowing for the production of almost any kind of optical potential. The experimental setup that we have implemented allows the advantage of a simultaneous detection of both the BEC and the actual potential that it experiences.

In Sec. 5.1 we will present an experimental technique for the production of large spacing optical lattices. We show that lattice spacings starting from 8 μm can be produced by adjusting the relative angle of two partially reflective mirrors. We have performed *in-situ* imaging of the atoms trapped in the potential wells of a 20 μm spaced lattice. For a lattice spacing 10 μm we have studied the interference pattern after expansion, evidencing the presence of a periodic interference structure even when the system is localized in the individual lattice sites and the tunnelling between neighboring sites is heavily suppressed, as recently observed in [35].

In Sec. 5.2 we will present some preliminary results on both static and dynamic properties of a BEC in a random potential [34]. The disordered potential is created by imaging an optical speckle pattern onto the condensate. For strong disorder we observe a localization of the condensate in the deep wells of the optical potential. For smaller levels of disorder we observe the appearance of stripes in the expanded density distribution, together with a strong damping of both dipole and quadrupole oscillations. The measured shifts of the quadrupole mode frequency in the perturbative limit of weak disorder are explained in the frame of the Gross-Pitaevskii theory.

5.1 Large spacing optical lattices

The system made by ultracold atoms in optical lattices is a good candidate for the possible implementation of quantum computing schemes. In this context, a larger spacing optical lattice could provide the fundamental requirement of single-site addressability, that is hard to achieve in a traditional near-infrared standing-wave lattice. One possible approach consists in the realization of standing waves with CO_2 lasers emitting at 10 μm wavelength. Even if CO_2 lattices provide the advantage of a complete suppression of heating mechanisms (due to the huge detuning from resonance), they present the drawback of quite difficult manipulation. In this section we present a simple system for the creation and the detection of optical lattices with spacing starting from ≈ 8 μm, almost 20 times the spacing of a traditional standing wave lattice, still using near-infrared light produced by solid state laser sources. We have made some preliminary investigations of static and dynamics properties of the BEC in such a potential, evidencing quite different results with respect to the physics of ordinary lattices, owing to the different length and energy scales.

5.1.1 Experimental setup

The experimental setup for the production and the detection of the large spacing optical lattice is schematically shown in Fig. 5.1. The lattice beam coming from the Ti:Sa laser is shone onto a pair of partially reflective mirrors placed with a small relative angle δ one in front of the other at a distance of ≈ 1 mm. As shown in Fig. 5.2, the multiple reflection of the lattice beam from these mirrors produces, at the second order of reflection, two separate beams (of different intensities) with a relative angle 2δ. These two beams, following different optical paths, are then guided by a lens system to recombine onto the condensate, where they interfere producing a periodic pattern with alternating intensity maxima and minima. The period d of this lattice, that is oriented along the difference of the laser wavevectors, depends on the angle α between the beams according to

$$d = \frac{\lambda}{2\sin(\alpha/2)}. \tag{5.1}$$

It is easy to show that in the case of counterpropagating beams ($\alpha = \pi$) the above expression reduces to the well known spacing $\lambda/2$ for a standing wave lattice, as the ones studied in the previous chapters. On the other limit, when the two beams are almost copropagating ($\alpha \simeq 0$), d may become very large. In our setup, varying the angle δ between the two mirrors, it is possible to easily adjust the lattice spacing to the desired value. For the working wavelength $\lambda = 820$ nm the lower limit is $d \approx 8$ μm, corresponding to the maximum angle $\alpha = 25°$ that is possible to reach in our setup taking into account the finite size of the vacuum cell windows.

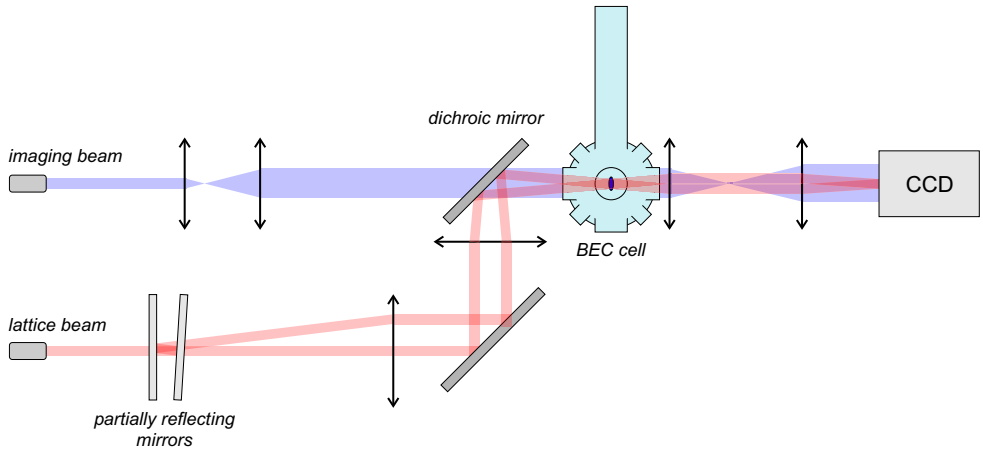

Figure 5.1: Optical setup for the production and detection of a large spacing optical lattice. The two beams creating the interference pattern are obtained from the multiple reflections of a laser beam by a pair of partially reflective mirrors placed with a relative angle one in front of the other.

Since the two beams producing the lattice have not the same intensity, we expect the resulting interference pattern to show a reduced contrast with respect to the case in which the two beams have the same intensity. It can be shown that the intensity of the lattice I_L, i.e. the intensity difference between constructive interference and destructive interference, is given by

$$I_L = I_{max} - I_{min} = 4t^2\,(1-t)\,I_0, \tag{5.2}$$

where t is the transmissivity of the partially reflecting mirrors and I_0 is the intensity of the beam incident on them. It is easy to show that this expression has a maximum for $t = 2/3$. For this reason in the experiment we have used mirrors with $t \simeq 0.7$, corresponding to the maximum lattice intensity $I_L \simeq 0.58 I_0$ achievable with this technique.

How is it possible to detect the real intensity distribution experienced by the atoms? A nice feature of the setup shown in Fig. 5.1 is that the lattice beams are aligned quasi-parallel to the radial horizontal axis of the condensate following the same path of the imaging beam. This has been possible by using a dichroic mirror, reflecting in the range $\lambda > 800$ nm and transmitting in the range $\lambda < 800$ nm. This feature allows us to use the same imaging setup to detect both the BEC and the spatial profile of the light intensity. This means that we can image in consecutive photos both the condensate and the exact potential that the condensate experiences. Indeed, since the CCD plane is conjugate to the vertical plane passing through the trap axis, the intensity profile recorded by the CCD will be exactly the same (except for a

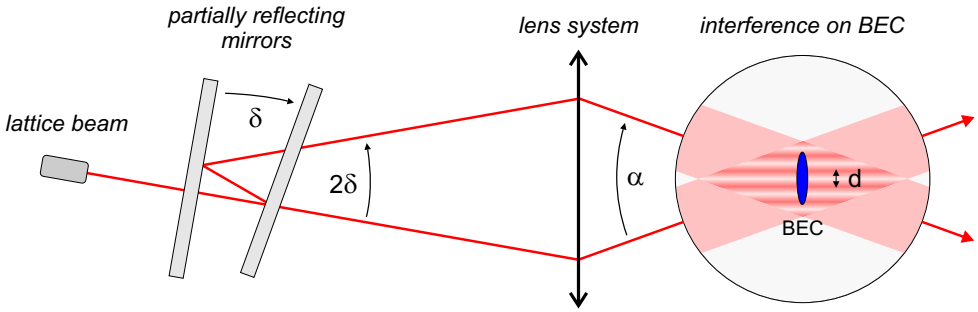

Figure 5.2: Detail of the optical system used to produce a periodic interference pattern onto the BEC. The lattice spacing d can be tuned by changing the angle δ between the two partially reflecting mirrors.

magnification factor) as the one imaged onto the condensate. Furthermore, by calibrating the CCD responsivity with a reference beam of known intensity, it is possible to convert the digitized signal of each pixel into an intensity value and, by using Eq. (3.7), calculate the height of the potential V_0. In the following, the lattice height and the other energy scales will be conveniently expressed in frequency units (using the implicit assumption of a division by the Planck constant h).

To illustrate the advantages of this imaging setup, in Fig. 5.3A we show the intensity profile of an optical lattice with spacing $d = 20$ μm, while in Fig. 5.3B we show the absorption image of the atoms trapped in the potential wells of the same lattice. The experimental sequence used to image *in situ* the atomic distribution is the following. First we produce the BEC, then, maintaining the magnetic confinement, we ramp in 100 ms the height of the lattice from zero to the final value. After the end of the ramp we wait 50 ms, then we abruptly switch off the optical lattice with the same AOM used for the ramp and, after a few tens of μs, we flash the imaging beam for the detection phase. The latter time interval is necessary not to perturb the imaging with lattice light coming onto the CCD, but is small enough not to let the atoms expand from the lattice sites once the optical confinement is released. The combination of the CCD electronic shutter and an interferential bandpass filter centered around $\lambda = 780$ nm and placed in front of the camera, allows a complete extinction of the lattice light at the time of acquisition. In Fig. 5.3C and 5.3D we show, respectively, the power spectrum of the two-dimensional Fourier transforms of the distributions shown in Figs. 5.3A and 5.3B. As one can see, both the distributions are characterized by sharp peaks in momentum space: from the position of these peaks it is possible to precisely measure the period of the observed structures.

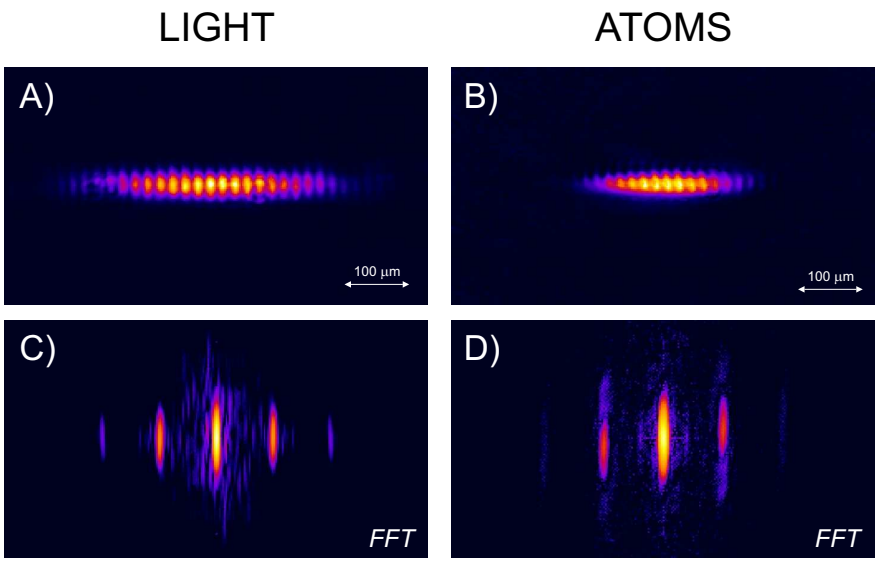

Figure 5.3: An optical lattice with $d = 20$ μm spacing. On the left we show the intensity distribution of the lattice beam (A) recorded by the CCD and the corresponding Fourier transform (C). On the right we show the density distribution (B) of the condensate trapped in the lattice sites imaged *in situ* a few μs after switching off the lattice, together with its Fourier transform (D), showing well resolved peaks in the same position as the ones in (C).

Incidentally, this technique provides an excellent way to precisely adjust the focus of the imaging setup. As a matter of fact, in the first experiments we reported the somehow surprising observation that, in the absorption images of the atoms trapped in the lattice wells, the spacing we measured was significantly different from the period of the lattice imaged on the CCD. This mismatch can be easily explained invoking a systematic error due to an out-of-focus setup of the camera. Indeed, by slightly moving back and forth the CCD along the path of the imaging/lattice beams, we have found the right position in which both the intensity of the lattice and the atomic density distribution had the same spacing. This position corresponds to the case in which the CCD is placed exactly on the plane conjugate to the atoms.

5.1.2 Expansion from the large spacing lattice

With the usual infrared standing-wave lattices employed so far in many experiments, it is not possible to optically resolve *in situ* the modulation of the atomic density distribution. As a matter of fact, in most of the cases the diagnostic of the system is carried out by removing the confining potential and imaging the atomic gas expanding after some time of flight. This kind

of analysis provides useful information on the quantum nature of the system. When the height of the optical lattice is larger than the chemical potential (tight binding regime), the system forms an array of condensates localized in the wells of the periodic potential. It has been experimentally observed that such an array of coherent atomic states, once released from the trap, produces after expansion a periodic interference pattern [18, 19, 21]. The high contrast interference observed in these experiments can be related to the long range coherence that exists in the superfluid regime when the tunnelling rate between neighboring sites is sufficiently high. Since the tunnelling rate strongly depends on the lattice spacing d (being proportional to $e^{-2d}/\sqrt{d}$ in the tight binding regime [118]), it is worth studying the expansion of the BEC from a large-spaced lattice, in which tunnelling is expected to be heavily suppressed.

Let us consider a linear array of condensates trapped in an optical lattice with spacing d. After releasing the atoms from the trapping potential one expects to observe an interference pattern with spacing

$$d' = \frac{h t_{exp}}{m d}, \tag{5.3}$$

where t_{exp} is the expansion time [2]. For the maximum expansion time $t_{exp} =$ 28 ms possible in our setup (for longer times the falling atoms would escape from the field of view), a trap spacing $d = 20$ μm would correspond to interference fringes spaced by $d' = 6.4$ μm, that is slightly below the ≈ 10 μm resolution of our imaging system. For this reason we have studied the expansion from a lattice with $d = 10$ μm, corresponding to a detectable fringe spacing $d' = 12.8$ μm. We note that for this lattice spacing the recoil energy E_R (defined in Sec. 3.1.3) is only 6 Hz, almost 600 times smaller than the recoil energy for a regular standing-wave lattice with $d = 0.4$ μm spacing.

In the experiment, after producing the BEC, we ramp in 100 ms the intensity of the lattice beam from zero to different final values (as indicated in Fig. 5.4A), then we wait 50 ms and suddenly switch off both the magnetic trap and the optical lattice. In Fig. 5.4B we show absorption images of the atomic density distribution after 28 ms of free expansion (left) together with their 2D Fourier transform (right) for different values of the lattice height from $V_0 = 0$ to $V_0 = 4.6$ kHz. Increasing the lattice height above ~ 500 Hz we note that interference fringes with the expected spacing $d' \simeq 13$ μm start to form, as indicated by the emergence of peaks in the Fourier transform, and their visibility increases with increasing lattice height. At the same time, the axial width of the overall distribution gets larger as a consequence of the increased confinement in the lattice wells, that produces a faster expansion along the lattice direction. In Fig. 5.4C we show the interference pattern observed for the maximum lattice height $V_0 = 4.6$ kHz, in which the system is deeply in the tight binding regime and we expect a localization in the lattice wells (the BEC chemical potential in the harmonic trap is $\mu \simeq 1$ kHz). However, differently from [19], for this large spacing the tunnelling between neighboring sites is

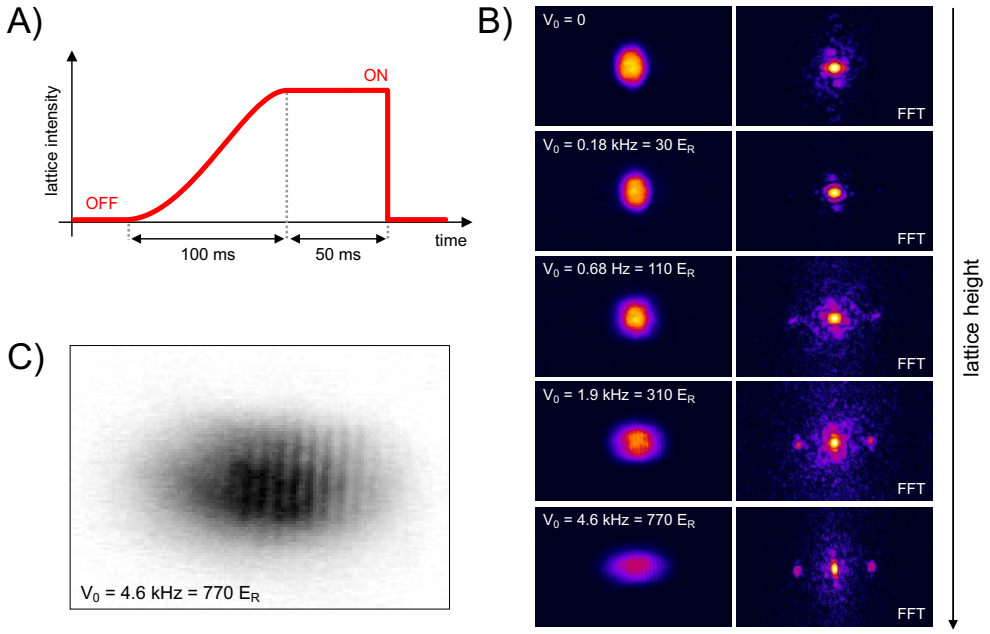

Figure 5.4: Expansion from an optical lattice with 10 μm spacing. A) The intensity of the lattice is increased adiabatically from zero to the final value in 100 ms, then after 50 ms the lattice is abruptly switched off together with the harmonic trapping potential. B) Absorption images after 28 ms of expansion (left) and corresponding Fourier transform (right) for different lattice heights V_0. C) Expanded density profile for $V_0 = 4.6$ kHz: we observe the clear presence of interference fringes.

totally suppressed and the states in the different wells do not communicate one with each other. As a consequence, each state will evolve in time independently, according to its energy, that is different from site to site due to the inhomogeneity of the sample. In this situation we are observing interference fringes from an array of phase uncorrelated matter-wave sources, as recently reported in [35] with a similar system.

A simple model. To get more insight into the problem of interference from uncorrelated sources, let us write down a very simple model. Following an obvious analogy with optics, let us consider a linear array of point-like radiation sources disposed along $\hat{z}$ with uniform spacing d, all emitting isotropically in space with the same amplitude. This problem is the extension of the Young's double slit experiment to the case of N emitters. We indicate the position of the sources along $\hat{z}$ and their phases with the variables $\{z_n, \phi_n\}$. Let us suppose to measure the field distribution on a screen parallel to $\hat{z}$, placed at

a distance D from the emitters. The field amplitude, as a function of the position z' on the screen, is proportional to a sum of phase-factors describing the wave propagation in space:

$$A(z') \propto \sum_n e^{i(\phi_n + k d_n)}, \tag{5.4}$$

where k is the modulus of the wavevector and $d_n = \sqrt{D^2 + (z_n - z')^2}$ is the distance of the n-th source from the detection point. If one assumes that $D \gg (z_n - z')$, i.e. that we are observing the interference in the far-field, we can make the following approximation

$$d_n = \sqrt{D^2 + (z_n - z')^2} \simeq D \left[1 + \frac{1}{2} \left(\frac{z_n - z'}{D} \right)^2 \right]. \tag{5.5}$$

Using this assumption, the total intensity on the screen will be given by

$$\left| A(z') \right|^2 \propto \left| \sum_n e^{i\left(\phi_n + \frac{k}{2D}(z_n - z')^2\right)} \right|^2. \tag{5.6}$$

This quantity is evaluated numerically in Fig. 5.5 for $N = 20$ sources identified by three different sets of variables $\{z_n, \phi_n\}$, in which we release one at a time the hypothesis of uniform phases and uniform spacing. The diagrams on the left show the displacement of each source $\delta z_n = z_n - nd$ from the regular lattice position and its phase ϕ_n. The graphs on the right show the field intensity $|A(z')|^2$ calculated with Eq. (5.6).

In Fig. 5.5A we consider the ideal case of equispaced sources all emitting in phase. In this situation we observe a high-contrast interference pattern characterized by well resolved peaks at a distance inversely proportional to the distance d between the sources. In optics, this is the intensity distribution produced by a diffraction grating illuminated by coherent light. In matter-wave optics, a similar interferogram is observed in the superfluid regime after the expansion of BECs released from optical lattices produced with near-infrared standing waves [19]. Working out a slightly more realistic model, in which the finite size of the emitters is taken into account, the interferogram should be convolved with the diffraction figure from a single source, resulting in a decreased visibility of the higher order peaks.

In Fig. 5.5B we consider the case of equispaced sources with random phases. The interferogram on the right corresponds to the randomly generated set of phases shown on the left. In this case, even if no coherence is present across the array, we can still observe a periodic structure in the interferogram. This is indeed what we observe in Fig. 5.4C and what has been studied, both theoretically and experimentally, in [35]. We note that this periodic interference is produced in a single shot. Actually, averaging the intensity

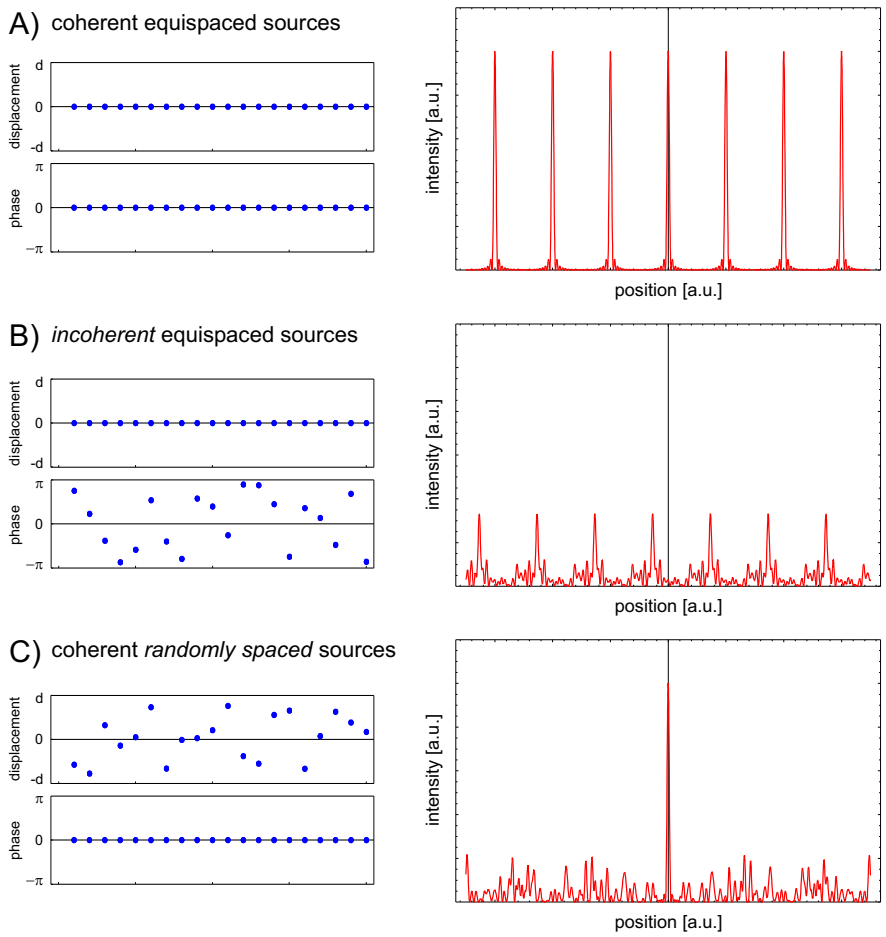

Figure 5.5: Far-field intensity obtained from the interference of a linear chain of 20 point-like emitters. On the left of each row the diagrams show the particular set of positions and phases of the sources used to calculate, with Eq. (5.6), the interferograms shown on the right. The three rows refer to: A) uniform phase and uniform spacing; B) random phase and uniform spacing; C) uniform phase and random spacing.

distribution on many different realizations, the contrast of the interferogram is expected to rapidly vanish, since the uncorrelated phases produce a pattern that differs from shot to shot both in the relative position of the peaks and in their visibility. The persistence of a periodic interference pattern even in the case of phase-uncorrelated sources is an effect essentially related to the limited number of emitters that interfere. Indeed, in the case of only two sources, even if there is no phase relation between them, one expects to observe a perfect interference pattern with 100% contrast [2]. Increasing the number of sources,

the visibility of the peaks decreases and more complex structures start to grow. Even if the overall distribution still shows periodicity, the harmonic content of the interferogram grows at the expenses of a reduced visibility and, in the limit of a very large number of sources, the interference pattern could be confused with noise. However, a correlation measurement should still be able to detect a periodic structure, that is closely related to the ordered distribution of the emitters. A detailed analysis of such a problem is carried out in [35].

In Fig. 5.5C we consider the case of coherent sources with a random displacement from their regular position $z_n = nd$. The interferogram on the right corresponds to the randomly generated set of displacements shown on the left. While in the case of random phases and uniform spacing a periodic interference pattern is still visible in a single shot, in the case of random spacing no particular structure is visible at all, even if all the sources emit coherently. We will come back on this point in Sec. 5.2.2 studying the expansion of a BEC from a disordered potential.

5.1.3 Dipole oscillations in the large spacing lattice

In order to get more information on the behavior of the system in the different regimes of lattice height, we have studied dipole oscillations of the harmonically trapped BEC in the presence of the lattice. The experimental technique used to induce dipole oscillations is the same described in Sec. 3.2.2. In Fig. 5.6 we show the center of mass position of the expanded cloud as a function of time for a trap displacement $\Delta z = 32$ μm and different lattice heights. The black points refer to the regular undamped oscillation of the condensate in the pure harmonic potential at the trap frequency $\nu_z = (8.74 \pm 0.03)$ Hz.

The gray points correspond to the center-of-mass motion in a shallow lattice with $V_0 = 170$ Hz, corresponding to 28 recoil energies. In this case we observe a damped oscillation of the center of mass at the same frequency of the harmonic trap. This result is qualitatively different from what observed in Sec. 3.2.2 studying dipole oscillations in the standing wave lattice with $d = 0.4$ μm, where we have observed a shift of the dipole mode frequency that could be explained in terms of a modified effective mass. The main difference is that, for a lattice spacing $d = 10$ μm and a trap displacement $\Delta z = 32$ μm, the motion of the atomic cloud in momentum space is no longer confined in the center of the first Brillouin zone, where the band is approximately parabolic. Let us assume that the Bloch picture is still valid in this regime, in which the condensate occupies only ~ 15 sites. Since the lattice spacing is 25 times bigger, the corresponding width of the Brillouin zones is 25 times smaller. Indeed, in this case the atoms are spanning many Brillouin zones, making Landau-Zener tunnelling from one band to the next one at each passage from the zone edges. The actual energy spectrum probed by the atoms during the oscillation is essentially the free particle one, with a curvature set by the real mass m, except for a small modification at the bottom, where small

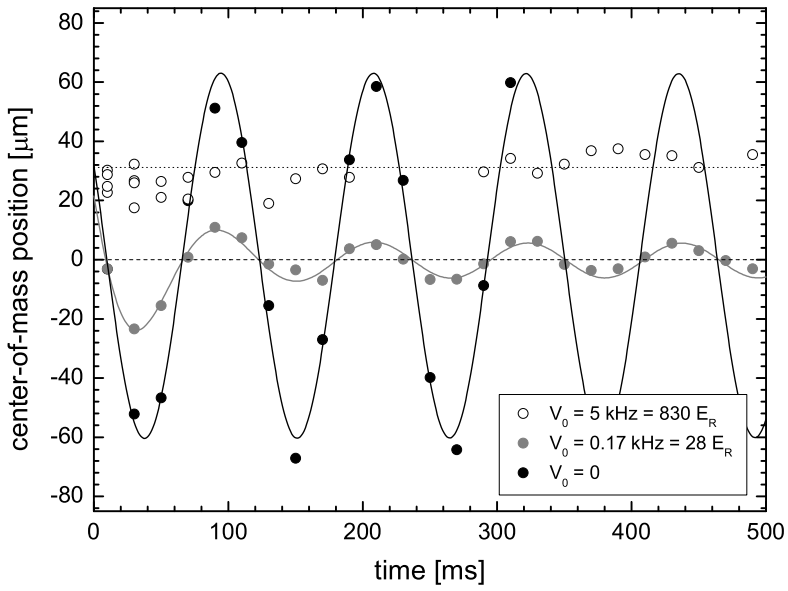

Figure 5.6: Dipole oscillations of a harmonically trapped BEC in the presence of an optical lattice with 10 μm spacing. The dotted line is the initial position of the atoms at $t = 0$. The dashed line is the center of the magnetic trap after the excitation of the dipole mode. The black points refer to the oscillation without lattice, the gray points show a damped oscillation in a lattice with height $V_0 = 170$ Hz, while the empty circles show the localization in a lattice with height $V_0 = 5$ kHz.

energy gaps form between the very first bands. In order to observe effects of reduced effective mass, as the ones studied in Sec. 3.2.2, one should use a much smaller amplitude oscillation (~ 1 μm), that could be barely detectable with our imaging setup, in order to stay within one Brillouin zone.

Coming back to Fig. 5.6, increasing the height of the optical lattice to $V_0 = 5$ kHz $= 830 E_R$, we observe that the center-of-mass motion is blocked and the atomic cloud stays at a side of the displaced harmonic trap. Indeed, in this regime the height of the periodic potential becomes higher than the chemical potential of the condensate and the system localizes in the different sites. Differently from the standing wave lattice, in which the tunnelling ensures a collective motion even in the tight binding regime, in this case the tunnelling between adjacent sites is heavily suppressed by the large distance between wells, and the atomic states in each site are expected not to communicate one with each other. We note that, for this lattice height, we detect clear interference fringes as the one reported in Fig. 5.4C for all the evolution times considered in Fig. 5.6. The hypothesis of interference from independent localized states formulated in the previous section is thus confirmed by the

observation that, even in the presence of an external potential gradient, the center of mass does not move in time.

We would like to note that this localization effect cannot be attributed to the generation of a Mott insulator state [21], as also suggested in [35]. Indeed, in the Mott insulator phase the system presents nontrivial localization properties on a timescale much longer than the tunnelling times. In our case the tunnelling is so heavily suppressed that the observation of the system is necessarily limited to a timescale on which the long-range coherence properties of the system cannot be detected. Actually, what we are observing in the experiment is a trivial localization effect produced only by the strongly increased tunnelling times, and not by an actual competition between interaction and tunnelling energies [21].

5.2 Random potentials

In the previous section we have discussed a technique for the production of large spacing optical lattices. Using slightly different optical systems it is possible to image arbitrarily complex intensity distributions onto the condensate. One interesting possibility is offered by *speckle patterns*, that are produced by the complex interference of the light scattered by non-specular surfaces or transmitted by diffusive media. This pseudo-random intensity distribution can be efficiently used to produce disordered potentials [119].

The effects of a disordered potential on a bosonic system have been intensely explored both theoretically and experimentally, particularly in the context of liquid ^{4}He flowing in a porous material, where the breakdown of superfluidity with sufficient disorder was observed [120]. Theoretical works have demonstrated that at zero temperature, under particular conditions, a bosonic fluid in a disordered potential can be characterized by a superfluid fraction significantly smaller than the condensate fraction [121, 122, 123].

Bose-Einstein condensates of dilute gases are an ideal system for the investigation of disorder-related phenomena. One of the most appealing consequences of disorder is the possibility of inducing a quantum phase transition from a superfluid to a strongly-interacting *Bose-glass* state [124, 125, 126], characterized by a nontrivial localization of the atoms in the random potential wells, induced by the cooperation between interactions and disorder. In weakly interacting systems the presence of disorder can induce *Anderson localization* [127], a phenomenon well known in solid state physics, responsible for the disruption of the electron transport caused by the presence of defects [128]. Anderson localization has been recently observed for light propagating in strongly scattering semiconductor powders [129]. In the very last years, several theoretical works have discussed the possibility of observing the Bose-glass and Anderson localization transitions for a BEC in an optical lattice when a disordered potential is added to the system [22, 23].

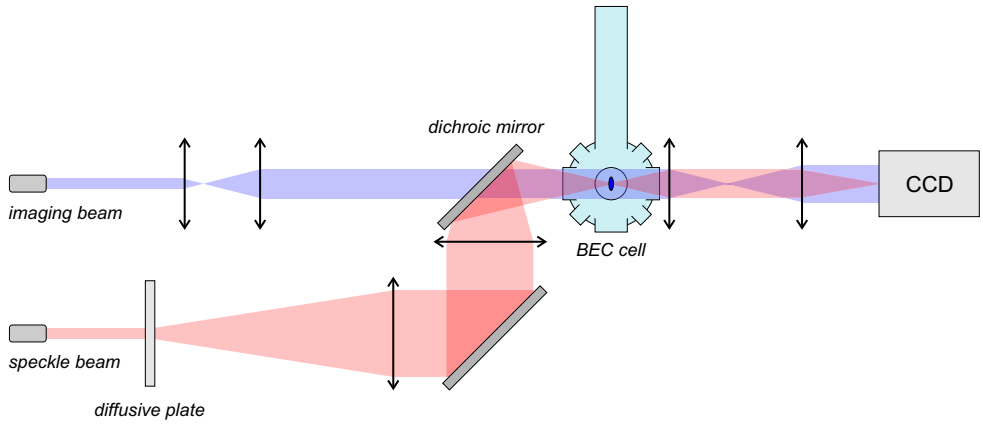

Figure 5.7: Optical setup for the production and detection of the speckle pattern. An off-resonant beam is shone through a diffusive plate and the resulting intensity distribution is imaged onto the BEC.

From an applicative point of view, investigating the effects of disorder is important for the study of Bose-Einstein condensation on microstructured magnetic traps. Some experimental works have evidenced a fragmentation of the condensates trapped in the proximity of the chip surface [130, 131] and this effect has been recently attributed to pseudo-random fluctuations in the trapping potential caused by manufacturing imperfections in the fabrication of the microchips [132, 133, 134]. It is crucial for the future of integrated atom optics on microchips to quantitatively investigate these effects, defining how the presence of disorder could affect the coherence and transport properties of the trapped samples.

In this section we present the first observation of a BEC in a random potential [34]. The disordered potential, that is stationary in time and randomly varying in space, is created with an optical speckle pattern superimposed to the magnetic trap in which the condensate is produced. The degree of disorder can be easily tuned by changing the laser parameters, as well as the precise speckle realization can be changed and precisely detected.

5.2.1 Experimental setup

The experimental setup used for the production and the detection of the speckle potential, schematically shown in Fig. 5.7, is very similar to the one used for the large spacing lattice. The off-resonant beam coming from the Ti:Sa laser is shone onto a diffusive plate made up of many randomly-distributed scattering centers, producing a complex interference pattern in the far field. This intensity distribution is then imaged onto the condensate using the same system described in Sec. 5.1.1 in the case of the optical lattice.

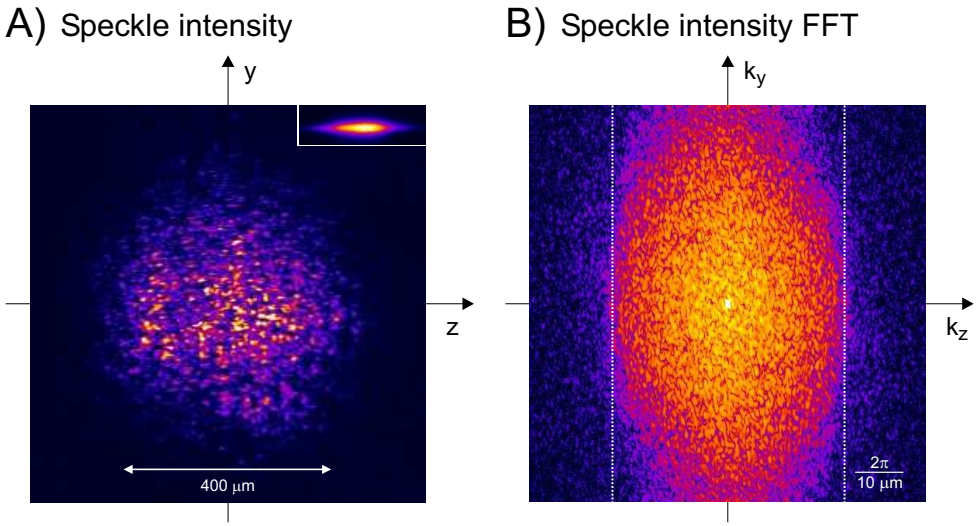

Figure 5.8: A) Intensity distribution of the speckle pattern recorded by the CCD. The inset in the top right corner shows the size of a typical trapped BEC. B) Fourier transform of the speckle pattern. The vertical dotted lines delimiting the edge of the distribution along the z axis correspond to structures with a spatial period of ~ 10 μm.

Again, the speckle beam is aligned along the BEC radial horizontal direction on the same path of the imaging beam, so that it is possible to use the same CCD camera to image in consecutive photos both the BEC and the speckle distribution. In Fig. 5.8A we show the intensity distribution recorded by the CCD for a typical speckle realization. As indicated by the 2D Fourier transform in Fig. 5.8B, the spatial spectrum of this pattern is quite flat, but with an upper limit due to the finite resolution of the imaging system. The vertical dotted lines delimiting the edge of the distribution along the z axis correspond to structures with a spatial period of ~ 10 μm.

The speckle pattern produces a 2D potential that is stable in time and varies spatially along the axes $\hat{y}$ and $\hat{z}$ orthogonal to the direction $\hat{x}$ along which the beam propagates. Along the $\hat{x}$ axis the intensity is constant, since the beam is only slightly focused on the trap center, so the condensate experiences the effect of many randomly-distributed potential tubes. As a consequence of the speckle size $10 \div 20$ μm and of the trap anisotropy, the cigar-shaped BEC probes ≈ 10 wells in the axial direction and only ≈ 1 well along the radial direction, as suggested by the inset in the top right corner of Fig. 5.8A, where we show on the same scale the image of a trapped BEC. Following these considerations, the speckle potential can be considered in first approximation as one-dimensional.

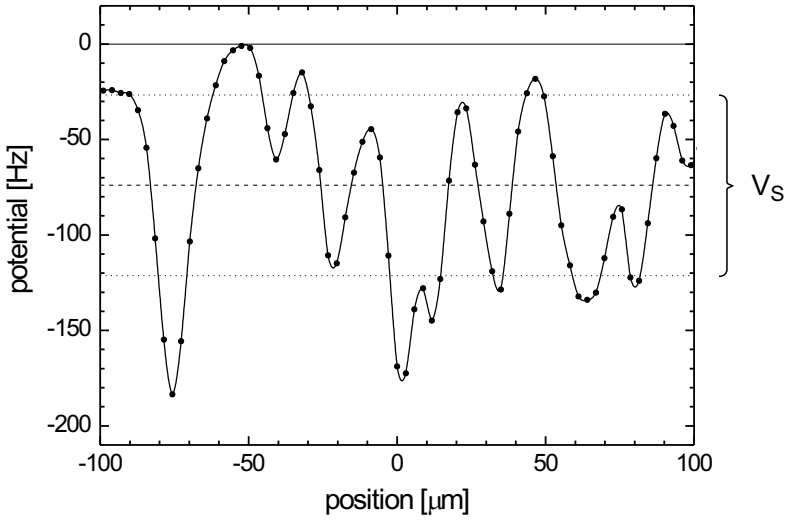

Figure 5.9: Axial cross section of the speckle potential. The points correspond to the intensity recorded by the CCD while the continuous line is a cubic interpolation. The dashed line indicates the mean value $< V >$ of the potential on the plotted 200 μm interval, while the dotted lines refer to one standard deviation σ_V below and above the average value. We define the mean speckle height V_S as twice the standard deviation.

In order to calibrate the height of the potential, we use the same procedure described in Sec. 5.1.1. We first measure the responsivity of the CCD by illuminating the camera with a reference beam with the same wavelength $\lambda = 822$ nm and known intensity. In this way it is possible to associate each pixel count to an intensity value and, using Eq. (3.7), calculate the height of the potential. In Fig. 5.9 we show a typical cross section of the speckle potential along the trap axis. The points correspond to the intensity recorded by the CCD while the continuous line is a cubic interpolation. In order to quantify the strength of the disorder we have to give an operative definition of the speckle height V_S. For this reason, we make a statistical analysis of the potential on a 200 μm interval around the trap center, calculating the mean value $\langle V \rangle$ and the standard deviation σ_V. We define the speckle height V_S as twice σ_V, as shown by the dotted lines in Fig. 5.9. More precisely,

$$V_S \equiv 2\sigma_V = 2\sqrt{\frac{\sum_j \left[V(z_j) - \langle V \rangle\right]^2}{N-1}}, \tag{5.7}$$

where the sum runs on the N samples $V(z_j)$ of the speckle potential.

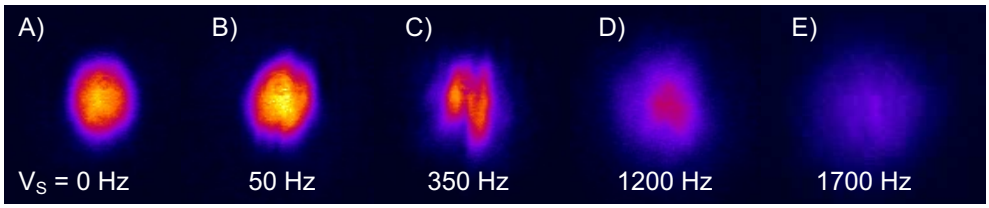

Figure 5.10: Absorption images of the atomic density distribution following 28 ms of expansion after the release from the speckle potential. The numbers in the bottom indicate the speckle height V_S defined in Eq. (5.7) in h units.

5.2.2 Expansion from the random potential

As in the case of the large spacing optical lattice, we have started to gather information on the behavior of the BEC in the disordered potential by looking at the atomic density distribution after expansion. After producing the BEC in the magnetic trap, we increase the intensity of the speckle beam in 200 ms from zero to different final values V_S using an exponential ramp with time constant 40 ms. At the end of the ramp we wait for 50 ms, then we suddenly switch off both the magnetic trap and the speckle beam and, after an expansion time of 28 ms, we image the atomic cloud. In Fig. 5.10 we show absorption images of the atomic density distribution for different values of the speckle height from $V_S = 0$ to $V_S = 1.7$ kHz. We observe three different regimes. For very small optical potentials $V_S \lesssim 100$ Hz we do not observe any significant deviation from the regular Thomas-Fermi shape of the BEC expanding from the harmonic potential (Fig. 5.10A,B). For higher speckle heights 100 Hz $\lesssim V_S \lesssim 1$ kHz we observe that the density distribution is strongly modified by the appearance of complex structures in the form of vertical stripes (Fig. 5.10C). Such long wavelength modulations can be a signature of the development of different phase domains across the BEC, having some similarities with the stripes observed with highly elongated quasi-condensates [135, 136] or with the structures produced by the growth of different momentum components following the onset of dynamical instability (as studied in Sec. 4.3.3). We note that the average spacing of these stripes $d' \gtrsim 50$ μm cannot be related to the characteristic length scale of the speckle pattern $d \approx 10 \div 20$ μm, since the latter would give rise to an interferogram length scale $d' \approx 6 \div 12$ μm after 28 ms of expansion. Finally, further increasing the speckle height to $V_S \gtrsim 1$ kHz, the expanded density profile ceases to be characterized by stripes and we detect only a broad unstructured gaussian distribution (Fig. 5.10D,E).

In order to check that this optically-thin gaussian distribution is not a trivial effect of an increased temperature of the sample, we have verified that the loading procedure is effectively adiabatic and no heating of the atomic cloud is produced by the presence of the speckle potential. This has been

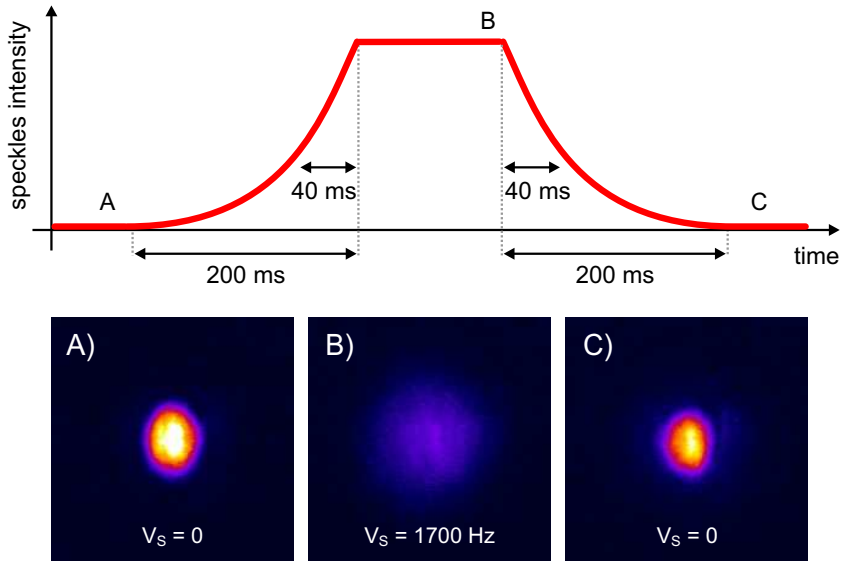

Figure 5.11: Adiabatic loading of the BEC in the speckles. Top) The height of the potential is increased from zero (A) to the maximum value $V_S = 1700$ Hz (B) using a 200 ms exponential ramp with time constant 40 ms, then is switched off using the inverse ramp (C). Bottom) Absorption images of the atomic density distribution following 28 ms of expansion after the release from the speckle potential at the times (A), (B) and (C).

checked by raising the intensity of the potential to the maximum value $V_S = 1.7$ kHz and then switching off the speckle beam using the inverse exponential ramp, as shown in the top of Fig. 5.11. The results of this test are shown in the bottom part of the same figure, where we observe that after this procedure the expanded density distribution (C) has the same Thomas-Fermi profile as the one reported in (A) for the BEC ground state in the pure harmonic potential. This observation confirms that no heating is introduced either in the loading process or by the permanence in the speckle potential. Actually, using faster ramps we have observed that the final density profile was perturbed by the presence of long-wavelength modulations as the one observed in Fig. 5.10C in the weak disorder regime, suggesting that the ground state was not recovered.

Once it is proved that the density distribution in Fig. 5.10E is not a trivial effect of heating, we can interpret it as the effect of the localization of the condensate wavefunction in the valleys of the disordered potential. Indeed, for these speckle heights we expect to enter the tight binding regime and to have some form of localization (we remind that the chemical potential of the harmonically trapped BEC is $\mu \simeq 1$ kHz). In the frame of the model derived in Sec. 5.1.2, we have observed that, unlike the case of an equispaced array

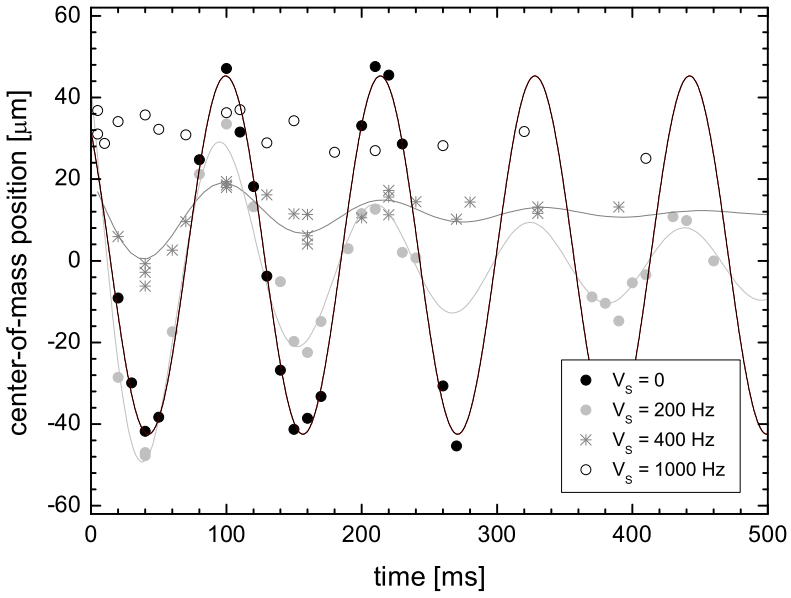

Figure 5.12: Dipole oscillations in the harmonic + disordered potential for different values of the speckle height V_S. The black and light gray lines are fit of damped oscillations to the experimental data. The darker gray line is a guide for the eyes.

of incoherent sources, in the case of a finite number of emitters with irregular spacing one cannot detect any periodic interference pattern, neither for incoherent or coherent sources. The increased size of the gaussian distribution with respect to the Thomas-Fermi profile of the harmonically trapped condensate has to be attributed to the increased optical trapping frequency experienced in average by the atomic states located in the potential wells.

5.2.3 Collective excitations in the random potential

In this section we will consider collective excitations of the condensate in the combined harmonic + speckle potential. Let us start to consider dipole oscillations, in the same way as we have done with the large spacing optical lattice in Sec. 5.1.3. After producing the BEC in the harmonic trap, we increase in 200 ms the intensity of the speckle beam using an exponential ramp with 40 ms time constant, then we excite the dipole oscillation using the same technique described in Sec. 3.2.2. In Fig. 5.12 we show the center of mass position of the expanded cloud as a function of time for a trap displacement $\Delta z \simeq 27$ μm and different speckle heights V_S. The black points refer to the regular undamped oscillation of the condensate in the pure harmonic potential at the trap frequency (8.74 ± 0.03) Hz. Increasing the speckle height to $V_S = 200$ Hz

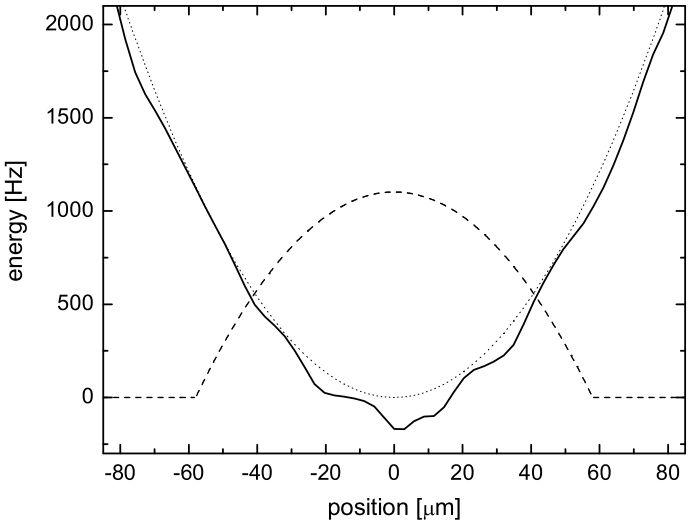

Figure 5.13: The dotted line shows the axial cross section of the pure harmonic trap potential. The continuous line is the sum of the harmonic and the disordered potential for the speckle realization plotted in Fig. 5.9 with $V_S \simeq 100$ Hz. The dashed line represents the axial cross section of the Thomas-Fermi density distribution for the BEC ground state in the pure harmonic potential (the height corresponding to the chemical potential μ).

(light gray points) we observe a damped oscillation around the center of the displaced trap. Increasing the speckle height to $V_S = 400$ Hz (gray stars), in the regime where strong modulations are visible in the expanded density profile (see Fig. 5.10C), the center-of-mass oscillation, now extremely damped, is no more centered in the new harmonic potential minimum, instead it asymptotically tends to a position closer to the center of the undisplaced trap. This effect can be attributed to the inhomogeneity of the random potential: contrarily to the case of the optical lattice, where the potential barriers have all the same height, in this case the potential landscape is much more irregular and shallow barriers alternate with higher ones. As a consequence, a fraction of the atomic cloud may localize in deep potential wells without the possibility of escaping, thus shifting the center of the oscillations towards the original trap position. Finally, increasing the intensity to $V_S = 1000$ Hz (empty circles), in the regime where an unstructured gaussian profile is visible in expansion (see Fig. 5.10D), the center-of-mass motion gets frozen, as a consequence of a complete localization of the system in the potential wells.

In order to acquire more information on the behavior of the condensate in the presence of disorder, we have performed a systematic study also of the BEC quadrupole oscillations when a weak disorder in the range $0 < V_S \lesssim 200$

Hz is added to the harmonic confining potential. In this regime the speckles produce just a weak perturbation of the harmonic trap, as it is shown in Fig. 5.13 for $V_S = 100$ Hz, where the continuous line is the axial cross section of the harmonic + random potential. In order to convey a more precise idea of the energy and length scales characterizing this regime, we have plotted in the same figure also the Thomas-Fermi shape of the BEC ground state in the pure harmonic potential (dashed line), with the height of the inverted parabola corresponding to the chemical potential.

As described with more details in Sec. 3.2.2, the quadrupole mode is excited by modulating the trap bias field at a frequency close to the theoretical quadrupole frequency $\sqrt{5/2}\omega_z$ for a harmonically trapped BEC in the Thomas-Fermi limit. During this excitation procedure the speckle potential remains stationary. The amplitude and the length of the modulation (five cycles) have been chosen in such a way to produce a 5% oscillation of the BEC axial width. After the excitation of the quadrupole mode we wait for different evolution times Δt, then we switch off both the magnetic and speckle potential and measure the aspect ratio of the condensate after expansion. From a fit of the experimental points with a damped sine function we extract the frequency and the damping rate of the oscillation.

In Fig. 5.14A we plot the frequency of the quadrupole oscillation as a function of the speckle height V_S for two different speckle realizations (filled and empty circles), obtained with a translation of the diffusive plate. The frequency is expressed as a percentage shift with respect to the quadrupole frequency (13.72 ± 0.06) Hz measured in the pure harmonic trap. We observe that, for a particular realization of the speckle pattern, the frequency shift grows with increasing height of the potential. In particular, we measure both negative and positive shifts, whose amplitude and sign depend on the particular realization of the speckle potential. In Fig. 5.14B we plot the damping rates for the same two realizations, clearly showing that the damping of the oscillation becomes stronger when the speckle height is increased (as also observed in the dipole oscillations of Fig. 5.12).

In Sec. 3.2.1 we have shown that in the Thomas-Fermi limit the quadrupole mode frequency of a harmonically trapped elongated BEC is $\sqrt{5/2}\omega_z$. In the presence of a different potential, this value can be modified by both the deviation of the potential from a pure harmonic oscillator, and other effects such as changes in the condensate and superfluid fraction, modification of the interatomic interactions, or an increase in the thermal fraction[1]. In the same section we have demonstrated that in the presence of a periodic potential along the trap axis the quadrupole mode frequency is $\sqrt{5/2}\omega_z^*$, where $\omega_z^* =$

[1] Actually, even without the speckle potential, our measured quadrupole frequency is shifted -0.7% with respect to the value $\sqrt{5/2}\omega_z$, as shown by the continuous line in Fig. 5.14A, similarly to what has been measured previously and attributed to the presence of a residual not-avoidable thermal component [16].

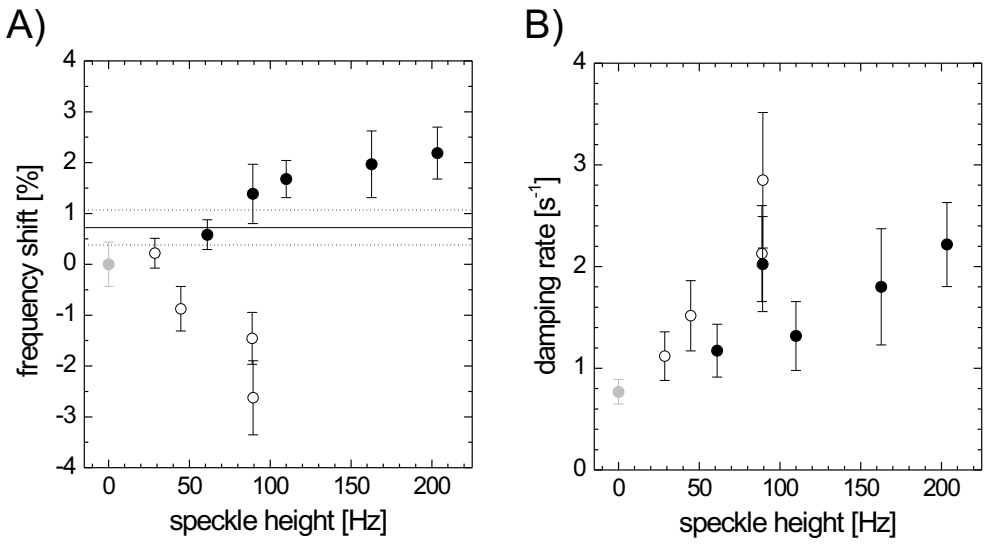

Figure 5.14: Quadrupole oscillations in the harmonic + disordered potential for two different speckle realizations (empty circles and filled black circles). A) Frequency shift with respect to the frequency measured in the pure harmonic potential (filled gray circle). The continuous line corresponds to the theoretical value $\sqrt{5/2}\omega_z$ valid in the Thomas-Fermi limit (the error in the experimental determination of the trap frequency ω_z is shown with dotted lines). B) Damping rate of the quadrupole oscillation.

$\sqrt{m/m^*}\omega_z$ is the axial trap frequency renormalized with the effective mass m^* introduced by the periodic potential.

To understand the effect of a shallow random potential on the BEC collective modes (dipole and quadrupole) we have compared the experimental observations with the solution of the time-dependent Gross-Pitaevskii equation (1.16) for the actual speckle potentials imaged by the CCD camera [137]. The GPE is solved after a sudden change in the axial trapping frequency (for the excitation of the quadrupole mode), or after a sudden displacement of the harmonic trap (for the excitation of the dipole mode). The simulations show that for small amplitude excitations the BEC oscillates coherently with no appreciable damping for evolution times up to 600 ms. In the case of the quadrupole mode the numerical results evidence a frequency shift that increases with increasing V_S, as qualitatively confirmed by the experimental data in Fig. 5.14A. The GPE simulations also predict a shift of the dipole mode, whose magnitude increases for decreasing amplitude oscillations. Actually, for larger oscillations the BEC probes more of the outer unperturbed harmonic potential, and less of the central perturbed potential (see Fig. 5.13). Significant frequency shifts ($> 1\%$) are calculated only for small amplitude oscillations ($\Delta z \lesssim 5$ μm),

but unfortunately we do not have sufficient signal-to-noise ratio to measure these shifts. For larger amplitude oscillations ($\Delta z \simeq 30$ μm) the frequency measurements are more precise and we do not observe any shift.

This theoretical analysis shows that, in the limit of small amplitude oscillations, the frequencies of both the dipole and quadrupole modes are shifted towards higher or lower values depending on the particular speckle realization. Furthermore, in some configurations a red shift is calculated for one mode and a blue shift for the other. This result of uncorrelated dipole and quadrupole frequency shifts is different from what we have seen in Sec. 3.2.1 for the collective excitations of a BEC in a standing wave optical lattice. Actually, in that case we have observed that, changing the height of the periodic potential, the dipole and quadrupole frequencies ω_D and ω_Q scale in the same way.

The numerical result obtained from the solution of the GPE can be explained by using a *sum rules* approach [41]. According to this technique, when the speckle height is sufficiently small and the random potential $V(\mathbf{r})$ can be treated as a perturbation of the harmonic trap, the frequencies of the low lying collective modes can be estimated as [137]

$$\omega_D^2 \simeq \omega_{D0}^2 + \frac{1}{m}\langle \partial_z^2 V \rangle_0 \tag{5.8}$$

$$\omega_Q^2 \simeq \omega_{Q0}^2 + \frac{1}{m}\frac{\langle z\partial_z V + z^2\partial_z^2 V\rangle_0}{\langle z^2\rangle_0}\ , \tag{5.9}$$

where ω_{D0} and ω_{Q0} are the unperturbed frequencies and the expectation value $\langle ... \rangle_0$ is calculated on the unperturbed ground state (for the quadrupole mode we assume a strongly elongated BEC). These analytical expressions demonstrate that the dipole and quadrupole frequencies have different dependencies on the particular characteristics of the perturbing potential. This approach, though less accurate than the explicit solution of the GPE, has the advantage of providing a semi-analytical explanation of the results and to strongly reduce the computational effort[2]. In Fig. 5.15A we show the predictions of the sum rules for 150 different speckle potentials with $V_S \simeq 30$ Hz. The filled circles indicate the shift of the quadrupole mode frequency, while the empty circles refer to the dipole mode. The different speckle realizations have been obtained from the same 2D experimental pattern (as the one imaged in Fig. 5.8A) by taking consecutive axial cross sections at different vertical positions with 1 μm step. We observe that the shifts of both the dipole and the quadrupole modes strongly depend on the particular speckle configuration, but the mean shifts, averaged on the ensemble of realizations, are close to zero for both the modes. In the case of the quadrupole mode we have performed a similar series of measurements experimentally. Fig. 5.15B shows the measured quadrupole frequency for different realizations of the speckle potential at $V_S \simeq 80$ Hz.

[2]It has been verified [137] that, for several different potentials $V(\mathbf{r})$, the results of the sum rules are in agreement with the full solution of the GPE.

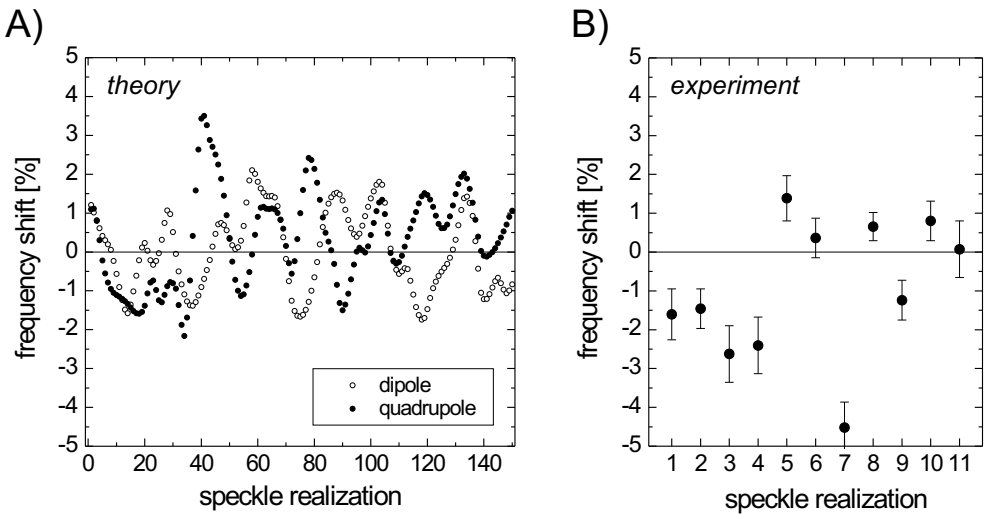

Figure 5.15: A) Frequency shifts of the dipole (empty circles) and quadrupole mode (filled circles) calculated using the sum-rules approach described in the text for $V_S \simeq 30$ Hz. The different realizations correspond to many consecutive axial slices of the same 2D speckle pattern taken at different vertical positions. B) Frequency shifts of the quadrupole mode measured for different speckle realizations with $V_S \simeq 80$ Hz.

Within our limited statistics we observe both red and blue shifts, with a slight bias towards negative shifts.

As shown in Fig. 5.15A, we expect the frequencies of the collective modes to be extremely sensitive to the particular realization of the random potential. For this reason it is important to watch out the mechanical stability of the optical setup, in such a way to have a good control on the exact realization of the speckle potential. In our experiment we have observed that the speckle pattern can maintain the same intensity distribution for many weeks without any adjustment and the absolute position of the intensity peaks (imaged onto the BEC) changes less than 2 μm day to day.

In the numerical solution of the GPE there are some indications that, for larger amplitude oscillations, the superfluidity of the system may be compromised, with the appearance of short wavelength density modulation and damped oscillations [137]. We have started the experimental investigation of large amplitude quadrupole excitations, finding first evidences of increased frequency shifts and strong perturbations of the expanded density profile.

Conclusions and perspectives

In the very last years Bose-Einstein condensates in optical lattices have been the subject of extremely intense and rewarding research, both theoretical and experimental. The motivations for the study of such systems are numerous and can be coarsely divided in two main groups. A first line of research uses optical lattices to study the transport and superfluid properties of Bose-condensed systems. Optical lattices have been used to probe the phase coherence of atomic samples and to study the Josephson dynamics induced by the tunnelling across the optical barriers. These systems also represent an ideal testground for many fundamental problems of solid state physics connected with the theory of quantum transport in a periodic potential. A second line of research takes advantage of optical lattices as tools to create arrays of tightly confining traps used to localize the atoms either in one, two or three dimensions. The strong confinement provided by such lattices allows the investigation of effects of reduced dimensionality in correlation with the physics of strongly interacting systems. Furthermore, atoms loaded in the ground state of optical lattices could provide a fruitful system for the implementation of quantum computing schemes.

This PhD work joins this extremely rich field of research, bringing new elements for the comprehension of these systems. In particular, we have focused our investigation on some fundamental aspects of the transport and superfluid properties of Bose-Einstein condensates in 1D optical lattices.

In a first series of experiments we have studied the dynamics of a condensate in a static optical lattice superimposed to the harmonic confining potential. More precisely, we have investigated how the frequencies of the collective modes are affected by a change in the lattice height. For small amplitude oscillations the effect of the periodic potential can be accounted for by normalizing the harmonic trap frequency with an *effective mass* taking into account the modified inertia of the system. In the large amplitude regime we have evidenced a disruption of coherent dipole oscillations and the emergence of an *insulating* regime. This breaking of superfluidity, accompanied by a partial loss of coherence, is interpreted in terms of a dynamical instability driven by the interplay between nonlinearity and periodicity.

In a second series of experiments we have used a moving optical lattice to

precisely control the relative motion of the BEC with respect to the optical potential. In a low density regime we have shown that the center-of-mass dynamics of the condensate exactly follows the Bloch theory for a quantum particle in a periodic potential. The effects of a modified effective mass (already evidenced in the frequency shift of the collective modes) have been observed on the condensate expansion in the moving lattice and used to engineer the dispersion of the matter wavepacket (*lensing effect*). In the high density regime, when the nonlinearity of the wave equation becomes important, the Bloch states may be unstable against the growth of excitations which drive the system away from the initial state. The two main mechanisms of instability, *energetic* and *dynamic instability* (the latter already observed for the large amplitude dipole oscillations), have been deeply investigated, clearly separating the two regimes by identifying their different effects and timescales. However, the detailed comprehension of the mechanisms being activated after the onset of the instabilities is still incomplete. In particular, in the case of energetic instability, a more systematic study of the evolution of the system for different temperatures of the sample could provide further insight into the interactions between the condensate and the quantum-depleted fraction.

In the last chapter we have presented a simple technique for the generation of optical lattices with adjustable spatial period. We have studied the interference pattern generated after expansion by condensates initially located in the wells of an optical lattice with 10 μm spacing, finding results in agreement with the ones first observed in [35]. Furthermore, we have checked the effective localization of the system by exciting dipole oscillations and studying the following dynamics. The appeal of this system is that, by increasing the lattice spacing, it becomes possible to optically resolve the single lattice sites. This possibility could be important for the implementation of quantum computing schemes, where addressability is a fundamental requirement. As an extension of this work, the next step has to be made in the direction of manipulating the single sites either optically or with the application of radiofrequency/microwave transitions between different internal levels [138].

Until now we have considered only one-dimensional optical lattices. Recent experiments have taken advantage of deep bi-dimensional optical lattices in order to create arrays of tightly confining traps in which it is possible to study effects of reduced dimensionality. In this situation one can study a collection of truly one-dimensional systems and tune the effective interactions between atoms by changing the transverse confinement. In the weakly interacting limit one can study the superfluid properties of the system in a pure 1D configuration, in which all the radial degrees of freedom are frozen. One interesting possibility concerns the investigation of 1D condensates in optical lattices, mostly in connection with the study of instabilities. Increasing the transverse confinement, strong damping of dipole oscillations has been reported even for very shallow optical lattices [139] and explained as a possible consequence of

increased quantum fluctuations. In the strongly interacting limit, when the radial confinement is further increased and the total interaction energy overcomes the kinetic energy, the transition from a superfluid to a *Tonks gas* has been very recently observed [140, 141]. In this regime the bosons, instead of forming a Bose-Einstein condensate (as in the weakly interacting limit), tend to repel each other and occupy different positions in space, as if they were noninteracting fermions. The observation of this "fermionization" process, in which bosons act like fermions, is the counterpart of the experiments performed with quantum degenerate Fermi gases studying the possibility to achieve the BCS superconductive phase in which paired fermions behave as bosons [142, 143].

In the frame of studying different zero temperature regimes out of the superfluid condensed phase, one interesting perspective consists in the addition of a *random potential* on the regular optical lattice in order to achieve the transition to the *Bose-glass* phase. In this strongly interacting regime one should observe a nontrivial localization of the atoms in the disordered lattice wells, induced by the cooperation between interactions and disorder. This quantum phase, for several aspects resembling the Mott Insulator state, since no long-range coherence and zero on-site number fluctuations are expected to characterize it, has been theoretically predicted since many years [124] but not yet observed. Another fascinating possibility provided by the use of disordered potentials could be the observation of *Anderson localization* for matter waves, a pure quantum interference effect (well known in solid state physics) that forces a localization of the system for low disorder heights, when classically the propagation of the wave in the disordered medium would be allowed.

Working in this direction, in the last chapter we have presented the first experimental investigation of a Bose-Einstein condensate in a random potential created with an optical speckle pattern. Far from being in the strongly interacting regime of the Bose-glass phase, we have investigated the expansion of the atomic system from the random potential and studied how the collective dynamics is affected by the presence of disorder, interpreting the results in the frame of the mean-field Gross-Pitaevskii theory.

Still in the superfluid regime, the addition of a random potential on the regular optical lattice could be used also to study the effects of disorder on the quantum transport in periodic potentials. In this context, it would be interesting to use the random potential to simulate the presence of defects and inhomogeneities in the ordered crystalline structure. The modification of the conduction properties as a function of the disorder parameters could provide useful information for problems of solid state physics.

All these perspectives enforce the important role of Bose-Einstein condensates and optical lattices for the investigation of fundamental physics problems. The beauty of this field of research is indeed represented by its strong connections with other areas of physics, from nonlinear optics to quantum

computation, from solid state physics to the physics of strongly correlated systems. Many problems have already been addressed in the last few years and many others are still open. The plenty of interesting phenomena that still deserve investigation makes Bose-Einstein condensates in optical lattices a fertile ground for many other years of exciting research.

Acknowledgements

E adesso torniamo a scrivere in italiano...

Il primo e più sentito ringraziamento va al Prof. Massimo Inguscio, che mi ha offerto la possibilità di entrare a far parte del suo gruppo. A lui devo soprattutto la passione per la ricerca e l'entusiasmo che in tutti questi anni è riuscito a trasmettermi. Desidero soprattutto ringraziarlo per la fiducia che ha sempre riposto in me e che spero in minima parte di meritare.

Un posto d'onore nei ringraziamenti va sicuramente a Chiara Fort, che per me non è stata soltanto una guida, ma un punto di riferimento importante, sia dal punto di vista professionale che da quello umano. Non è facile trovare persone brave e al tempo stesso disponibili, con le quali riesci a trovarti in sintonia sin dal primo momento: Chiara è una di queste.

Vorrei poi ringraziare le persone con cui nel corso di questi anni ho avuto il piacere di collaborare, condividendo gioie e dolori del lavoro sperimentale. Un grazie a Pasquale Maddaloni e a Francesca Ferlaino per la loro simpatia e per avere portato un po' di Napoli a Firenze. Un grazie a Robert Saers, l'uomo venuto dal freddo, che mi ha introdotto alla bellezza della lingua svedese... prima o poi verrò a trovarti! Un grazie a Jessica Lye, dalla lontanissima Australia, che per rileggere questa tesi e mandarmi le correzioni ha quasi perso una nave per la Tasmania... Un grazie infine a Vera Guarrera, l'ultima arrivata nel gruppo: sono sicuro che qui a Firenze ti troverai benissimo!

Un grazie poi al Prof. Francesco Cataliotti, che mi ha seguito durante il primo anno di dottorato, e a Michele Modugno, un punto di riferimento sempre presente per mille dubbi e domande.

In questo elenco li ho lasciati per ultimi, ma meritano un ringraziamento particolare: sono i due laureandi con cui ho avuto il piacere di lavorare durante questi anni di tesi. Grazie a Jacopo e a Luigi. Insieme a voi le lunghe giornate in laboratorio sono passate molto più facilmente, anche nei momenti di difficoltà. Oltre che degli ottimi colleghi di lavoro, siete stati e continuerete ad essere per me dei cari amici.

Grazie anche a tutti gli altri "abitanti" del LENS e del Dipartimento di Fisica, in particolare a Saverio, a Giacomo (L. e R.), a Laura, a Nicola e a Paolo. Spero di non essermi dimenticato di nessuno!

Ma dietro questa tesi non ci sono soltanto amici e colleghi di lavoro. Ci sono

anche tante altre persone che in forme diverse mi hanno supportato durante questi anni e che hanno avuto la pazienza di sopportarmi durante la scrittura di questa tesi. Non le elencherò tutte perché sarebbe troppo lungo, ma alcuni ringraziamenti particolari sono d'obbligo.

Un grazie a Stefano, un punto di riferimento importante, per le lunghe chiacchierate e per avermi sempre incoraggiato nei momenti di incertezza.

Un grazie enorme a mia mamma, per tutto quello che ha fatto e che continua a fare.

Ti ho lasciata per ultima, ma sei la persona che più mi è stata vicina, vivendo insieme a me i momenti più felici e più duri di questo dottorato, sopportando le mie assenze e condividendo le mie gioie: il mio ultimo grazie, Manuela, è per te.

L.

List of Figures

Bibliography

[1] *Bose-Einstein condensation in atomic gases*, Proceedings of the International School of Physics "Enrico Fermi", course CXL, edited by M. Inguscio, S. Stringari, and C. E. Wieman, IOS Press, Amsterdam (1999).

[2] M. R. Andrews, C. G. Townsend, H.-J. Miesner, D. S. Durfee, D. M. Kurn, and W. Ketterle, Science **275**, 637 (1997).

[3] M. Kozuma, L. Deng, E. W. Hagley, J. Wen, R. Lutwak, K. Helmerson, S. L. Rolston, and W. D. Phillips, Phys. Rev. Lett. **82**, 871 (1999).

[4] Yu. B. Ovchinnikov, J. H. Müller, M. R. Doery, E. J. D. Vredenbregt, K. Helmerson, S. L. Rolston, and W. D. Phillips, Phys. Rev. Lett. **83**, 284 (1999).

[5] M. Raizen, C. Salomon, and Q. Niu, Phys. Today **50**, 30 (1997) and references therein.

[6] S. Burger, K. Bongs, S. Dettmer, W. Ertmer, K. Sengstock, A. Sanpera, G. V. Shlyapnikov, and M. Lewenstein, Phys. Rev. Lett. **83**, 5198 (1999).

[7] L. Deng, E. W. Hagley, J. Wen, M. Trippenbach, Y. B. Band, P. S. Julienne, J. E. Simsarian, K. Helmerson, S. L. Rolston, and W. D. Phillips, Nature **398**, 218 (1999).

[8] B. Wu and Q. Niu, Phys. Rev. A **64**, 061603R (2001).

[9] G. Roati, E. de Mirandes, F. Ferlaino, H. Ott, G. Modugno, and M. Inguscio, Phys. Rev. Lett. **92**, 230402 (2004).

[10] F. London, Phys. Rev. **54**, 947 (1938).

[11] M. R. Matthews, B. P. Anderson, P. C. Haljan, D. S. Hall, C. E. Wieman, and E. A. Cornell, Phys. Rev. Lett. **83**, 2498 (1999).

[12] F. Chevy, K. W. Madison, and J. Dalibard, Phys. Rev. Lett. **85**, 2223 (2000).

[13] O. M. Maragò, S. A. Hopkins, J. Arlt, E. Hodby, G. Hechenblaikner, and C. J. Foot, Phys. Rev. Lett. **84**, 2056 (2000).

[14] D. Guéry-Odelin and S. Stringari, Phys. Rev. Lett. **83**, 4452 (2003).

[15] D. S. Jin, J. R. Ensher, M. R. Matthews, C. E. Wieman, and E. A. Cornell, Phys. Rev. Lett. **77**, 420 (1996).

[16] M.-O. Mewes, M. R. Andrews, N. J. van Druten, D. M. Kurn, D. S. Durfee, C. G. Townsend, and W. Ketterle, Phys. Rev. Lett. **77**, 988 (1996).

[17] B. P. Anderson and M. A. Kasevich, Science **282**, 1686 (1998).

[18] M. Greiner, I. Bloch, O. Mandel, T. W. Hänsch, and T. Esslinger, Phys. Rev. Lett. **87**, 160405 (2001).

[19] P. Pedri, L. Pitaevskii, S. Stringari, C. Fort, S. Burger, F. S. Cataliotti, P. Maddaloni, F. Minardi, and M. Inguscio, Phys. Rev. Lett. **87**, 220401 (2001).

[20] F. S. Cataliotti, S. Burger, C. Fort, P. Maddaloni, F. Minardi, A. Trombettoni, A. Smerzi, and M. Inguscio, Science **293**, 843 (2001).

[21] M. Greiner, O. Mandel, T. Esslinger, T. W. Hänsch, and I. Bloch, Nature **415**, 39 (2002).

[22] R. Roth and K. Burnett, Phys. Rev. A **68**, 023604 (2003).

[23] B. Damski, J. Zakrzewski, L. Santos, P. Zoller, and M. Lewenstein, Phys. Rev. Lett. **91**, 080403 (2003).

[24] G. K. Brennen, C. M. Caves, P. S. Jessen, and I. H. Deutsch, Phys. Rev. Lett. **82**, 1060 (1999).

[25] D. Jaksch, H.-J. Briegel, J. I. Cirac, C. W. Gardiner, and P. Zoller, Phys. Rev. Lett. **82**, 1975 (1999).

[26] F. Schmidt-Kaler, H. Häffner, M. Riebe, S. Gulde, G. P. T. Lancaster, T. Deuschle, C. Becher, C. F. Roos, J. Eschner, and R. Blatt, Nature **422**, 408 (2003).

[27] D. Leibfried, B. DeMarco, V. Meyer, D. Lucas, M. Barrett, J. Britton, W. M. Itano, B. Jelenković, C. Langer, T. Rosenband, and D. J. Wineland, Nature **422**, 412 (2003).

[28] O. Mandel, M. Greiner, A. Widera, T. Rom, T. W. Hänsch, and I. Bloch, Nature **425**, 937 (2003).

[29] C. Fort, F. S. Cataliotti, L. Fallani, F. Ferlaino, P. Maddaloni, and M. Inguscio, Phys. Rev. Lett. **90**, 140405 (2003).

[30] F. S. Cataliotti, L. Fallani, F. Ferlaino, C. Fort, P. Maddaloni, and M. Inguscio, New Journ. Phys. **5**, 71 (2003).

[31] L. Fallani, F. S. Cataliotti, J. Catani, C. Fort, M. Modugno, M. Zawada, and M. Inguscio, Phys. Rev. Lett. **91**, 240405 (2003).

[32] L. Fallani, L. De Sarlo, J. E. Lye, M. Modugno, R. Saers, C. Fort, and M. Inguscio, Phys. Rev. Lett. **93**, 140406 (2004).

[33] L. De Sarlo, L. Fallani, J. E. Lye, M. Modugno, R. Saers, C. Fort, and M. Inguscio, `cond-mat/0412279` (2004).

[34] J. E. Lye, L. Fallani, M. Modugno, D. Wiersma, C. Fort, and M. Inguscio, `cond-mat/0412167` (2004).

[35] Z. Hadzibabic, S. Stock, B. Battelier, V. Bretin, and J. Dalibard, Phys. Rev. Lett. **93**, 180403 (2004).

[36] A. Einstein, Sitzber. Kgl. Preuss. Akad. Wiss., 261 (1924); *ibidem*, 3 (1925).

[37] S. N. Bose, Z. Phys. **26**, 178 (1924).

[38] L. Pitaevskii and S. Stringari, *Bose-Einstein condensation*, Oxford University Press (2004).

[39] E. A. Cornell and C. E. Wieman, *Nobel Lecture*, Rev. Mod. Phys. **74**, 875 (2002).

[40] W. Ketterle, *Nobel Lecture*, Rev. Mod. Phys. **74**, 1131 (2002).

[41] F. Dalfovo, S. Giorgini, L. Pitaevskii, and S. Stringari, Rev. Mod. Phys. **71**, 463 (1999).

[42] K. Huang, *Statistical Mechanics*, John Wiley & Sons (1987).

[43] L. D. Landau and E. M. Lifshitz, *Statistical Physics*, Pergamon Press, Oxford (1969).

[44] N. W. Ashcroft and N. D. Mermin, *Solid State Physics*, Saunders College Publishing (1976).

[45] J. C. Slater, Phys. Rev. **87**, 807 (1976).

[46] C. Zener, Proc. R. Soc. London A **145**, 523 (1934).

[47] J. H. Denschlag, J. E. Simsarian, H. Häffner, C. McKenzie, A. Browaeys, D. Cho, K. Helmerson, S. L. Rolston, and W. D. Phillips, J. Phys. B **35**, 3095 (2002).

[48] O. Morsch, J. H. Müller, M. Cristiani, D. Ciampini, and E. Arimondo, Phys. Rev. Lett. **87**, 140402 (2001).

[49] B. Wu and Q. Niu, New Journ. Phys. **5**, 104 (2003).

[50] M. Machholm, C. J. Pethick, and H. Smith, Phys. Rev. A **67**, 053613 (2003).

[51] B. T. Seaman, L. D. Carr, and M. J. Holland, `cond-mat/0410347` (2004).

[52] M. Machholm, A. Nicolin, C. J. Pethick, and H. Smith, Phys. Rev. A **69**, 043604 (2004).

[53] P. J. Y. Louis, E. A. Ostrovskaya, C. M. Savage, and Y. S. Kivshar, Phys. Rev. A **67**, 013602 (2003).

[54] A. Trombettoni and A. Smerzi, Phys. Rev. Lett. **86**, 2353 (2001).

[55] M. P. A. Fisher, P. B. Weichman, G. Grinstein, and D. S. Fisher, Phys. Rev. B **40**, 546 (1989).

[56] D. Jaksch, C. Bruder, J. I. Cirac, C. W. Gardiner, and P. Zoller, Phys. Rev. Lett. **81**, 3108 (1998).

[57] M. Greiner, O. Mandel, T. W. Hänsch, and I. Bloch, Nature **419**, 51 (2002).

[58] C. Fort, M. Prevedelli, F. Minardi, F. S. Cataliotti, L. Ricci, G. M. Tino, and M. Inguscio, Europhys. Lett. **49**, 8 (2000).

[59] M. Fattori, *Esperimenti di interferometria spaziale e temporale con condensati atomici di Bose-Einstein*, Diploma thesis, University of Florence (2001).

[60] P. Maddaloni, *Experiments on macroscopic quantum coherence in Bose-Einstein condensates*, PhD thesis, University of Padova (2003).

[61] J. Catani, *Interazione tra un'onda di materia coerente e un reticolo ottico*, Diploma thesis, University of Florence (2003).

[62] L. De Sarlo, *Instabilità di un condensato di Bose-Einstein in un reticolo ottico*, Diploma thesis, University of Florence (2004).

[63] S. Chu, *Nobel Lecture*, Rev. Mod. Phys. **70**, 685 (1998).

[64] C. Cohen-Tannoudji, *Nobel Lecture*, Rev. Mod. Phys. **70**, 707 (1998).

[65] W. D. Phillips, *Nobel Lecture*, Rev. Mod. Phys. **70**, 721 (1998).

[66] T. W. Hänsch and A. L. Schawlow, Opt. Comm. **13**, 68 (1975).

[67] D. G. Fried, T. C. Killian, L. Willmann, D. Landhuis, S. C. Moss, D. Kleppner, and T. J. Greytak, Phys. Rev. Lett. **81**, 3811 (1998).

[68] E. L. Raab, M. Prentiss, A. Cable, S. Chu, and D. E. Pritchard, Phys. Rev. Lett. **59**, 2631 (1987).

[69] C. Monroe, W. Swann, H. Robinson, and C. Wieman, Phys. Rev. Lett. **65**, 1571 (1990).

[70] D. A. Steck, *Rubidium 87 D Line Data*, available at `http://george.ph.utexas.edu/~dsteck/alkalidata` (2001).

[71] L. Ricci, M. Weidemüller, T. Esslinger, A. Hemmerich, C. Zimmermann, V. Vuletic, W. König, and T. W. Hänsch, Opt. Comm. **117**, 641 (1995).

[72] A. L. Migdall, J. V. Prodan, W. D. Phillips, T. H. Bergeman, and H. J. Metcalf, Phys. Rev. Lett. **54**, 2596 (1985).

[73] J. D. Jackson, *Classical Electrodynamics*, John Wiley & Sons (1962).

[74] W. H. Wing, Progr. in Quant. Elec. **8**, 181 (1994).

[75] J. Söding, D. Guéry-Odelin, P. Desbiolles, G. Ferrari, and J. Dalibard, Phys. Rev. Lett. **80**, 1869 (1998).

[76] T. Esslinger, I. Bloch, and T. W. Hänsch, Phys. Rev. A **58**, R2664 (1998).

[77] D. E. Pritchard, Phys. Rev. Lett. **51**, 1336 (1983).

[78] E. Majorana, Il Nuovo Cimento **9**, 43 (1932).

[79] W. Ketterle, D. S. Durfee, and D. M. Stamper-Kurn, *Making, probing and understanding Bose-Einstein condensates*, in *Bose-Einstein condensation in atomic gases*, Proceedings of the International School of Physics "Enrico Fermi", course CXL, edited by M. Inguscio, S. Stringari and C. E. Wieman, IOS Press, Amsterdam (1999).

[80] F. James, *MINUIT Reference manual*, CERNLIB documentation available at `http://wwwasdoc.web.cern.ch/wwwasdoc/minuit/` (1998).

[81] W. H. Press, S. A. Teukolsky, W. T. Vetterling, and B. P. Flannery, *Numerical Recipes in C*, Cambridge University Press (1992).

[82] S. Stringari, Phys. Rev. Lett. **77**, 2360 (1996).

[83] A. Smerzi, A. Trombettoni, P. G. Kevrekidis, and A. R. Bishop, Phys. Rev. Lett. **89**, 170402 (2002).

[84] F. Nesi and M. Modugno, J. Phys. B **37**, S101 (2004).

[85] C. Cohen-Tannoudji, *Atomic motion in laser light*, in *Fundamental systems in Quantum optics*, Les Houches, Session LIII (July 1990), edited by J. Dalibard, J. M. Raimond and J. Zinn-Justin, Elsevier (1992).

[86] R. Grimm, M. Weidemüller, and Y. B. Ovchinnikov, Adv. At. Mol. Opt. Phys. **42**, 95 (2000).

[87] H. J. Metcalf and P. van der Straten, *Laser cooling and trapping*, Springer Verlag (1999).

[88] J. Stenger, S. Inouye, A. P. Chikkatur, D. M. Stamper-Kurn, D. E. Pritchard, and W. Ketterle, Phys. Rev. Lett. **82**, 4569 (1999); see also the erratum J. Stenger *et al.*, Phys. Rev. Lett. **84**, 2283 (2000).

[89] F. Zambelli, L. Pitaevskii, D. M. Stamper-Kurn, and S. Stringari, Phys. Rev. A **61**, 063608 (2000).

[90] A. P. Chikkatur, A. Görlitz, D. M. Stamper-Kurn, S. Inouye, S. Gupta, and W. Ketterle, Phys. Rev. Lett. **85**, 483 (2000).

[91] M. Krämer, L. Pitaevskii, and S. Stringari, Phys. Rev. Lett. **88**, 180404 (2002).

[92] M. Krämer, *Bose-Einstein Condensates in Rotating Traps and Optical Lattices*, PhD Thesis, University of Trento (2004).

[93] F. Chevy, V. Bretin, P. Rosenbusch, K. W. Madison, and J. Dalibard, Phys. Rev. Lett. **88**, 250402 (2002).

[94] C. Menotti, A. Smerzi, and A. Trombettoni, New Journ. Phys. **5**, 112 (2003).

[95] F. Kh. Abdullaev, B. B. Baizakov, S. A. Darmanyan, V. V. Konotop, and M. Salerno, Phys. Rev. A **64**, 043606 (2001).

[96] V. V. Konotop and M. Salerno, Phys. Rev. A **65**, 021602R (2002).

[97] M. Modugno, C. Tozzo, and F. Dalfovo, Phys. Rev. A **70**, 043625 (2004); see also the erratum M. Modugno *et al.*, Phys. Rev. A **71**, 019904 (2005).

[98] L. Salasnich, Laser Physics **12**, 198 (2002).

[99] L. Salasnich, A. Parola, and L. Reatto, Phys. Rev. A **65**, 043614 (2002).

[100] L. I. Schiff, *Quantum Mechanics*, McGraw-Hill (1949).

[101] O. Morsch, M. Cristiani, J. H. Müller, D. Ciampini, and E. Arimondo, Phys. Rev. A **66**, 021601R (2002).

[102] P. Massignan and M. Modugno, Phys. Rev. A **67**, 023614 (2003).

[103] Y. Castin and R. Dum, Phys. Rev. Lett. **77**, 5315 (1996).

[104] Y. Kagan, E. L. Surkov, and G. V. Shlyapnikov, Phys. Rev. A **54**, R1753 (1996); Phys. Rev. A **55**, R18 (1997).

[105] D. E. Pritchard, A. D. Cronin, S. Gupta, and D. A. Kokorowski, Ann. Phys. **10**, 35 (2001)

[106] S. L. Rolston and W. D. Phillips, Nature **416**, 219 (2002).

[107] S. Inouye, T. Pfau, S. Gupta, A. P. Chikkatur, A. Gorlitz, D. E. Pritchard, and W. Ketterle, Nature **402**, 641 (1999)

[108] M. Kozuma, Y. Suzuki, Y. Torii, T. Sugiura, T. Kuga, E. W. Hagley, and L. Deng, Science **286**, 2309 (1999).

[109] B. Eiermann, P. Treutlein, Th. Anker, M. Albiez, M. Taglieber, K. P. Marzlin, and M. K. Oberthaler, Phys. Rev. Lett. **91**, 060402 (2003).

[110] B. Eiermann, Th. Anker, M. Albiez, M. Taglieber, P. Treutlein, K. P. Marzlin, and M. K. Oberthaler, Phys. Rev. Lett. **92**, 230401 (2004).

[111] L. Khaykovich, F. Schreck, G. Ferrari, T. Bourdel, J. Cubizolles, L. D. Carr, Y. Castin, and C. Salomon, Science **296**, 1290 (2002).

[112] K. E. Strecker, G. B. Partridge, A. G. Truscott, and R. G. Hulet, Nature **417**, 150 (2002).

[113] S. Burger, F. S. Cataliotti, C. Fort, F. Minardi, M. Inguscio, M. L. Chiofalo, M. P. Tosi, Phys. Rev. Lett. **86**, 4447 (2001); see also the comment B. Wu and Q. Niu, Phys. Rev. Lett. **89**, 088901 (2002), and the reply S. Burger *et al.*, Phys. Rev. Lett. **89**, 088902 (2002).

[114] M. Cristiani, O. Morsch, N. Malossi, M. Jona-Lasinio, M. Anderlini, E. Courtade, and E. Arimondo, Optics Express **12**, 4 (2004).

[115] R.G. Scott, A.M. Martin, T.M. Fromhold, S. Bujkiewicz, F.W. Sheard, and M. Leadbeater, Phys. Rev. Lett. **90**, 110404 (2003).

[116] Y. Zheng, M. Koštrun, and J. Javanainen, Phys. Rev. Lett. **93**, 230401 (2004).

[117] M. Krämer, C. Menotti, and M. Modugno, `cond-mat/0407014` (2004).

[118] W. Zwerger, J. Opt. B **5**, S9 (2003).

[119] D. Boiron, C. Mennerat-Robilliard, J.-M. Fournier, L. Guidoni, C. Salomon, and G. Grynberg, Eur. Phys. J. D **7**, 373 (1999).

[120] J. D. Reppy, J. Low Temp. Phys. **87**, 205 (1992) and references therein.

[121] G. E. Astrakharchik, J. Boronat, J. Casulleras, and S. Giorgini, Phys. Rev. A **66**, 023603 (2002).

[122] S. Giorgini, L. Pitaevskii, and S. Stringari, Phys. Rev. B **49**, 12938 (1994).

[123] K. Huang and H. F. Meng, Phys. Rev. Lett. **69**, 644 (1992).

[124] M. P. A. Fisher, P. B. Weichman, G. Grinstein, and D. S. Fisher, Phys. Rev. B **40**, 546 (1989).

[125] R. T. Scalettar, G. G. Batrouni, and G. T. Zimanyi, Phys. Rev. Lett. **66**, 3144 (1991).

[126] W. Krauth, N. Trivedi, and D. Ceperley, Phys. Rev. Lett. **67**, 2307 (1991).

[127] P. W. Anderson, Phys. Rev. **109**, 1492 (1958).

[128] P. A. Lee and T. V. Ramakrishnan, Rev. Mod. Phys. **57**, 287 (1985).

[129] D. S. Wiersma, P. Bartolini, A. Lagendijk, and R. Righini, Nature **390**, 671 (1997).

[130] J. Fortágh, H. Ott, S. Kraft, A. Günther, and C. Zimmermann, Phys. Rev. A **66**, 041604(R) (2002).

[131] A. E. Leanhardt, A. P. Chikkatur, D. Kielpinski, Y. Shin, T. L. Gustavson, W. Ketterle, and D. E. Pritchard, Phys. Rev. Lett. **89**, 040401 (2002).

[132] J. Estève, C. Aussibal, C. Figl, D. Mailly, I. Bouchoule, C. I. Westbrook, and A. Aspect, Phys. Rev. A **70**, 043629 (2004).

[133] M. P. A. Jones, C. J. Vale, D. Sahagun, B. V. Hall, and E. A. Hinds, Phys. Rev. Lett. **91**, 080401 (2003).

[134] D. W. Wang, M. D. Lukin, and E. Demler, Phys. Rev. Lett. **92**, 076802 (2004).

[135] S. Dettmer, D. Hellweg, P. Ryytty, J. J. Arlt, W. Ertmer, K. Sengstock, D. S. Petrov, G. V. Shlyapnikov, H. Kreutzmann, L. Santos, and M. Lewenstein, Phys. Rev. Lett. **87**, 160406 (2001).

[136] S. Richard, F. Gerbier, J. H. Thywissen, M. Hugbart, P. Bouyer, and A. Aspect, Phys. Rev. Lett. **91**, 010405 (2003).

[137] M. Modugno, private communication (2004).

[138] D. Schrader, I. Dotsenko, M. Khudaverdyan, Y. Miroshnychenko, A. Rauschenbeutel, and D. Meschede, Phys. Rev. Lett. **93**, 150501 (2004).

[139] C. D. Fertig, K. M. O'Hara, J. H. Huckans, S. L. Rolston, W. D. Phillips, and J. V. Porto, `cond-mat/0410491` (2004).

[140] B. Paredes, A. Widera, V. Murg, O. Mandel, S. Fölling, I. Cirac, G. V. Shlyapnikov, T. W. Hänsch, and I. Bloch, Nature **429**, 277 (2004).

[141] T. Kinoshita, T. Wenger, and D. S. Weiss, Science **305**, 1125 (2004).

[142] C. A. Regal, M. Greiner, and D. S. Jin, Phys. Rev. Lett. **92**, 040403 (2004).

[143] C. Chin, M. Bartenstein, A. Altmeyer, S. Riedl, S. Jochim, J. Hecker Denschlag, and R. Grimm, Science **305**, 1128 (2004).